



**Max-Planck-Institut für Metallforschung  
Stuttgart**

---

**Nitriding of Fe–Cr–Al alloys:  
nitride precipitation and phase transformations**

Arno Rainer Clauß

Dissertation  
an der  
**Universität Stuttgart**

---

Bericht Nr. 221  
Dezember 2008



# **Nitriding of Fe–Cr–Al alloys: nitride precipitation and phase transformations**

Von der Fakultät Chemie der Universität Stuttgart  
zur Erlangung der Würde eines Doktors der Naturwissenschaften (Dr. rer. nat.)  
genehmigte Abhandlung

vorgelegt von

Arno Rainer Clauß

aus Lauffen am Neckar

Hauptberichter: Prof. Dr. Ir. E. J. Mittemeijer

Mitberichter: Prof. Dr. F. Aldinger

Mitprüfer: Prof. Dr. E. Roduner

Tag der Einreichung: 07.10.2008

Tag der mündlichen Prüfung: 02.12.2008

MAX-PLANCK-INSTITUT FÜR METALLFORSCHUNG, STUTTGART  
INSTITUT FÜR METALLKUNDE DER UNIVERSITÄT STUTTGART

Stuttgart 2008



# Contents

<b>1 Introduction</b> .....	<b>9</b>
<b>1.1 Nitriding</b> .....	<b>9</b>
1.1.1 Gaseous nitriding.....	11
1.1.2 Thermodynamic of gaseous nitriding .....	13
1.1.3 The Fe–N phase diagram .....	16
1.1.4 Nitriding potential and Lehrer diagram.....	17
1.1.5 Morphology of the nitrided zone .....	18
1.1.6 Constitution of the nitrided zone .....	19
1.1.7 Excess nitrogen .....	20
1.1.8 Residual stresses .....	21
<b>1.2 Aim and outlook of the thesis</b> .....	<b>24</b>
<b>2 Crystal structure and morphology of mixed <math>\text{Cr}_{1-x}\text{Al}_x\text{N}</math> nitride precipitates; gaseous nitriding of a Fe–1.5wt.%Cr–1.5wt.%Al alloy</b> .....	<b>31</b>
<b>2.1 Introduction</b> .....	<b>31</b>
2.1.1 Nitrides in binary ferritic alloys .....	32
2.1.2 Nitrides in ternary ferritic alloys.....	33
<b>2.2 Experimental</b> .....	<b>34</b>
2.2.1 Specimen preparation.....	34
2.2.2 Nitriding .....	35
2.2.3 Specimen characterisation .....	35
2.2.3.1 X-ray diffractometry .....	35
2.2.3.2 Electron probe microanalysis (EPMA) .....	36
2.2.3.3 Light microscopy (LM).....	36
2.2.3.4 Microhardness measurement .....	36
2.2.3.5 Transmission electron microscopy (TEM, STEM and HRTEM) .....	37
2.2.4 Determination of nitrogen absorption isotherm .....	39
<b>2.3 Results and evaluation</b> .....	<b>40</b>
2.3.1 Phase analysis .....	40

2.3.2 Crack formation .....	40
2.3.3 Composition and microhardness depth profiles .....	41
2.3.4 Transmission electron microscopy analysis (TEM) .....	43
2.3.4.1 Crystallography of nitride precipitates and deformation structure.....	43
2.3.4.2 High resolution transmission electron microscopy (HRTEM) .....	47
2.3.4.3 Composition of the nitride precipitates .....	49
2.3.4.4 Jet-electropolished TEM samples .....	50
2.3.5 Analysis of excess nitrogen uptake .....	51
<b>2.4 General discussion .....</b>	<b>55</b>
2.4.1 Combined precipitation of Al and Cr in mixed nitride precipitates .....	55
2.4.2 Precipitate morphology and coherency effects .....	56
2.4.3 Depth gradient of precipitate size.....	57
2.4.4 The orientation relationship .....	57
2.4.5 Excess nitrogen.....	58
2.4.6 Crack formation along grain boundaries .....	58
<b>2.5 Conclusions .....</b>	<b>59</b>
<b>3 Phase transformation of mixed <math>\text{Cr}_{1-x}\text{Al}_x\text{N}</math> nitride precipitates in ferrite .....</b>	<b>65</b>
<b>3.1 Introduction; instability of nitrides.....</b>	<b>65</b>
<b>3.2 Experimental .....</b>	<b>67</b>
3.2.1 Specimen preparation .....	67
3.2.2 Nitriding and subsequent annealing .....	67
3.2.3 Microstructural analysis.....	68
<b>3.3 Results and discussion.....</b>	<b>70</b>
3.3.1 Concentration depth and microhardness depth profiles; after nitriding and after subsequent annealing.....	70
3.3.2 Precipitates after nitriding and after subsequent annealing; structure, composition and orientation relationships .....	73
3.3.2.1 Near the surface.....	73
3.3.2.2 In the nitrogen diffusion zone .....	77
3.3.2.3 In the initially unnitrided core.....	79

---

<b>3.4 Conclusions.....</b>	<b>84</b>
<b>4 The microstructure of the diffusion zone of a gaseously nitrided Fe–1.5wt.%Cr–1.5wt.%Al alloy .....</b>	<b>89</b>
<b>4.1 Introduction .....</b>	<b>89</b>
<b>4.2 Experimental.....</b>	<b>91</b>
4.2.1 Specimen preparation.....	91
4.2.2 Nitriding .....	92
4.2.3 Specimen characterisation .....	92
4.2.3.1 X-ray diffractometry .....	92
4.2.3.2 Electron probe microanalysis (EPMA) .....	93
4.2.3.3 Light microscopy (LM).....	93
4.2.3.4 Microhardness measurement (Vickers hardness).....	93
4.2.4 Determination of the residual stress depth profile by X-ray diffractometry	94
4.2.5 Scanning transmission electron microscopy (STEM).....	95
4.2.6 Auger electron spectroscopy (AES).....	95
<b>4.3 Phase analysis and ferrite-matrix lattice strains .....</b>	<b>96</b>
<b>4.4 Development of nitrogen concentration- and microhardness-depth profiles .....</b>	<b>96</b>
<b>4.5 Residual stress-depth profile .....</b>	<b>100</b>
<b>4.6 Crack formation.....</b>	<b>103</b>
<b>4.7 Ferrite-matrix lattice strains.....</b>	<b>105</b>
<b>4.8 Nitrogen and aluminium segregation at grain boundaries .....</b>	<b>107</b>
<b>4.9 Conclusions.....</b>	<b>115</b>
<b>5 Summary .....</b>	<b>119</b>
<b>5.1 Introduction .....</b>	<b>119</b>
<b>5.2 Experimental.....</b>	<b>120</b>
5.2.1 Specimen preparation.....	120
5.2.2 Nitriding .....	120

5.2.3 Specimen characterisation .....	121
<b>5.3 Results .....</b>	<b>122</b>
5.3.1 Crystal structure and morphology of mixed $\text{Cr}_{1-x}\text{Al}_x\text{N}$ nitride precipitates	122
5.3.2 Phase transformation of mixed $\text{Cr}_{1-x}\text{Al}_x\text{N}$ nitride precipitates in ferrite....	123
5.3.3 The microstructure of the diffusion zone of a gaseously nitrided Fe–1.5wt.%Cr–1.5wt.%Al alloy .....	124
<b>6 Zusammenfassung in deutscher Sprache .....</b>	<b>127</b>
<b>6.1 Einleitung.....</b>	<b>127</b>
<b>6.2 Experimentelles .....</b>	<b>128</b>
6.2.1 Probenpräparation .....	128
6.2.2 Nitrieren .....	129
6.2.3 Charakterisierung der Proben .....	129
<b>6.3 Ergebnisse.....</b>	<b>131</b>
6.3.1 Kristallstruktur und Morphologie gemischter $\text{Cr}_{1-x}\text{Al}_x\text{N}$ Nitridausscheidungen.....	131
6.3.2 Phasenumwandlung von inneren $\text{Cr}_{1-x}\text{Al}_x\text{N}$ Mischnitridausscheidungen in Ferrit.....	132
6.3.3 Die Mikrostruktur in der Diffusionszone einer gasnitrierten Fe–1,5Gew.%Cr–1,5Gew.%Al-Legierung.....	133
<b>Danksagung .....</b>	<b>135</b>
<b>Curriculum Vitae .....</b>	<b>137</b>







# Chapter 1

## Introduction

### 1.1 Nitriding

To improve mechanical and/or corrosion properties of iron-based workpieces, nitriding is a widely applied thermochemical surface treatment method. The nitrided zone of a ferritic iron-based workpiece usually consists of the “compound layer” (often also called “white layer” since it appears white on light micrographs) and the “diffusion zone” (cf. Fig. 1.1).

workpiece surface

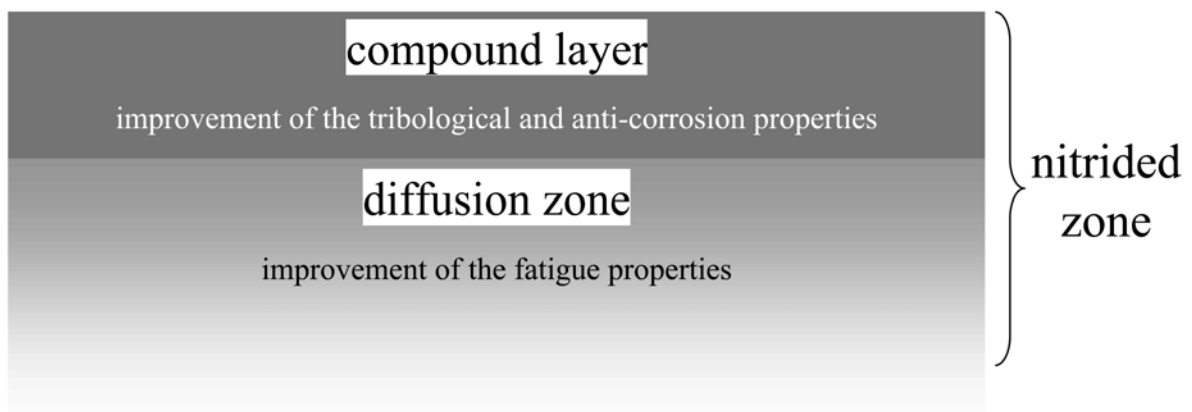


Fig. 1.1: Schematic illustration of the nitrided zone of an iron-based workpiece. The nitrided zone can be subdivided into “compound layer” and “diffusion zone”.

During nitriding no phase transition of the ferritic matrix occurs as compared with the austenite-martensite transition upon hardening. For this reason nitriding is appreciated widely in industry because a minimum of distortion occurs and an excellent control of the workpiece dimension is provided. Further, nitriding optimises the resistance to fatigue, wear and corrosion in the workpiece adjacent region (cf. Fig. 1.1). The mechanisms of nitriding are generally known (cf. section 1.1.5). However, specific reactions that occur in different iron-based alloys are not always known and the demanded properties have been developed empirically.

Typical nitriding steels are medium-carbon steels containing strong nitride-forming elements like aluminium, chromium, titanium, vanadium and molybdenum. The nitrides of these elements, which form in the ferrite matrix during the nitriding process, effect the demanded properties at the workpiece surface (cf. section 1.1.5).

With the beginning 20<sup>th</sup> century heat treating of steels was started to be investigated by means of fundamental, scientific research. Although scientific investigations improve the processing methods and the workpiece properties, a comprehensive experience is still essential [1].

Nitriding is a thermochemical diffusion method [2], which leads to the introduction of nitrogen into the workpiece surface of an iron-based, ferritic alloy accompanied by a modification of the chemical composition and microstructure in the surface adjacent region of the workpiece. Nitrogen donating media can generally be gases (gaseous nitriding), plasma (plasma nitriding), liquids (salt-bath nitrocarburising<sup>1</sup>) and powders (powder nitrocarburising<sup>1</sup>) [3]. All variants have different technical preferences. Two requirements are necessary for the introduction of nitrogen into the surface of a workpiece: (i) a concentration gradient, which can be adjusted by keeping the nitrogen concentration higher at the workpiece surface than beneath and (ii) an appropriate nitrogen diffusivity, which can usually be increased by increasing the temperature. The nitriding temperature range is typically between 500 °C and 590 °C (773 K to 863 K) [2, 3].

The various above mentioned nitriding methods indicate the current efforts for the improvement of material properties. The understanding and controlling of processes, which take place in iron-based alloys upon nitriding, can provide cost-effective applications and processing. The results of the present thesis promote such ambitions.

---

<sup>1</sup> Nitrogen is introduced together with carbon.

### 1.1.1 Gaseous nitriding

Gaseous nitriding allows, in comparison with other nitriding methods (see above), a more accurate control of the chemical potential and activity of nitrogen in the nitriding atmosphere and hence at the workpiece surface (see section 1.1.2). The nitriding atmosphere consists of an ammonia/hydrogen gas mixture with ammonia ( $\text{NH}_3$ ) as the nitrogen donating component. Ammonia dissociates catalytically at the workpiece surface and atomic nitrogen becomes dissolved in the ferrite matrix. The nitrogen activity at the workpiece surface can be kept constant by using a nitriding facility that allows a flow-through of the gas mixture (see section 1.1.2 and the kinetic of the ammonia decomposition in Ref. [4]).

The gaseous nitriding facility, which was used for the experimental work of the present thesis, is shown in Figs. 1.2 and 1.3.

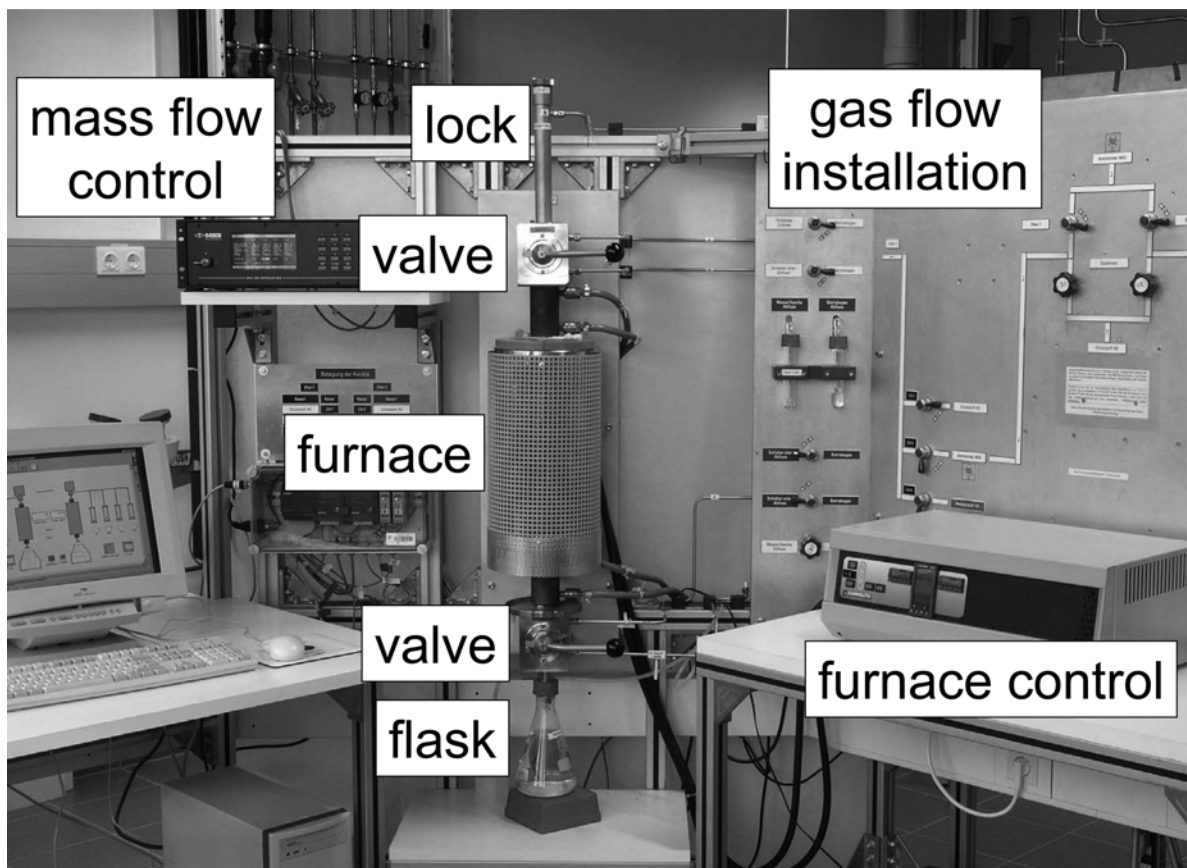


Fig. 1.2: Gaseous nitriding facility consisting of a vertical, multizone quartz-tube furnace with control, a lock for charging, valves and a gas-flow installation with mass-flow control. The flask, filled with water, is used for quenching the nitriding specimen after nitriding to stop the process.

It consists of a vertical, multizone quartz-tube furnace, which allows a precise temperature control within  $\pm 1$  K in each temperature zone (three in number). Mass-flow controllers adjust the nitriding gas mixture (i.e. ammonia and hydrogen mass flow).

The way of the gas flow is illustrated in Fig. 1.3 a. An enlarged view on the nitriding specimen (“workpiece”) is shown in Fig. 1.3 b. The nitriding specimen is suspended on a rod with a quartz fibre and centred in the furnace. The nitriding process is stopped by breaking mechanically the quartz fibre in the furnace so that the specimen can fall through an opened valve into a flask filled with water and flushed with nitrogen gas, where it is quenched.

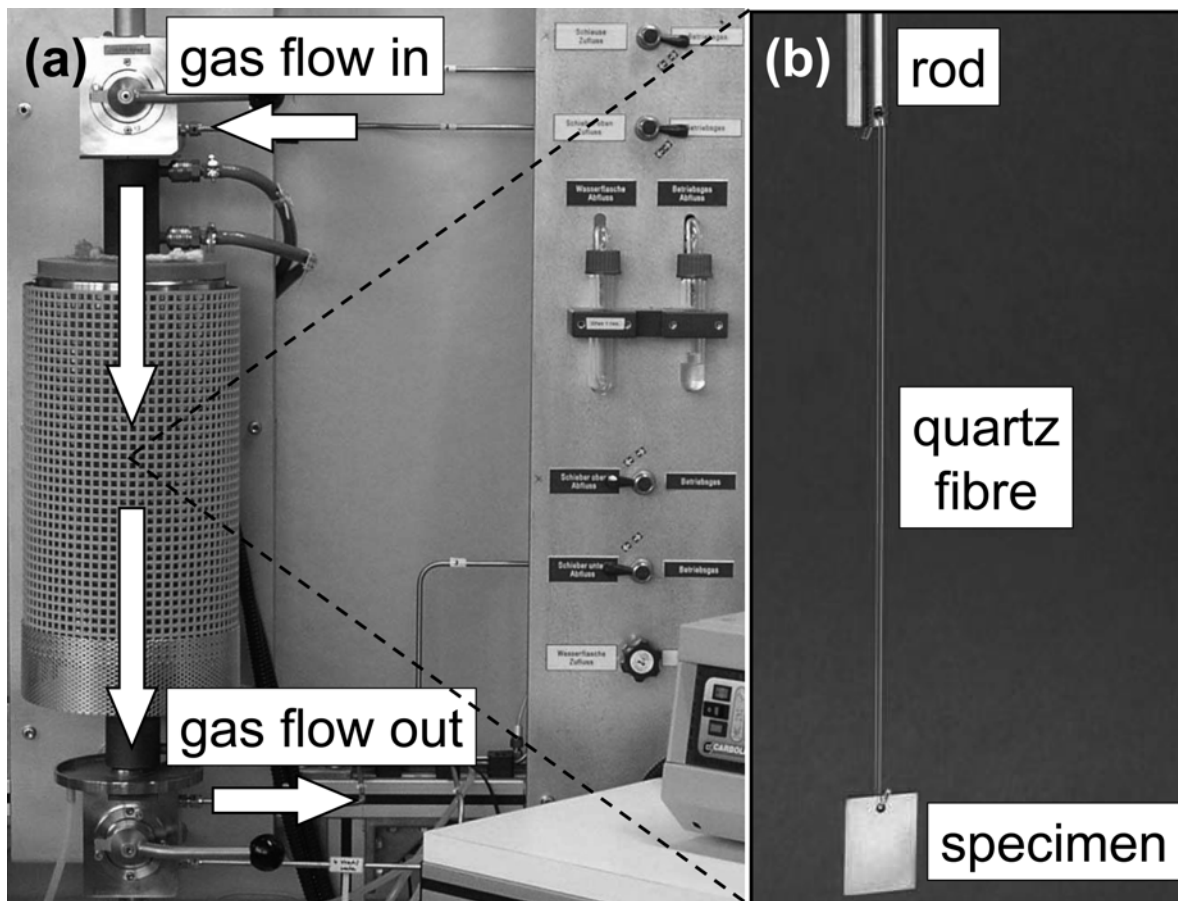
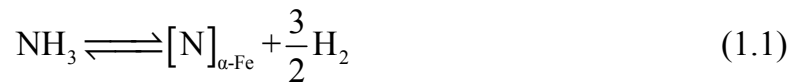


Fig. 1.3: (a) way of the nitriding gas mixture flow. (b) enlarged view on the nitriding specimen suspended on a rod by means of a quartz fibre.

### 1.1.2 Thermodynamic of gaseous nitriding

The relation between process parameters and morphology of the produced surface layer is of great interest for the realisation of well defined compositions and structures and, hence, properties. For this reason it is necessary to have a reproducible, controllable processing. Well controlled nitriding requires knowledge and control of the chemical potential and the corresponding nitrogen activity as provided by an ammonia/hydrogen gas mixture. N<sub>2</sub> gas as nitrogen donating medium is not suitable for gaseous nitriding because the nitrogen activity at atmospheric pressure is too low [5, 6].

Gaseous nitriding involves a metal-gas reaction between solid ferrite and an ammonia/hydrogen gas mixture. Thereby nitrogen becomes dissolved in the solid ferrite matrix according to the following reaction (cf. Ref. [5])



where  $[\text{N}]_{\alpha\text{-Fe}}$  represents the in the ferrite matrix dissolved nitrogen.

The chemical potential (i.e. Gibbs free energy  $\mu$ ) of nitrogen, dissolved in the solid ferrite matrix is defined as

$$\mu_{[\text{N}]_{\alpha\text{-Fe}}, \text{s}} \equiv \mu_{[\text{N}]_{\alpha\text{-Fe}}, \text{s}}^{\circ} + RT \ln a_{[\text{N}]_{\alpha\text{-Fe}}} \quad (1.2)$$

where  $\mu_{[\text{N}]_{\alpha\text{-Fe}}, \text{s}}^{\circ}$  denotes the chemical potential of nitrogen in the solid (s) reference state (i.e. ferrite),  $a_{[\text{N}]_{\alpha\text{-Fe}}}$  represents the activity of nitrogen in the dissolved state with respect to the reference state (in the reference state  $a_{[\text{N}]_{\alpha\text{-Fe}}} = 1$ ),  $R$  is the gas constant and  $T$  the absolute temperature.  $\mu_{[\text{N}]_{\alpha\text{-Fe}}, \text{s}}^{\circ}$  is temperature dependent at the selected pressure of the reference state. There is no precondition for the selection of the reference state. Hence, the relevant reference state must be specified for the discussion of activities.

In a gas mixture the chemical potential of a gaseous constituent  $i$  is defined by

$$\mu_{i, \text{g}} \equiv \mu_{i, \text{g}}^{\circ} + RT \ln \left( \frac{f_i}{f_i^{\circ}} \right) \quad (1.3)$$

where  $\mu_{i, \text{g}}^{\circ}$  is the chemical potential of  $i$  in the gaseous (g) reference state (temperature dependent at the selected pressure of the reference state),  $f_i$  denotes the fugacity of  $i$

in the gas mixture and  $f_i^\circ$  represents the fugacity of  $i$  in the reference state. Assuming an ideal behaviour of the considered gases or constant fugacity coefficients equation (1.3) can be written as

$$\mu_{i, g} \equiv \mu_{i, g}^\circ + RT \ln \left( \frac{p_i}{p_i^\circ} \right) \quad (1.4)$$

where  $p_i$  is the partial pressure of  $i$  and  $p_i^\circ$  represents the pressure of  $i$  in the reference state.

Thermodynamic equilibrium between solid ferrite and the ammonia/hydrogen gas mixture requires that the chemical potentials of nitrogen in the gas phase and in the solid phase (i.e. specimen surface) are equal. If this prevails, it follows on the basis of equations (1.1) to (1.4)

$$\mu_{\text{NH}_3, g} = \mu_{[\text{N}]_{\text{a-Fe}}, s} + \frac{3}{2} \mu_{\text{H}_2, g} \quad (1.5)$$

and from equation (1.5) it follows

$$\mu_{[\text{N}]_{\text{a-Fe}}, s} = \mu_{\text{NH}_3, g}^\circ - \frac{3}{2} \mu_{\text{H}_2, g}^\circ + RT \ln \left( \frac{p_{\text{NH}_3}}{p_{\text{H}_2}^{3/2}} \right) \quad (1.6)$$

where it should be emphasised that the pressure of the reference state is selected as one atmosphere ( $p_i^\circ = 1 \text{ atm}$ ) and  $p_i$  must have the same unit as  $p_i^\circ$  (i.e. atmospheres). Hence, the activity of nitrogen dissolved in the solid at a constant temperature is controlled by the ratio

$$r_{\text{N}} = \left( \frac{p_{\text{NH}_3}}{p_{\text{H}_2}^{3/2}} \right), \quad (1.7)$$

which is called *nitriding potential* (in German “Nitrierkennzahl”). The nitriding potential (i.e. nitrogen activity at the specimen surface) can be adjusted by the composition of the gas mixture in the flow-through furnace. The composition of the gas mixture (i.e. mole fractions of ammonia and hydrogen) can be controlled to a high degree of accuracy with well calibrated mass-flow controllers (variance within 1 % of the adjusted value in ml/min). Besides temperature and time the nitriding potential is the most decisive, independent parameter for a controlled nitriding processing.



The assumption of local equilibrium at the specimen surface between dissolved nitrogen in the ferrite matrix and the ammonia/hydrogen gas mixture implies that  $N_2$  gas formation



effectively does not occur. To maintain this assumption the gas-flow velocity is chosen that high (i.e. 13.5 mm/s at room temperature) that a significant ammonia decomposition is avoided. Since the tendency for this reaction at atmospheric pressure is strong at higher nitriding temperatures [4, 5], the neglect of  $N_2$  gas formation from dissolved nitrogen at the specimen surface requires that the kinetics of this reaction proceeds very slowly, as compared with the development of the equilibrium in equation (1.1), so that the activity of nitrogen at the specimen surface is determined by the local equilibrium of equation (1.1). This is the case for the in this thesis applied parameters (i.e. flow-through principle with appropriate gas-flow velocity; cf. above).

Further, it can be assumed that the kinetics of the thermal decomposition of ammonia into nitrogen and hydrogen gas



in the nitriding atmosphere is such slow that sufficiently high gas exchange rates in the furnace (flow-through principle) achieve a significant nitriding potential [5] (cf. equation (1.7)).

### 1.1.3 The Fe–N phase diagram

Phase diagrams normally describe the thermodynamically stable conditions of systems as a function of temperature and composition at constant pressure. A part of the standard Fe–N phase diagram [7] is shown in Fig. 1.4. The ferrite ( $\alpha$ -Fe) and austenite ( $\gamma$ -Fe) phase fields, and the  $\gamma'$ -Fe<sub>4</sub>N<sub>1-x</sub> and  $\epsilon$ -Fe<sub>3</sub>N<sub>1+y</sub> phase fields are indicated. It is important to realise that Fig. 1.4 does not describe the equilibrium between Fe and N<sub>2</sub> at atmospheric pressure [6].

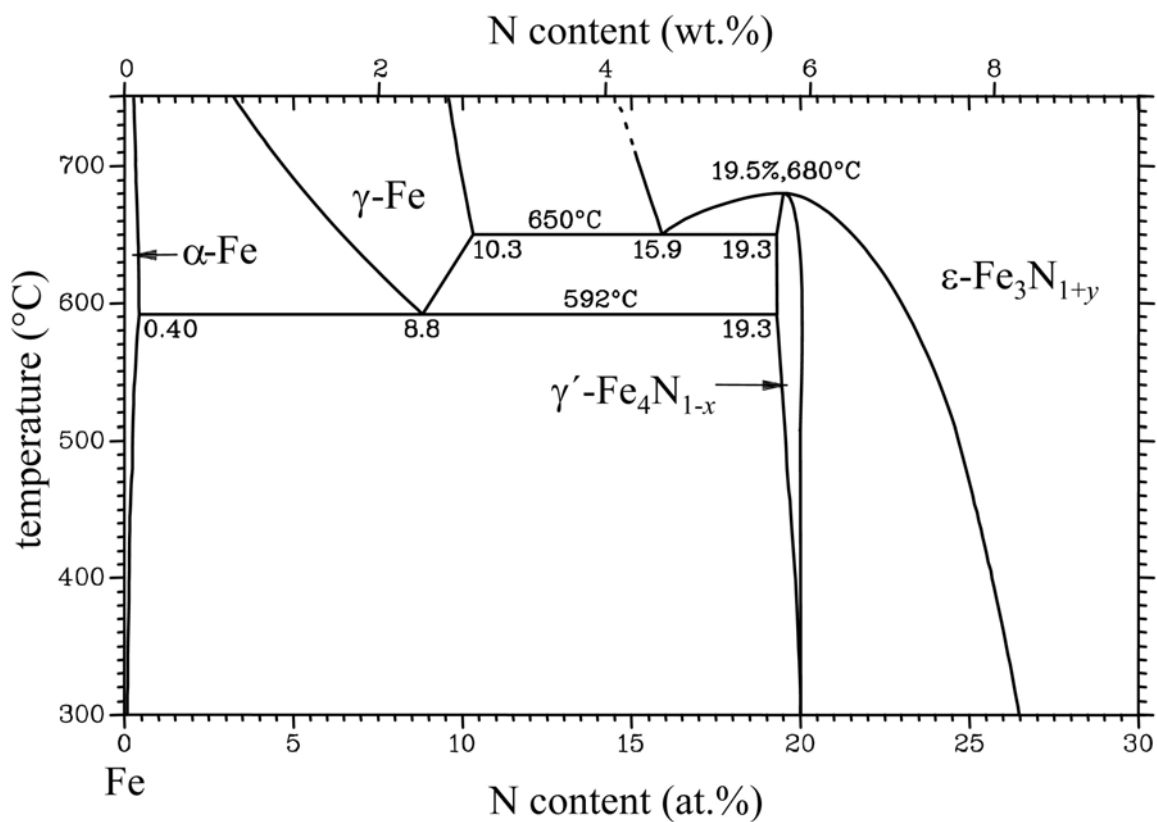


Fig. 1.4: Part of the metastable Fe–N phase diagram, redrawn from Ref. [7].

A more generally interpretation of Fig. 1.4 is that the Fe–N phase diagram represents the equilibria between Fe and a medium of largely variable chemical potential of nitrogen (cf. section 1.1.2). An equilibrium can only occur at the interface between Fe and such a medium. At normal temperatures and pressures the iron nitrides (e.g.  $\gamma'$ -Fe<sub>4</sub>N<sub>1-x</sub> and  $\epsilon$ -Fe<sub>3</sub>N<sub>1+y</sub>) have a strong tendency for decomposition into Fe and N<sub>2</sub> [5, 6].

### 1.1.4 Nitriding potential and Lehrer diagram

The nitriding potential  $r_N$  governs the chemical potential of nitrogen in the gas phase and, hence, the activity of nitrogen dissolved in Fe at the interface between Fe and the ammonia/hydrogen gas mixture (cf. section 1.1.2). According to Fig. 1.4, which shows the phase fields for the Fe–N system classically as temperature over nitrogen concentration, Lehrer determined the borders of the Fe–N phase fields with respect to the temperature and the nitriding potential and drew the so called Lehrer diagram [8]. Such a Lehrer diagram is depicted in Fig. 1.5. Besides the phase boundaries, the Lehrer diagram in Fig. 1.5 shows additionally lines of constant nitrogen concentration (i.e. isoconcentration lines) [9]. In this way extended Lehrer diagram provides not only the adjustment of a certain phase but also of a certain nitrogen concentration at the Fe specimen surface.

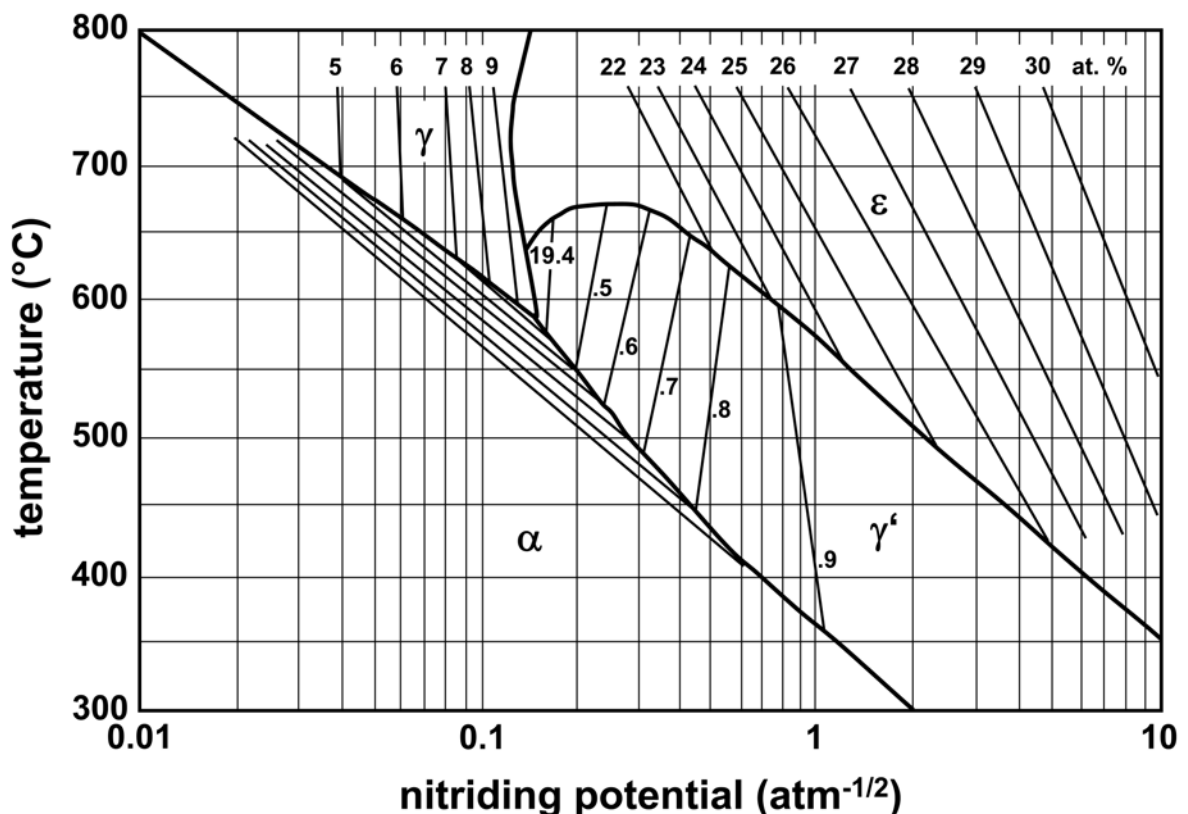


Fig. 1.5: Lehrer diagram with isoconcentration lines, redrawn according to Ref. [9], indicating the equilibrium Fe–N phase fields with respect to the temperature and the nitriding potential at the Fe/gas atmosphere interface.

### 1.1.5 Morphology of the nitrated zone

It is assumed that the growth of the nitrated zone during nitriding is controlled by the diffusion of nitrogen atoms over the octahedral interstices of the iron sublattice [6]. A local equilibrium between dissolved nitrogen in the ferrite matrix and the ammonia/hydrogen gas mixture is only achieved at the specimen surface. Beneath the surface the nitrogen concentration decreases, due to inward diffusion, and hence the chemical potential of nitrogen in ferrite decreases with increasing depth.

If the chemical potential of nitrogen in the nitriding medium does not allow the development of iron nitrides (cf. section 1.1.2; cf. Figs. 1.4 and 1.5), the nitrated zone consists only of ferrite with a concentration depth gradient of dissolved nitrogen (see  $\alpha$ -Fe region in Fig. 1.6 and consider the maximum nitrogen solubility in ferrite in Fig. 1.4). If the nitriding potential allows iron nitride formation, it depends on the local equilibrium concentration of nitrogen at the surface (cf. Figs. 1.4 and 1.5) whether a closed layer of  $\gamma'$  iron nitride develops or a layer of  $\epsilon$  iron nitride together with  $\gamma'$  iron nitride beneath. The local nitrogen concentrations at the  $\epsilon/\gamma'$  interface and at the  $\gamma'/\alpha$  interface (cf. arrows in Fig. 1.6) correspond with the according equilibrium nitrogen concentrations in the Fe–N phase diagram (cf. Fig. 1.4).

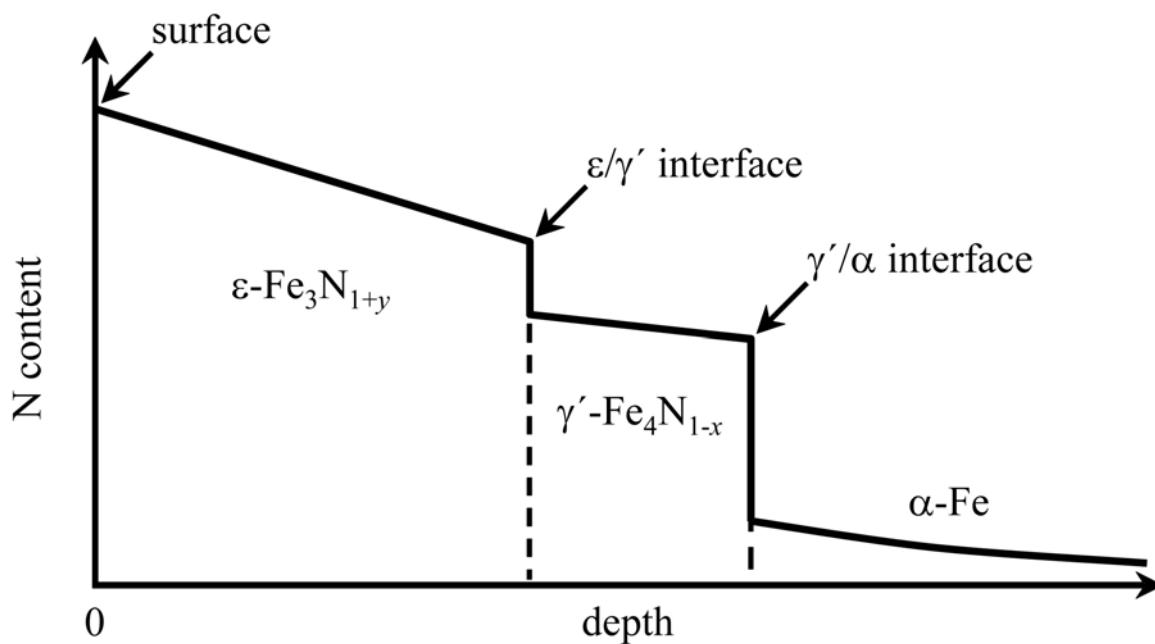


Fig. 1.6: Schematic nitrogen concentration depth profile of the nitrated zone of a pure  $\alpha$ -Fe matrix.

### 1.1.6 Constitution of the nitrided zone

The formation of nitrides upon nitriding changes the microstructure of the ferrite matrix in the nitrided zone of the specimen, made of pure iron, an iron-based alloy or steel. With respect to the present nitrides and the layer constitution the nitrided zone can be subdivided into the *compound layer* and the *diffusion zone* (cf. Fig. 1.7).

The compound layer is a closed layer at the specimen surface consisting of the hcp  $\epsilon$  iron nitride together with fcc  $\gamma'$  iron nitride beneath or only  $\gamma'$  iron nitride without  $\epsilon$  iron nitride above (cf. section 1.1.5). The demanded tribological and anti-corrosion properties of nitrided specimens are benefited by the compound layer [3, 5, 10, 11].

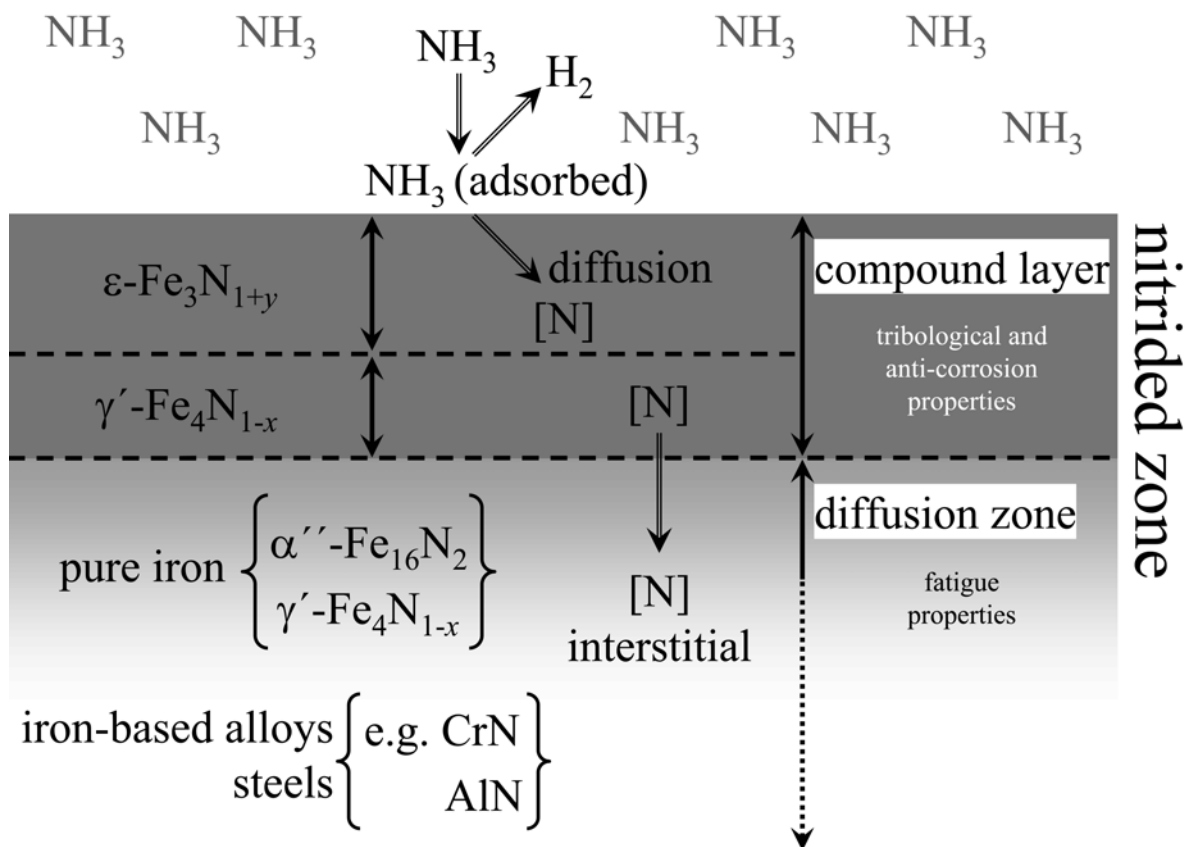


Fig. 1.7: Schematic illustration of the nitriding process at the specimen surface (pure iron or iron-based alloy).

The part of the nitrided zone beneath the compound layer, in which nitrogen largely is dissolved interstitially in the ferrite matrix, is called “diffusion zone”. In the diffusion zone of pure  $\alpha$ -Fe, precipitates of  $\gamma'\text{-Fe}_4\text{N}_{1-x}$  and  $\alpha''\text{-Fe}_{16}\text{N}_2$  can be present [12, 13]. In case of iron-based alloys or steels, containing nitride forming elements such as Ti, V, Mo, Cr or Al, so called “inner nitrides” can precipitate, which are to a large extent responsible for an improvement of the fatigue behaviour [14-18].

### 1.1.7 Excess nitrogen

The nitrogen uptake upon nitriding of a ferritic, iron-based alloy leads to the formation of (inner) nitride precipitates and the dissolution of nitrogen in the ferritic iron matrix. However, quantitative investigations revealed that nitrated, iron-based alloys take up more nitrogen than necessary for the precipitation of the stoichiometric nitrides and the equilibrium dissolution of nitrogen in the pure, unstrained ferrite lattice [19]. The additionally present nitrogen is called “excess nitrogen” [16, 18, 19].

Excess nitrogen atoms can be located at several sites: (i) adsorbed at the interface between the nitride precipitates and the ferrite matrix [16, 18, 19], (ii) additionally dissolved in octahedral interstices of the strained ferrite lattice, due to a lattice misfit between inner nitride precipitates and the ferrite matrix, which increases the nitrogen solubility [20] and (iii) trapped at dislocations [21]. If an iron-based alloy is nitrated under conditions so that no iron nitrides can be formed at the surface (i.e. the nitriding potential is chosen sufficiently low; cf. above), the total nitrogen uptake  $[N]_{\text{total}}$  of the alloy can be given as

$$[N]_{\text{total}} = [N]_{\text{MeN}} + [N]_{\alpha\text{-Fe}}^0 + [N]_{\text{interface}} + [N]_{\text{strain}} + [N]_{\text{dislocation}} \quad (1.10)$$

where  $[N]_{\text{MeN}}$  is the (normal) amount of nitrogen incorporated in the  $\text{Me}_x\text{N}_y$  nitride precipitate (Me = e.g. Cr, Al, etc.),  $[N]_{\alpha\text{-Fe}}^0$  is the (normal) equilibrium solubility of nitrogen in the unstrained ferrite matrix corresponding to the applied nitriding parameters (i.e. temperature and nitriding potential; cf. above),  $[N]_{\text{interface}}$  is the (excess) nitrogen adsorbed at the precipitate/matrix interface,  $[N]_{\text{strain}}$  is the additional (excess) nitrogen dissolved due to the misfit stress field in the ferrite matrix lattice and  $[N]_{\text{dislocation}}$  is the (excess) nitrogen trapped at dislocations (cf. above). Hence the total amount of excess nitrogen is the following sum

$$[N]_{\text{total}}^{\text{excess}} = [N]_{\text{interface}} + [N]_{\text{strain}} + [N]_{\text{dislocation}} \quad (1.11)$$

The total amount of excess nitrogen  $[N]_{\text{total}}^{\text{excess}}$  can be subdivided into two types: (i) mobile excess nitrogen, i.e.  $[N]_{\text{strain}}$ , and (ii) immobile excess nitrogen, i.e.  $[N]_{\text{interface}}$  and  $[N]_{\text{dislocation}}$  [21].

A significant part of the immobile excess nitrogen in nitrated binary iron-based alloys has been suggested to be adsorbed at the nitride/matrix interface [16, 18, 19, 21-23], i.e.  $[N]_{\text{interface}}$ . The amount of  $[N]_{\text{interface}}$  depends on the total precipitate/matrix interfacial area and on the interface structure (e.g. shape and morphology of the inner nitride precipitates and their orientation relationship with the ferrite matrix, coherency and incoherency).

The amount of immobile excess nitrogen trapped at dislocations  $[N]_{\text{dislocation}}$  depends on the dislocation density in the material (cf. cold-rolled ferrite matrix versus recrystallised ferrite matrix).

The amount of mobile excess nitrogen additionally dissolved in the strained ferrite lattice  $[N]_{\text{strain}}$  depends on the lattice misfit between inner nitride precipitates and the ferrite matrix, which causes a dilatation of the matrix lattices due to elastic accommodation. A model, which predicts the amount of  $[N]_{\text{strain}}$  can be found in Ref. [19].

### 1.1.8 Residual stresses

Residual stresses are self-equilibrating stresses existing in materials under uniform temperature conditions without external loading [24]. They often arise in materials in consequence of processing steps such as heat treatment or machining [25]. Residual stresses can have many different origins (e.g. mechanical, thermal, plastic or due to phase transformation such as inner nitride precipitation) but they are all the result of misfit [26]. These misfits can occur between different parts, different phases, or different regions within the same part. Depending on the scale over which they self-equilibrate residual stresses can be subdivided into *macro stresses* and *micro stresses* [27]. Macro stresses vary continuously over large distances and are also denominated as residual stresses of type I. Micro stresses are residual stresses of type II, which vary over the grain scale (intergranular stresses), and residual stresses of type III, which vary over the atomic scale. The misfitting regions in case of micro stresses are of microscopic and submicroscopic dimensions. Significant type II stresses occur when the microstructure consists of several phases or due to phase transformations. Type III stresses originate from the coherency misfit strain at interfaces and from dislocation

stress fields. A summary of commonly used techniques for the determination of the above mentioned different kinds of residual stresses are given in Ref. [27].

The influence of residual stresses on the mechanical behaviour of materials can be both, beneficial and detrimental. Nitriding leads to the generation of pronounced internal residual stresses in the diffusion zone of the nitrided layer [28], which have a crucial, beneficial influence on the, amongst others (cf. section 1.1.6), mechanical properties of nitrided specimens. In particular the resistance against fatigue is increased upon nitriding due to the presence of compressive residual stresses, induced by the precipitation of sub-microscopically, coherent inner nitride particles, which tend to expand the ferrite matrix. The presence of compressive residual stresses parallel to the specimen surface in the surface-adjacent region can inhibit crack initiation and crack growth [24, 28].

To understand the development of residual macrostresses in the diffusion zone of the nitrided layer, an extremely simplified description is given in the following: the initial state is an unnitrided specimen (cf. Fig. 1.8 a). During nitriding nitrogen becomes incorporated into the surface of the specimen where it forms inner nitride precipitates with the present nitride-forming elements (e.g. Cr, Al, etc.) in the diffusion zone. In Fig. 1.8 b the nitrided zone and the unnitrided core of the specimen are considered notionally separately. The difference in specific volume between the matrix and the developed nitrides expands the nitrided layer. In fact, (cf. Fig. 1.8 c) the nitrided layer and the unnitrided specimen core are attached to each other and a self-equilibrating stress state has to be reached. As a result of this equilibrium stress state, a residual macrostress state of compressive character is induced in the nitrided zone, whereas a residual macrostress state of tensile character responds in the unnitrided core.



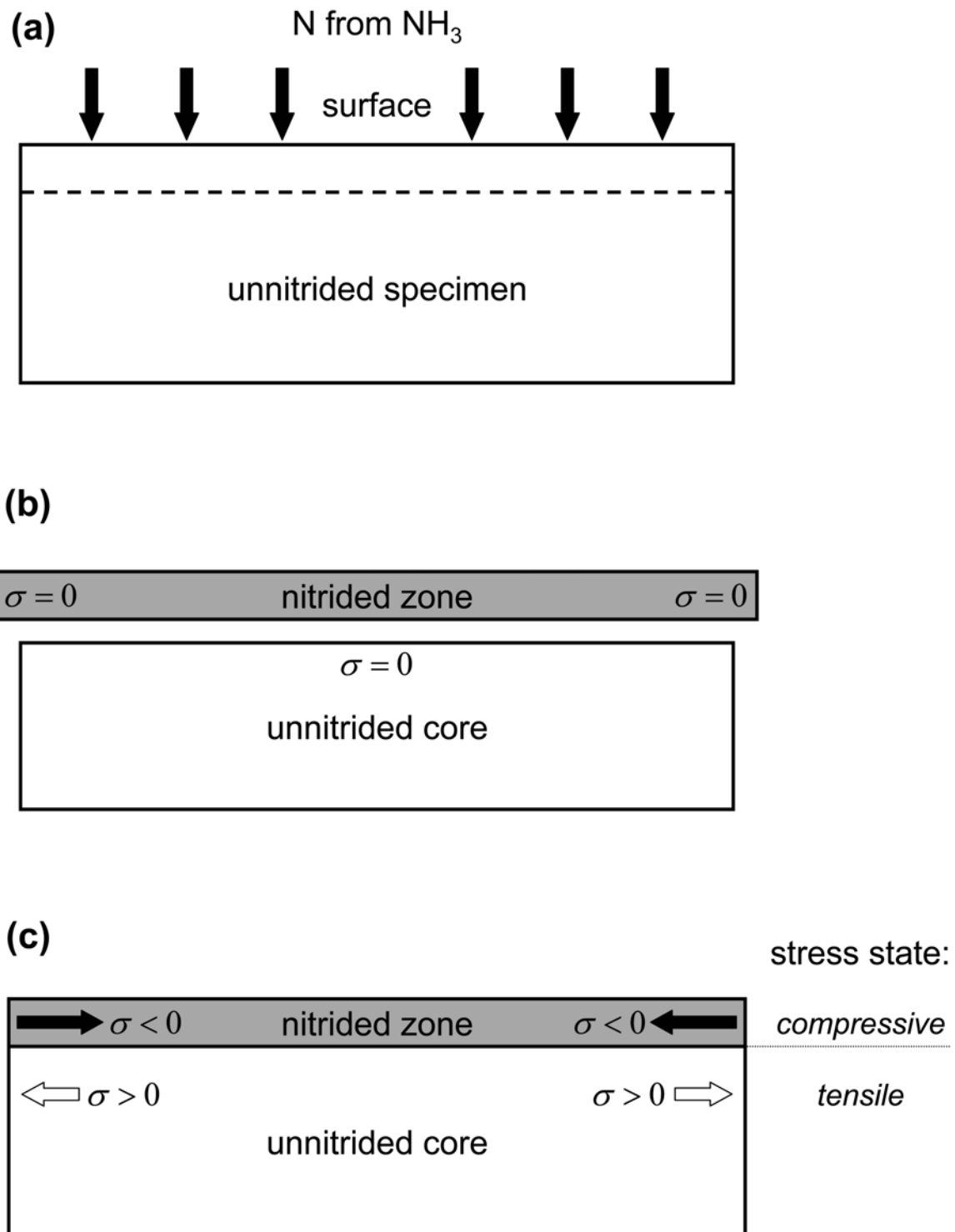


Fig. 1.8: Schematic illustration of the residual macrostress development in a specimen during nitriding. (a) As initial state an unnitrided specimen is considered in which nitrogen becomes incorporated upon nitriding. (b) The formation of inner nitrides in the diffusion zone brings about a theoretical expansion of the nitrided zone (see text). (c) The resulting equilibrium stress state induces a residual stress state of compressive character in the nitrided zone and consequently a residual stress state of tensile character in the unnitrided core beneath.

## 1.2 Aim and outlook of the thesis

As in the previous section already introduced, nitriding of ferritic iron-based alloys is a very important surface engineering process and widely used in industry due to its beneficial influence on the fatigue behaviour and its improvement of the case resistance against wear and corrosion. However, the application practice is still largely based on phenomenology and experience. For this reason there is a great interest in scientific investigations of the processing methods in combination with control and predictability of materials properties.

Investigations of the precipitation behaviour of inner nitrides in the diffusion zone and the corresponding change of the material microstructure and hence material properties have been started on simple, binary iron alloys in the past (e.g. [15-18, 21, 29-49]). Simple, binary alloys provide a very fundamental approach because there is no other interaction than that between nitrogen, nitride-forming elements such as Al, Cr, Ti and V, and the pure iron matrix. In particular the investigation of binary Fe–Cr alloys [17, 31, 38, 39, 41, 42, 44, 48, 50] and Fe–Al alloys [14, 30, 34-36, 46, 51, 52] has been carried out extensively.

The next step in this fundamental, scientific approach towards understanding of the nitriding behaviour of, for example, nitriding steels are ternary iron-based alloys. In the present work the nitriding behaviour of Fe–Cr–Al alloys was investigated. Al together with Cr as nitride-forming elements were chosen since they are commonly used as alloying elements in typical nitriding steels. At the beginning of this work different Fe–Cr–Al alloys were investigated after gaseous nitriding by X-ray diffraction analysis, electron probe microanalysis, microhardness measurement and classical metallography to get information about the precipitated inner nitride phases and the microstructure. Although the reaction of the alloy specimens with the nitriding atmosphere was apparent (e.g. plastic deformation of the specimens, brittleness, open grain boundaries and a significant hardness increase), it was difficult to identify the composition and microstructure of the inner nitride precipitates with the above mentioned methods. The application of several transmission electron microscopy methods (high resolution and scanning transmission electron microscopy) finally

provided a deep insight into the microstructure and composition of the developed inner nitrides.

Chapter 2 presents results concerning the investigation of the microstructure and the elemental composition of inner nitride precipitates after gaseous nitriding of a recrystallised, ternary alloy with the composition Fe–1.5wt.%Cr–1.5wt.%Al (i.e. Fe–1.6at.%Cr–3.1at.%Al). It could be shown that upon nitriding tiny, platelet-like precipitates develop of a metastable, mixed  $\text{Cr}_{1-x}\text{Al}_x\text{N}$  phase instead of the two binary, equilibrium inner nitride phases CrN in the cubic, rock-salt structure and AlN in the hexagonal wurtzite structure. The mixed  $\text{Cr}_{1-x}\text{Al}_x\text{N}$  precipitates are of cubic, rock-salt structure type and obey a Bain-type orientation relationship [53] with the ferrite matrix. The precipitate platelets are smallest at the nitrated surface and become coarser with increasing nitriding depth. Coarser precipitates at large nitriding depths start to lose their coherency with the ferrite matrix and do not fulfil the Bain orientation relationship exactly. For this reason the large uptake of excess nitrogen has its maximum at the nitrated surface due to the presence and homogeneous distribution of very thin, coherent precipitate platelets. Besides the presence of mobile excess nitrogen, which is additionally dissolved in the elastically strained ferrite matrix, immobile excess nitrogen at octahedral interstices in the ferrite matrix adjacent to the platelet faces is bonded to Cr and preferentially to Al.

In Chapter 3 the decomposition and structural transformation of the metastable  $\text{Cr}_{1-x}\text{Al}_x\text{N}$  precipitates in nitrated Fe–1.5wt.%Cr–1.5wt.%Al specimens upon annealing at higher temperature than the nitriding temperature have been studied. It could be revealed that the mixed, ternary  $\text{Cr}_{1-x}\text{Al}_x\text{N}$  precipitates in the nitrated layer decompose, at least partially, which leads to the development of the equilibrium precipitates CrN of cubic, rock-salt structure type obeying the Bain orientation relationship with the ferrite matrix and AlN in the hexagonal, wurtzite structure type obeying a Pitsch–Schrader orientation relationship [54] with the ferrite matrix. The precipitation of the equilibrium AlN phase was observed both in the interior and at grain boundaries of the matrix. The coherency of inner nitride platelets decreases due to coarsening and transformation of the precipitates. Coarsening of the precipitates and decreasing of the coherency leads to a decreased capacity for excess nitrogen in the ferrite matrix. It was observed that mobile excess nitrogen diffuses during annealing from the nitrated layer

into the initially unnitrided specimen core. There the binary equilibrium nitrides CrN in the cubic, rock-salt structure and AlN of the hexagonal, wurtzite structure type develop immediately.

Chapter 4 gives additional insight into the microstructure of the diffusion zone of nitrated Fe-1.5wt.%Cr-1.5wt.%Al specimens. The size of the mixed  $\text{Cr}_{1-x}\text{Al}_x\text{N}$  precipitates and the presence of excess nitrogen have a strong influence on this microstructure. The precipitates in the surface adjacent region have a higher local density and a smaller size than at larger depths in the diffusion zone (cf. above). This brings about the occurrence of residual stress and an enhanced uptake of excess nitrogen in the surface adjacent region. After a certain nitrating time crack formation occurred starting from the specimen surface and propagating along grain boundaries perpendicularly to the surface towards larger depths. The observed grain boundary brittleness could be ascribed to the development of nitrogen gas at grain boundaries and the segregation of aluminium promoting the precipitation of AlN at grain boundaries. A Segregation of chromium could not be observed. A simple model has been proposed based on a determined residual stress-depth profile and the occurrence of plastic deformation in the surface adjacent region to explain the unexpected initially occurrence of tensile stress parallel to the specimen surface in the diffusion zone, which induces the crack formation.

## References

- [1] H. J. Spies, HTM 59 (2004) 78-86.
- [2] S. Lampman (1991). Introduction to surface hardening of steel. ASM Handbook: Heat Treating. Metals Park, Ohio, ASM International. 4: 259-267.
- [3] D. Liedtke, U. Baudis, J. Boßlet, U. Huchel, H. Klümper-Westkamp, W. Lerche and H. J. Spies, Wärmebehandlung von Eisenwerkstoffen Nitrieren und Nitrocarburieren, Renningen, Expert Verlag (2006).
- [4] H. J. Grabke, Ber. Bunsenges. Physik. Chem. 72 (1968) 533-541.
- [5] E. J. Mittemeijer and J. T. Slycke, Surf. Eng. 12 (1996) 152-162.
- [6] E. J. Mittemeijer and M. A. J. Somers, Surf. Eng. 13 (1997) 483-497.
- [7] H. A. Wriedt, N. A. Gokcen and R. H. Nafziger, Bull. Alloy Phase Diagrams 8 (1987) 355-377.
- [8] E. Lehrer, Z. Elektrochem. 36 (1930) 383-392.
- [9] R. Hoffmann, E. J. Mittemeijer and M. A. J. Somers, HTM 51 (1996) 162-169.
- [10] C. H. Knerr, T. C. Rose and J. H. Filkowski (1991). Gas nitriding. ASM Handbook: Heat Treating. J. R. Davis, G. M. Davidson, S. R. Lampman, T. B. Zorc, J. L. Daquila, A. W. Ronke, K. L. Henniger and R. C. Uhl. Metals Park, Ohio, ASM International. 4: 387-409.
- [11] E. J. Mittemeijer and J. Grosch, Eds. Proceedings of 'AWT-Tagung Nitrieren und Nitrocarburieren', Arbeitsgemeinschaft Wärmebehandlung und Werkstofftechnik e.V., Wiesbaden (1991).
- [12] D. H. Jack and K. H. Jack, Mater. Sci. Eng. 11 (1973) 1-27.
- [13] U. Dahmen, P. Ferguson and K. H. Westmacott, Acta Metall. 35 (1987) 1037-1046.
- [14] H. H. Podgurski, R. A. Oriani, F. N. Davis, J. C. M. Li and Y. T. Chou, Trans. TMS-AIME 245 (1969) 1603-&.
- [15] M. Pope, P. Grieveson and K. H. Jack, Scand. J. Metall. 2 (1973) 29-34.
- [16] D. H. Jack, Acta Metall. 24 (1976) 137-146.
- [17] P. M. Hekker, H. C. F. Rozendaal and E. J. Mittemeijer, J. Mater. Sci. 20 (1985) 718-729.

- [18] D. S. Rickerby, S. Henderson, A. Hendry and K. H. Jack, *Acta Metall.* 34 (1986) 1687-1699.
- [19] M. A. J. Somers, R. M. Lankreijer and E. J. Mittemeijer, *Philos. Mag. A* 59 (1989) 353-378.
- [20] H. A. Wriedt and L. S. Darken, *Trans. TMS–AIME* 233 (1965) 111-121.
- [21] S. S. Hosmani, R. E. Schacherl and E. J. Mittemeijer, *Acta Mater.* 54 (2006) 2783-2792.
- [22] H. H. Podgurski and F. N. Davis, *Acta Metall.* 29 (1981) 1-9.
- [23] M. H. Biglari, C. M. Brakman, E. J. Mittemeijer and S. van der Zwaag, *Philos. Mag. A* 72 (1995) 931-947.
- [24] E. Macherauch and K. H. Kloos (1987). Origin, measurement and evaluation of residual stresses. *Residual stresses in science and technology*. E. Macherauch and V. Hauk. Oberursel, DGM Informationsgesellschaft mbH. 1: 3-26.
- [25] I. C. Noyan and J. B. Cohen, *Residual stress: measurement by diffraction and interpretation*, Berlin, Springer (1987).
- [26] P. J. Withers and H. K. D. H. Bhadeshia, *Materials Science and Technology* 17 (2001) 366-375.
- [27] P. J. Withers and H. K. D. H. Bhadeshia, *Materials Science and Technology* 17 (2001) 355-365.
- [28] E. J. Mittemeijer, *J. Met.* 37 (1985) 16-20.
- [29] V. A. Phillips and A. U. Seybolt, *Trans. TMS–AIME* 242 (1968) 2415-2422.
- [30] H. H. Podgurski and H. E. Knechtel, *Trans. TMS–AIME* 245 (1969) 1595-1602.
- [31] B. Mortimer, P. Grieveson and K. H. Jack, *Scand. J. Metall.* 1 (1972) 203-209.
- [32] Y. M. Lakhtin, N. V. Silina and V. A. Fedchun, *Metal Science and Heat Treatment* 19 (1977) 3-8.
- [33] E. J. Mittemeijer, A. B. P. Vogels and P. J. Vanderschaaf, *J. Mater. Sci.* 15 (1980) 3129-3140.
- [34] M. H. Biglari, C. M. Brakman, M. A. J. Somers, W. G. Sloof and E. J. Mittemeijer, *Z. Metallk.* 84 (1993) 124-131.
- [35] M. H. Biglari, C. M. Brakman and E. J. Mittemeijer, *Philos. Mag. A* 72 (1995) 1281-1299.

- [36] M. H. Biglari, C. M. Brakman, E. J. Mittemeijer and S. van der Zwaag, *Metall. Mater. Trans. A* 26 (1995) 765-776.
- [37] J. S. Steenaert, M. H. Biglari, C. M. Brakman, E. J. Mittemeijer and S. van der Zwaag, *Z. Metallk.* 86 (1995) 700-705.
- [38] N. G. Chechenin, P. M. Bronsveld, A. Chezan, C. B. Craus, D. O. Boerma, J. T. M. De Hosson and L. Niesen, *Phys. Status Solidi A-Appl. Mat.* 177 (2000) 117-125.
- [39] R. E. Schacherl, P. C. J. Graat and E. J. Mittemeijer, *Z. Metallk.* 93 (2002) 468-477.
- [40] R. E. Schacherl, P. C. J. Graat and E. J. Mittemeijer, *Metall. Mater. Trans. A* 35A (2004) 3387-3398.
- [41] M. Sennour, P. H. Jouneau and C. Esnouf, *J. Mater. Sci.* 39 (2004) 4521.
- [42] S. S. Hosmani, R. E. Schacherl and E. J. Mittemeijer, *Materials Science and Technology* 21 (2005) 113-124.
- [43] S. S. Hosmani, R. E. Schacherl and E. J. Mittemeijer, *Acta Mater.* 53 (2005) 2069-2079.
- [44] R. E. Schacherl, P. Zieba and E. J. Mittemeijer, *Diffusion in Materials: Dimat 2004, Pt 1 and 2* 237-240 (2005) 1270-1274.
- [45] S. S. Hosmani, R. E. Schacherl and E. J. Mittemeijer, *Metallurgical and Materials Transactions a-Physical Metallurgy and Materials Science* 38A (2007) 7-16.
- [46] S. Meka, S. S. Hosmani, A. R. Clauss and E. J. Mittemeijer, *Int. J. Mater. Res.* 99 (2008) 808-814.
- [47] N. E. Vives Diaz, S. S. Hosmani, R. E. Schacherl and E. J. Mittemeijer, *Acta Mater.* 56 (2008) 4137-4149.
- [48] N. E. Vives Diaz, R. E. Schacherl and E. J. Mittemeijer, *Int. J. Mater. Res.* 99 (2008) 150-158.
- [49] N. E. Vives Diaz, R. E. Schacherl, L. F. Zagonel and E. J. Mittemeijer, *Acta Mater.* 56 (2008) 1196-1208.
- [50] S. S. Hosmani, R. E. Schacherl and E. J. Mittemeijer, *Int. J. Mater. Res.* 97 (2006) 1545-1549.
- [51] K. Bohnenkamp, *Arch. Eisenhüttenw.* 38 (1967) 433-437.

- 
- [52] H. J. Spies, H. Biermann and A. Fischer, *Z. Metallk.* 96 (2005) 781-786.
- [53] E. C. Bain, *Trans. AIME* 70 (1924) 25-46.
- [54] W. Pitsch and A. Schrader, *Arch. Eisenhüttenw.* 29 (1958) 715-721.



## Chapter 2

# **Crystal structure and morphology of mixed $\text{Cr}_{1-x}\text{Al}_x\text{N}$ nitride precipitates; gaseous nitriding of a Fe–1.5wt.%Cr–1.5wt.%Al alloy**

*A. R. Clauss, E. Bischoff, S. S. Hosmani, R. E. Schacherl and E. J. Mittemeijer*

### **Abstract**

The crystal structure and morphology of nitride precipitates, developing in the matrix of a Fe–1.5wt.%Cr–1.5wt.%Al (Fe–1.6at.%Cr–3.1at.%Al) alloy upon gas nitriding, were investigated. To this end the nitrided zone was studied employing metallographic methods, X-ray diffractometry, electron probe microanalysis, microhardness measurement and (high resolution and scanning) transmission electron microscopy. Furthermore, a nitrogen absorption isotherm was determined to characterise the nature of the nitride-precipitation process. It could be shown that mixed  $\text{Cr}_{1-x}\text{Al}_x\text{N}$  nitride precipitates of the cubic, rock-salt structure type develop upon nitriding the ternary alloy. These precipitates obey a Bain-type orientation relationship with the ferrite matrix and are associated with a considerable uptake of excess nitrogen and a very pronounced hardness increase.

### **2.1 Introduction**

Nitriding is an important thermochemical surface engineering process of ferritic steel workpieces to improve the resistance against fatigue, wear and corrosion [1-4]. Although this treatment is widely used in industry, the application practice is largely based on phenomenology. The presence of alloying elements like Al, Cr, Ti and V, which have a strong affinity for nitrogen, can lead to the formation of nitride precipitates in the ferrite matrix, which, by mechanical strengthening, are to a large extent responsible for the resulting strongly improved mechanical performance.

Until now nitride precipitates in ferrite matrices have only been investigated in detail for simple *binary* iron-based alloys (see, e.g., Refs. [5-8]). In practice, however, more than one alloying element with affinity for nitrogen occurs in technical alloys. In particular Al and Cr are used together as alloying elements in typical nitriding steels. Hence, a strong technological interest stimulates the investigation of the composition, structure and shape of nitride precipitates in such multicomponent alloys. At the same time a pronounced fundamental, scientific importance for such research exists as well, as indicated later (section 2.1.2).

### 2.1.1 Nitrides in binary ferritic alloys

A significant amount of research on the nitriding of binary iron-based alloys has been done in the past and also recent years. The formation of platelet-like nitride precipitates obeying the Bain-type orientation relationship (OR) [9] (sometimes also called after Baker and Nutting [10]) during nitriding of binary low alloyed ferritic irons has been observed for pure Fe–Cr, Fe–V, Fe–Ti and Fe–Mo alloys [7, 11-13]. The nitride-precipitation kinetics during (gaseous) nitriding has been classified according to the type of alloying element-nitrogen interaction (weak, intermediate, strong) [14].

Nitriding of binary Fe–Cr alloys [6, 11, 15-21] and Fe–Al alloys [5, 22-28] has been investigated rather extensively. Three modifications of chromium nitride can be distinguished: (i) the cubic, rock-salt structure type CrN, (ii) the hexagonal structure type Cr<sub>2</sub>N and (iii) an orthorhombic CrN modification, which occurs only at very low temperatures (cryogenic modification) and is not relevant for nitriding of iron-based alloys [29]. For aluminium nitride also three modifications exist: (i) the at ambient pressure thermodynamically stable hexagonal, wurtzite structure type AlN [29, 30], (ii) the metastable cubic, rock-salt structure type AlN [5] and (iii) the metastable zinc blende structure type AlN [31, 32], which has never been observed in nitrided iron-based alloys. In ferritic Fe–Cr alloys the formation of cubic, rock-salt structure type CrN platelets with a Bain-type OR with the ferrite matrix was observed [11, 33]. In annealed Fe–Al alloys the nucleation of the thermodynamically stable hexagonal wurtzite structure type AlN is difficult [23, 25, 26, 34]. Transmission electron microscopy results of Biglari et al. [5] from a Fe–2at.%Al alloy revealed the presence

of two AlN modifications after long-time nitriding: (i) the hexagonal wurtzite structure type AlN exhibiting a Pitsch–Schrader [35] OR with the ferrite matrix and (ii) the cubic, rock-salt structure type AlN showing a Bain OR with the ferrite matrix.

Upon nitriding of ferritic iron-based alloys more nitrogen is taken up than necessary for the formation of nitride precipitates and for the dissolution of nitrogen in a pure unstrained ferrite matrix. This additional nitrogen present in the nitrided zone is called “excess nitrogen” [36].

### **2.1.2 Nitrides in ternary ferritic alloys**

There is sparse and ambiguous information about the nitriding behaviour of iron-based alloys containing both Cr and Al as alloying elements and work on the nitriding of the ternary system Fe–Cr–Al lacks at all. In a nitrided Cr–Al medium-carbon steel, “distorted” platelets approximately parallel to  $\{001\}_{\alpha\text{-Fe}}$  matrix planes were observed [37]. After nitriding of low carbon Al and Cr containing steels, besides iron nitrides and hexagonal AlN, the formation of a fcc Me<sub>x</sub>N nitride ( $x \approx 1$ ) with Me containing Al and presumably Cr was reported [38]. Investigation of nitrided (Cr, Al, Ni)- and (Cr, Al, Mn)-containing nitriding steels suggested the formation of tiny coherent platelet-like mixed (i.e. Cr and Al containing) nitrides with a distinct orientation relationship (i.e. Bain) to the ferrite matrix [39-41], but evidence for simultaneous occurrence of Cr and Al in the nitride precipitates was not provided.

The present paper describes the nitriding behaviour of a recrystallised ternary Fe–Cr–Al alloy: Fe–1.5wt.%Cr–1.5wt.%Al. The gaseous<sup>2</sup> nitriding conditions were chosen such that no iron nitrides develop at the surface: upon nitriding (only) precipitation of alloying element nitrides in the ferritic matrix takes place. The results obtained show that the nitriding behaviour of this ternary Fe–Cr–Al alloy is not given by a simple “addition” of the nitriding behaviours of the bounding binary Fe–Cr and Fe–Al systems. The nitrided samples were investigated with respect to the microstructure, the phase constitution and the element distribution, using X-ray

---

<sup>2</sup> The gaseous nitriding variant enables an accurate adjustment of the thermodynamic condition (chemical potential of nitrogen dissolved in the solid) at the sample surface [4].

diffraction, electron probe microanalysis (EPMA), light microscopy, microhardness measurement (Vickers) and (high resolution and scanning) transmission electron microscopy (HRTEM, STEM and TEM). According to the knowledge of the present authors, this is the first time that on basis of gaseous nitriding of a Fe–Cr–Al alloy the occurrence of tiny platelets of cubic, rock-salt structure type, mixed  $\text{Cr}_{1-x}\text{Al}_x\text{N}$  nitride precipitates, obeying the Bain-type OR with the ferrite matrix, is proven directly by nanoscale analytical methods.

## 2.2 Experimental

### 2.2.1 Specimen preparation

For the production of an alloy with the composition Fe–1.5wt.%Cr–1.5wt.%Al appropriate amounts of pure iron (99.98 wt.%), pure chromium (99.999 wt.%) and pure aluminium (99.999 wt.%) were weighed, pre-alloyed in an arc furnace and melted in an  $\text{Al}_2\text{O}_3$  crucible by means of an inductive furnace under a protective argon gas atmosphere (99.999 vol.%). The melt was cast in a copper mould to obtain a cylindrical rod ( $\varnothing$ : 10 mm,  $l$ : 100 mm). The chemical composition and the amounts of impurities were determined by chemical analysis (inductively coupled plasma – optical emission spectroscopy, carrier gas hot extraction and combustion method); results are shown in Table 2.1.

Table 2.1

Amounts of alloying elements and impurities of the used alloy (balance Fe).

Alloy	Cr		Al		N (wt.%)	O (wt.%)	S (wt.%)	C (wt.%)
	(wt.%)	(at.%)	(wt.%)	(at.%)				
Fe–Cr–Al	$1.52 \pm 0.01$	$1.60 \pm 0.01$	$1.52 \pm 0.01$	$3.09 \pm 0.02$	$< 0.0005$	$0.0043 \pm 0.0004$	$< 0.0010$	$0.0025 \pm 0.0002$

The element distribution (homogeneity) after casting was validated by electron probe microanalysis (EPMA; cf. section 2.2.3.2) line-scans (spot size about 1  $\mu\text{m}$ ) on a polished cross-section of the rod.

The rod was cut into three pieces and the shell of each was removed by grinding. Subsequently the pieces were cleaned with ethanol and water in an ultrasonic bath before they were cold-rolled to sheets of a thickness of about 1 mm. Rectangular specimens ( $20 \times 15 \times 1 \text{ mm}^3$ ) were cut out of these sheets and in each specimen a little

hole was drilled ( $\varnothing$ : 1.5 mm) to hang it up later in the nitriding furnace. The samples were ground, polished and cleaned first with ethanol and finally with water in an ultrasonic bath before encapsulation in a quartz tube under a protective argon gas atmosphere (99.999 vol.%). Subsequently the samples were recrystallised in a muffle furnace for 1 h at a temperature of about 1123 K under a protective gas atmosphere (cf. above). The average grain diameter of the resulting, more or less equiaxed, single-phase microstructure was 22  $\mu\text{m}$ .

## **2.2.2 Nitriding**

Before nitriding, the recrystallised specimen surfaces were polished mechanically (last step 1  $\mu\text{m}$  diamond suspension), cleaned first with ethanol and finally with water in an ultrasonic bath and thereafter dried in a nitrogen gas flow. The nitriding process was performed in a vertical, multizone quartz-tube furnace ( $\varnothing$ : 28 mm) with a  $\text{H}_2/\text{NH}_3$  gas mixture flux of 500 ml/min (purity  $\text{H}_2$ : 99.999 vol.%, purity  $\text{NH}_3$ : > 99.998 vol.%; linear gas velocity at room temperature: 13.5 mm/s) at a temperature of  $(853 \pm 1)$  K. The gas fluxes (455 ml/min  $\text{H}_2$  and 45 ml/min  $\text{NH}_3$ ) were adjusted by mass-flow controllers and correspond to a nitriding potential (cf. Refs. [4] and [42]) of  $r_{\text{N}} = 0.104 \text{ atm}^{-1/2}$ . The nitriding process was stopped by breaking mechanically the quartz fibre at which the specimen was suspended in the furnace so that the specimen fell towards an opened valve into a flask filled with water, flushed with  $\text{N}_2$ , where the specimen was quenched. The nitriding potential was chosen such that no iron nitrides develop at the surface [42], i.e. the nitrated layer consists only of the diffusion zone adjacent to the surface exhibiting alloying element nitride precipitation.

## **2.2.3 Specimen characterisation**

### *2.2.3.1 X-ray diffractometry*

Phase analysis by means of X-ray diffraction (recorded from the surface) of all specimens before and after nitriding was performed applying a PANalytical (formerly Philips) X'Pert Multi-Purpose Diffractometer (MPD) using  $\text{Co-K}\alpha$  radiation and the Bragg-Brentano geometry with a graphite monochromator in the diffracted beam. To improve the crystallite statistics, the specimens were rotated around their surface normal during the measurements. The diffraction-angle range ( $30^\circ \leq 2\theta \leq 140^\circ$ ) was

scanned in steps of  $0.05^\circ$  with a counting time of 10 s per step. For the identification of phases from the diffraction peaks, data of the ICDD data base were used [43].

### 2.2.3.2 Electron probe microanalysis (EPMA)

For the determination of concentration depth profiles EPMA was performed on polished cross-sections of the specimens (embedded in Struers PolyFast, last polishing step: 1  $\mu\text{m}$  diamond suspension) using a Cameca SX100 microprobe (acceleration voltage  $U_a = 15$  kV, current  $I = 100$  nA, spot size about 1  $\mu\text{m}$ ) equipped with five wavelength-dispersive spectrometers. For each specimen at least four line-scans with step size of 3  $\mu\text{m}$  at different locations on the specimen cross-section were performed, perpendicular to the surface, starting from the surface across the cross-section towards the centre of the specimen. To obtain the element contents at each measurement point, the intensities of the characteristic Fe-K $\beta$ , Cr-K $\alpha$ , Al-K $\alpha$  and N-K $\alpha$  X-ray emission peaks were measured and divided by the corresponding intensities obtained from standard samples of pure Fe, Cr, Al and  $\gamma'$ -Fe<sub>4</sub>N (for N-K $\alpha$ ). Elemental concentrations were calculated from the intensity ratios applying the  $\Phi(\rho z)$  approach according to Pouchou and Pichoir [44].

### 2.2.3.3 Light microscopy (LM)

For LM investigations a piece of each nitrided specimen was cut off (Struers Accutom-50, Al<sub>2</sub>O<sub>3</sub> cut-off wheel), embedded in Struers PolyFast, ground and polished (last polishing step: 1  $\mu\text{m}$  diamond suspension). Each cross-section was etched with 1 % or 2.5 % Nital (1 vol.% and 2.5 vol.%, respectively, HNO<sub>3</sub> in ethanol) at a temperature of about 293 K to 323 K for about 30 s to 200 s. LM micrographs were taken using a Zeiss Axiophot microscope equipped with a digital camera (Olympus ColorView IIIu).

### 2.2.3.4 Microhardness measurement

Microhardness measurements at the same sites of the EPMA line-scans on cross-sections of nitrided specimens were carried out with a Vickers microhardness tester (Leica VMHT Mot) applying a load of 147 mN, an indenter speed of 30  $\mu\text{m/s}$  and a dwell time of 10 s. The distance of the indentations on the cross-sections from the

specimen surface and the length of both indentation diagonals were measured on calibrated LM micrographs (cf. Section 2.2.3.3) applying a computer software (analySIS Imaging–Software).

### *2.2.3.5 Transmission electron microscopy (TEM, STEM and HRTEM)*

TEM samples taken at selected depths of the nitrated zone were produced by either the jet-electropolishing technique or by argon ion milling.

Self-supporting (i.e. no special specimen carrier necessary; cf. below) discs ( $\varnothing = 3$  mm) were stamped with a mechanical punch from sheets produced by removing material mechanically from the nitrated surface. These discs were thinned applying the jet-electropolishing technique (bath composition: 85 vol.% acetic acid and 15 vol.% perchloric acid, current:  $250 \text{ mA} \leq I \leq 480 \text{ mA}$ , voltage:  $40 \text{ V} \leq U \leq 85 \text{ V}$ , temperature:  $285 \text{ K} \leq T \leq 295 \text{ K}$ , flow rate corresponding to settings “2” to “7” at a Struers Tenupol–3 apparatus; treatment time  $30 \text{ s} \leq t \leq 300 \text{ s}$ ) and subsequently rinsed in ethanol, acetone and isopropanol. To generate a hole in the middle of the sample, the discs were fixed during the jet-electropolishing treatment between two platinum rings.

It turned out that samples prepared by the jet-electropolishing technique (in particular TEM samples from the near surface region) were hardly electron transparent because of thick rims. Furthermore, due to problems with astigmatism in the used TEM instruments, caused by the ferromagnetism of the samples, and due to the brittleness of the nitrated material, a modified preparation method using a special titanium specimen carrier (i.e. no punched-out discs and hence not self-supporting;  $\varnothing = 3$  mm) in combination with low-angle ion milling based on the method of Barna [45] was applied. The advantage of this method is the reduction of the ferromagnetism due to less specimen mass in the TEM samples. Two pieces of specimen material were mounted vertically in a titanium specimen carrier for cross-sectional view and another piece of specimen material was mounted horizontally in a second titanium specimen carrier for planar view. The material in each titanium specimen carrier was fixed both mechanically and with glue before grinding, dimpling and ion milling (either Bal–Tec RES 010,  $3.5 \text{ kV} \leq U_a \leq 4 \text{ kV}$ ,  $0.7 \text{ mA} \leq I \leq 1 \text{ mA}$ , milling time:  $8 \text{ h} \leq t \leq 30 \text{ h}$ , angle of ion incidence:  $6^\circ$  or Gatan PIPS–691,  $3 \text{ kV} \leq U_a \leq 4 \text{ kV}$ ,  $10 \mu\text{A} \leq I \leq 12 \mu\text{A}$ , milling

time:  $3 \text{ h} \leq t \leq 10 \text{ h}$ , angle of ion incidence:  $8^\circ$ ). The sample stage was cooled by a special cooling system (developed at the Max Planck Institute for Metals Research) made of copper tubes and filled with liquid nitrogen.

Transmission electron microscopy (TEM) investigation was performed using a Philips CM 200 transmission electron microscope operating at 200 kV, equipped with an energy-dispersive X-ray detection system (EDX). Bright field images (BF), dark field (DF) images and selected area diffraction patterns (SADPs) were taken by a CCD camera. The lattice spacings  $d$  were calculated for different  $hkl$  values and phases from the lattice parameters  $a$  as provided by the ICDD data base [43] ( $\alpha$ -Fe:  $a = 0.287 \text{ nm}$ ,  $\text{Fe}_3\text{O}_4$ :  $a = 0.839 \text{ nm}$ , AlN wurtzite:  $a = 0.311 \text{ nm}$ , AlN rock salt:  $a = 0.405 \text{ nm}$ , AlN zinc blende:  $a = 0.434 \text{ nm}$ , CrN rock salt:  $a = 0.414 \text{ nm}$ ). The  $d$  values of AlN rock-salt and CrN rock-salt structures are so close to each other that it is very difficult to distinguish these phases in TEM diffraction patterns. The corresponding  $d$  values of the diffraction spots were determined [46] by measuring the distance  $R$  from the centre in the SADP with the program Digital Micrograph Diffpack from Gatan Inc. Calibration was achieved either by calculation from the acceleration voltage  $U_B$ , the camera length  $L$  or by internal calibration using ferrite matrix spots of which the  $d$  values are known. The last method was applied in most cases. These measured  $d$  values of the diffraction spots were compared with the calculated  $d$  values (see above) to index the diffraction spots and identify the present phases.

Due to the difficult distinction of AlN and CrN rock-salt structure in the SADPs, scanning transmission electron microscopy (STEM) was applied to get information of the chemical composition of the nitride precipitates. The STEM investigation was performed using a VG HB 501UX scanning transmission electron microscope operating at 100 kV with a focused beam of less than 1 nm size and a NORAN EDX system equipped with a multi-channel analyser (10 eV per channel). Line-scans for analysis were conducted across the nitride precipitates. For each line-scan 30 points were measured with a dwell time of 5 s per point (evaluation software: NORAN System SIX).

High-resolution transmission electron microscopy (HRTEM) was used to reveal the (atomic) structure at the precipitate/matrix interfaces. To this end a JEOL ARM high voltage microscope was used operating at 1250 kV.



## 2.2.4 Determination of nitrogen absorption isotherm

For quantitative analysis of excess nitrogen uptake a nitrogen absorption isotherm was determined (cf. Ref. [47] for background of nitrogen absorption measurement). For this purpose rectangular foils ( $20 \times 15 \times 0.2 \text{ mm}^3$ ) were prepared. To determine an absorption isotherm the nitriding was carried out in the same nitriding furnace as described in section 2.2.2. Pre-nitriding was performed at  $(853 \pm 1) \text{ K}$  for 24 h in a  $\text{H}_2/\text{NH}_3$  gas mixture (455 ml/min  $\text{H}_2$  and 45 ml/min  $\text{NH}_3$ ) corresponding to a nitriding potential of  $r_{\text{N}} = 0.104 \text{ atm}^{-1/2}$  (cf. section 2.2.2). It was proven experimentally that there is no further nitrogen uptake upon nitriding times longer than 24 h. After this pre-nitriding the nitrogen is distributed homogeneously over the whole cross-section, as proven by EPMA. Subsequently the pre-nitrided foil was denitrided at a (lower) temperature of  $(743 \pm 1) \text{ K}$  for 48 h in a pure hydrogen gas flow (500 ml/min) to remove nitrogen which is not strongly bonded (to the alloying elements) without changing the microstructure.

The data for the nitrogen absorption isotherm were determined by nitriding the foil at  $(833 \pm 1) \text{ K}$  for 30 h applying four different nitriding potentials:  $r_{\text{N}} = 0.054 \text{ atm}^{-1/2}$  (i.e. 475 ml/min  $\text{H}_2$  and 25 ml/min  $\text{NH}_3$ ),  $r_{\text{N}} = 0.091 \text{ atm}^{-1/2}$  (i.e. 460 ml/min  $\text{H}_2$  and 40 ml/min  $\text{NH}_3$ ),  $r_{\text{N}} = 0.117 \text{ atm}^{-1/2}$  (i.e. 450 ml/min  $\text{H}_2$  and 50 ml/min  $\text{NH}_3$ ) and  $r_{\text{N}} = 0.140 \text{ atm}^{-1/2}$  (i.e. 442 ml/min  $\text{H}_2$  and 58 ml/min  $\text{NH}_3$ ). After each nitriding step a denitriding step was performed in the same way as described above. The change of the nitrogen content after each nitriding and after each denitriding was measured by weighing the foil on a Mettler microbalance with an accuracy of 1  $\mu\text{g}$ . For each nitriding/denitriding state, twenty weightings were carried out to determine an average mass value. The standard error of the mean was calculated for each data point. The obtained errors in the mass differences upon nitriding/denitriding are smaller than the size of the data points in the absorption isotherm (see section 2.3.5).

## 2.3 Results and evaluation

### 2.3.1 Phase analysis

X-ray diffraction analyses were carried out on the specimen surface before and after nitriding. After nitriding no new phase(es) is/are detectable in the diffractograms recorded from the specimen surface (cf. Fig. 2.1), but the peaks of the ferrite matrix had very strongly broadened.

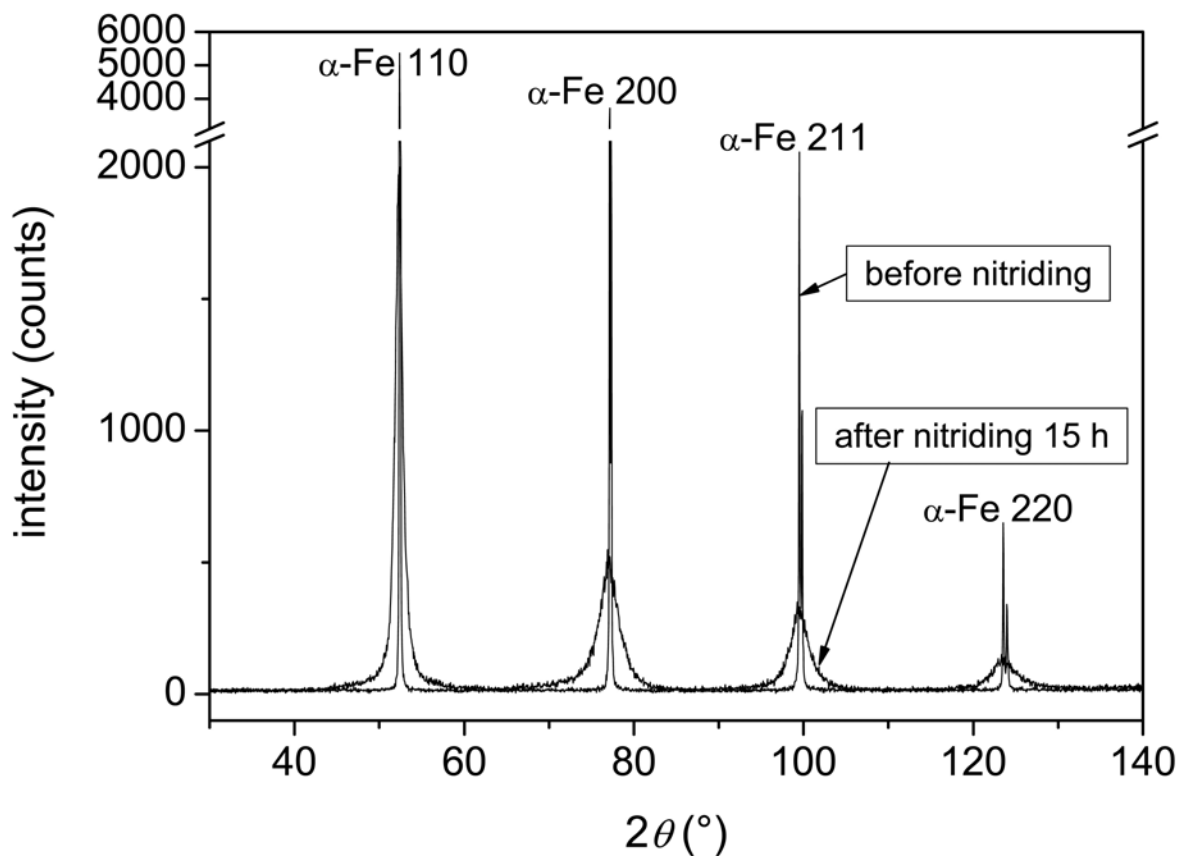


Fig. 2.1: X-ray diffractograms recorded from the surface of the specimen before and after nitriding (15 h at 853 K): A considerable peak broadening of the ferrite peaks is observed after nitriding.

### 2.3.2 Crack formation

During the nitriding process cracks appear in the nitrified microstructure. A LM micrograph of the nitrified surface is shown in Fig. 2.2 a (top view). Grain boundaries, pores (due to single grains, which have apparently broken out) and cracks along grain boundaries are visible. The etched cross-section of a nitrified specimen is shown in Figs. 2.2 b and c. Cracks and holes of lacking grains (see white arrows in Fig. 2.2 c)

are visible: cracks mostly start at the nitrated surface and propagate more or less perpendicular to the surface along grain boundaries across the nitrated layer in the direction of the unnitrided core. Such cracks are distributed over the whole cross-section. The lacking grains in the cross-section had probably broken out during grinding and polishing, whereas the lacking grains at the surface had broken out during nitriding.

### **2.3.3 Composition and microhardness depth profiles**

The EPMA concentration depth profiles of N and the two nitride forming elements Al and Cr are shown in Fig. 2.2 b (the results of five single line-scans, taken from different sites on the cross-section perpendicular to the surface, are shown together, superposed graphically in one concentration depth profile). Except at the surface, where the atomic concentration of Al and Cr is slightly decreased, as a consequence of a distinct near surface increase of the N concentration, the Al and Cr concentrations are approximately constant over the cross-section. At some sites in the EPMA line-scans the electron beam hits single pores. These pores cause a seeming increase of the concentrations of light elements as Al and N, because the physical assumptions used in the quantitative evaluation of the element concentrations (absorption and atomic number correction) are not fulfilled near pores [44]. The N concentration depth profile (Fig. 2.2 b) is characterised by: (i) a strong decrease of N content towards larger depth near the surface, (ii) a subsequent plateau region of N content with a modest negative slope and (iii) the transition zone between nitrated layer and unnitrided core where the N concentration drops to zero.

Immediately after EPMA the embedded cross-section was etched to uncover the line-scans of the electron beam (revealed by the carbon deposition, cf. LM micrograph shown in Fig. 2.2 c). Along two (of the five) EPMA line-scans (one started from the left surface, another one started from the opposite, right surface of the specimen cross-section; cf. LM micrograph in Fig. 2.2 c), the microhardness values were determined. The obtained N concentration depth profile can be compared with the corresponding microhardness depth profile in Fig. 2.2 c. The microhardness distribution over the cross-section shows the same characteristics as the N concentration depth profile.

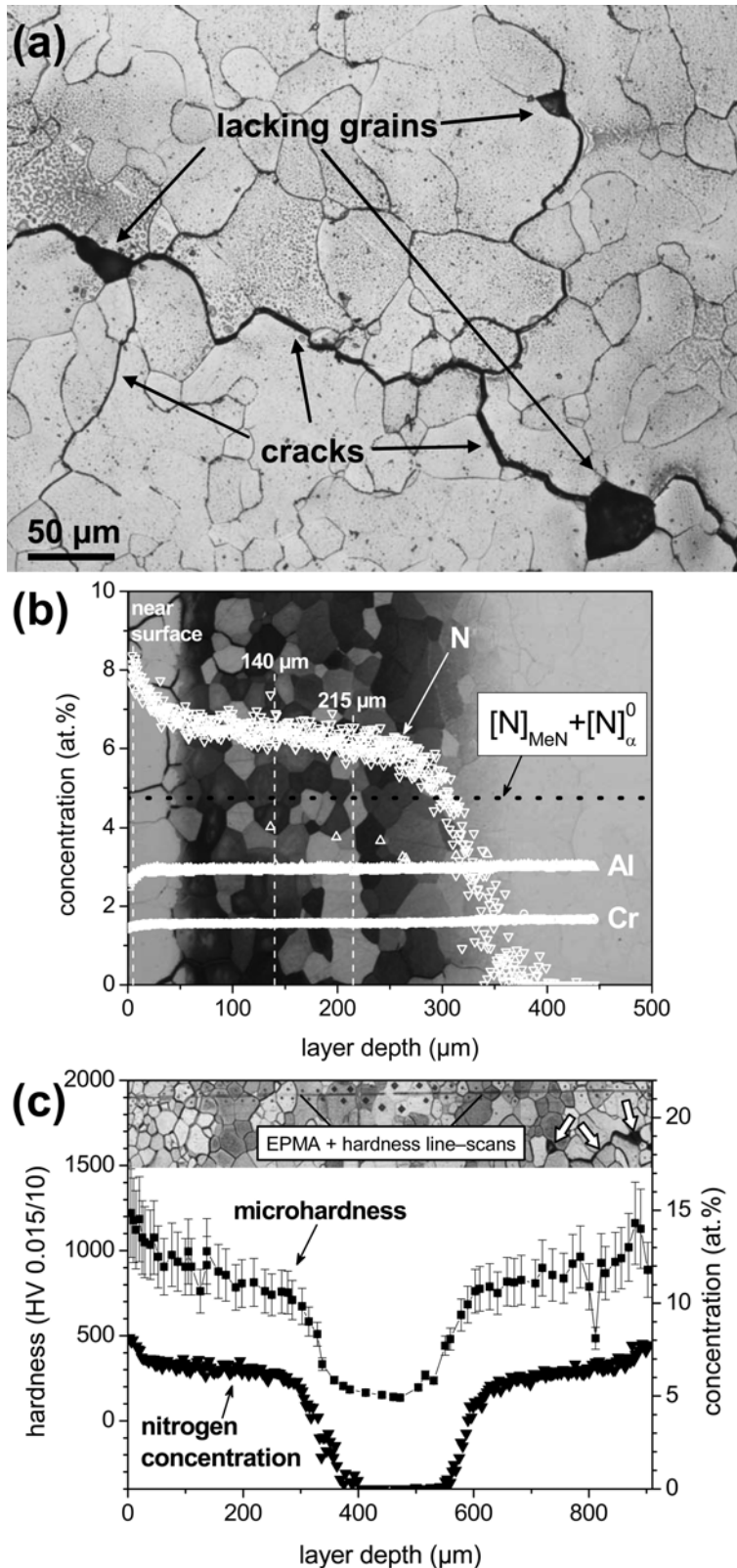


Fig. 2.2: (a) LM micrograph of the specimen surface after nitriding (15 h at 853 K). The surface was not etched! Cracks along grain boundaries and lacking grains are visible for this condition. (b) N, Al and Cr (EPMA) concentration depth profiles of a nitrided specimen (15 h at 853 K) combined with the corresponding LM micrograph. The dashed vertical white lines denote the depth values from which TEM samples were prepared. The dotted horizontal black line denotes the amount of N, which is necessary to transform all alloying elements into alloying element nitrides plus the amount of nitrogen dissolved interstitially in the unstrained remaining ferrite matrix. (c) Microhardness and N concentration depth profiles after nitriding; the corresponding LM micrograph is also shown in Fig. 2.2 c.

The dotted horizontal line in Fig. 2.2 b denotes the so-called *normal* amount of N,  $[N]_{\text{normal}} = 4.74$  at.%, which is necessary to transform all substitutionally dissolved Al and Cr into nitride precipitates (i.e.  $[N]_{\text{MeN}}$ ) plus the amount of N, which can be dissolved interstitially in the remaining pure, unstrained ferrite matrix in the thermodynamic equilibrium at the applied nitriding conditions (i.e.  $[N]_{\alpha\text{-Fe}}^0$ ). The value  $[N]_{\alpha\text{-Fe}}^0 = 0.30$  at.% was experimentally determined under similar conditions as applied to the nitriding of the ternary Fe–Cr–Al alloy, by nitriding a pure ferrite foil [47]. The amount of N in excess of this normal amount of N is called “*excess nitrogen*” [15, 36, 48] (cf. section 2.3.5). Evidently (see Fig. 2.2 b), during nitriding the specimens take up much more N than necessary for the stoichiometric formation of the nitride precipitates and realisation of the equilibrium N solubility in the ferrite matrix.

### 2.3.4 Transmission electron microscopy analysis (TEM)

TEM analysis was carried out to identify the precipitated nitride phase(s). The dashed vertical white lines in the cross-section shown in Fig. 2.2 b indicate the depths at which TEM samples were prepared.

#### 2.3.4.1 Crystallography of nitride precipitates and deformation structure

The SADPs (zone axis:  $[001]_{\alpha\text{-Fe}}$ ) of the *nitrided surface* region (15 h at 853 K), corresponding to the DF images presented in Figs. 2.3 a and b, show, besides the bright ferrite matrix spots, streaks with accumulations in intensity. Interpreting these intensity accumulations as nitride diffraction spots, they are compatible with the occurrence of reflections due to nitride precipitates of the rock-salt structure type of both CrN and AlN. The locations of the accumulations indicate that the Bain-type OR [9] holds for the nitride precipitates and the ferrite matrix:

$$\{001\}_{\alpha\text{-Fe}} // \{001\}_{\text{MeN}}, \langle 100 \rangle_{\alpha\text{-Fe}} // \langle 110 \rangle_{\text{MeN}}; \text{Me} = \text{Cr}, \text{Al}$$

There are three variants of the Bain OR between ferrite and cubic, rock-salt structure type precipitates (cf. Table 2.2 and Figs. 2.3 c to e). The superposition of these three variants leads to the characteristic SADP shown in Fig. 2.3 f. On the experimental SADPs shown in Figs. 2.3 a and b discrete spots are visible at locations of the

forbidden  $\{100\}_{\alpha\text{-Fe}}$  reflections, which are due to  $\{220\}_{\text{Fe}_3\text{O}_4}$  reflections from  $\text{Fe}_3\text{O}_4$ , which unavoidably developed at the surface of the foil for TEM analysis [5, 17, 49].

Table 2.2

The three variants of the Bain orientation relationship between ferrite and cubic, rock-salt structure type precipitates (cf. Figs. 2.3 c to e).

Bain orientation relationship		
variant 1	variant 2	variant 3
$[100]_{\alpha\text{-Fe}} // [1\bar{1}0]_{\text{MeN}}$	$[100]_{\alpha\text{-Fe}} // [001]_{\text{MeN}}$	$[100]_{\alpha\text{-Fe}} // [110]_{\text{MeN}}$
$[010]_{\alpha\text{-Fe}} // [110]_{\text{MeN}}$	$[010]_{\alpha\text{-Fe}} // [1\bar{1}0]_{\text{MeN}}$	$[010]_{\alpha\text{-Fe}} // [001]_{\text{MeN}}$
$[001]_{\alpha\text{-Fe}} // [001]_{\text{MeN}}$	$[001]_{\alpha\text{-Fe}} // [110]_{\text{MeN}}$	$[001]_{\alpha\text{-Fe}} // [1\bar{1}0]_{\text{MeN}}$

Tiny platelet-like structures are visible in the DF images, taken from the rock salt  $002_{\text{MeN}}$  spots of two different variants of the Bain OR (cf. circles in SADP), pertaining to nitride precipitates, which are oriented perpendicular with respect to each other (cf. Figs. 2.3 a and b). The length of the precipitate platelets can be estimated from the DF images in Figs. 2.3 a and b and is about 10 nm (and smaller).

A DF image, obtained using a  $002_{\text{MeN}}$  spot of the rock-salt structure type nitride precipitate, and the corresponding SADP from a *nitrided depth of about 140  $\mu\text{m}$*  are shown in Fig. 2.4 a. Platelet-like structures are visible, which obey the Bain OR. The length of the precipitates (lateral size of the platelets) at this depth is in the range of about 100 nm and hence 10 times larger than near the surface in the same specimen (cf. Figs. 2.3 a and b).

A BF image and the corresponding SADP from a *nitrided depth of about 215  $\mu\text{m}$*  are shown in Fig. 2.4 b. The incident electron beam is not exactly parallel to the  $[001]_{\alpha\text{-Fe}}$  zone axis. Platelets, oriented more or less perpendicularly with respect to each other, can be seen in the BF image; the platelets are surrounded by strain-field contrast. The size of the precipitates at this depth of 215  $\mu\text{m}$  is in the same range as at a depth of 140  $\mu\text{m}$  (cf. Figs. 2.4 a and b). Apparently the precipitate platelets in Fig. 2.4 b are distorted (bent) and the Bain OR is only approximately satisfied: the precipitates are not oriented exactly perpendicularly with respect to each other. Further a variation in the brightness along a platelet in the DF image occurs (cf. Fig. 2.5 a), which is associated with a splitting up of the  $\{002\}_{\text{MeN}}$  diffraction spots (cf.

Fig. 2.5 b); both observations are compatible with bending and local distortion of the platelets.

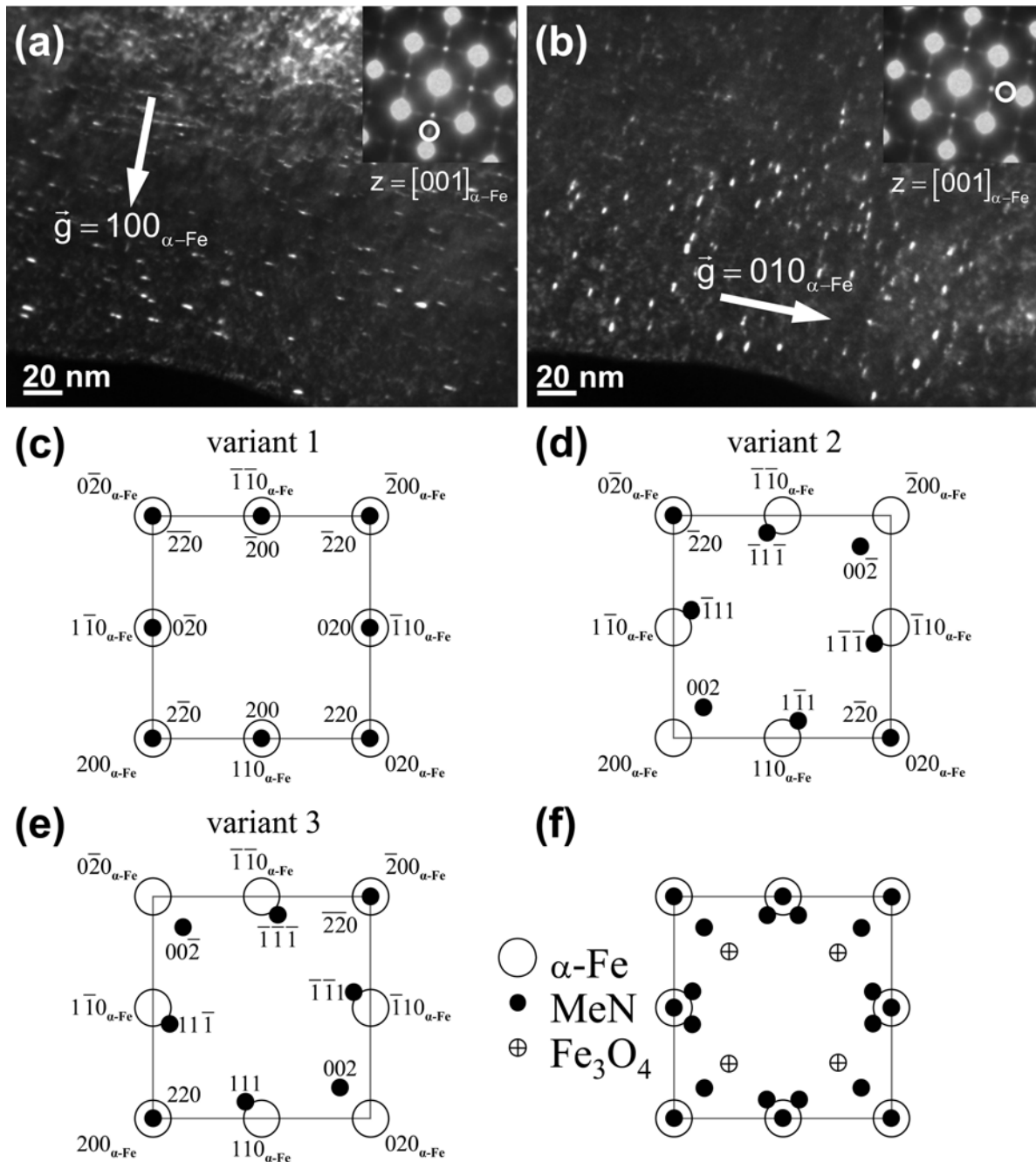


Fig. 2.3: (a) and (b) DF images and corresponding SADPs of an ion milled TEM sample from near the nitrided surface (few  $\mu\text{m}$  depth); the DF images are obtained from  $002_{\text{MeN}}$  spots of the rock-salt structure type of the nitride precipitates in a Bain OR with the ferritic matrix (see Figs. 2.3 d and e). (c) to (e) Schematic SADPs (zone axis:  $[001]_{\alpha-Fe}$ ) of the three variants 1, 2 and 3 of the Bain OR between the ferritic matrix and cubic, rock-salt structure type nitride precipitates, and their superposition in (f). Transparent circles:  $\alpha-Fe$  spots. Black circles: cubic, rock-salt structure type spots. Crossed circles:  $220_{\text{Fe}_3\text{O}_4}$  spots.

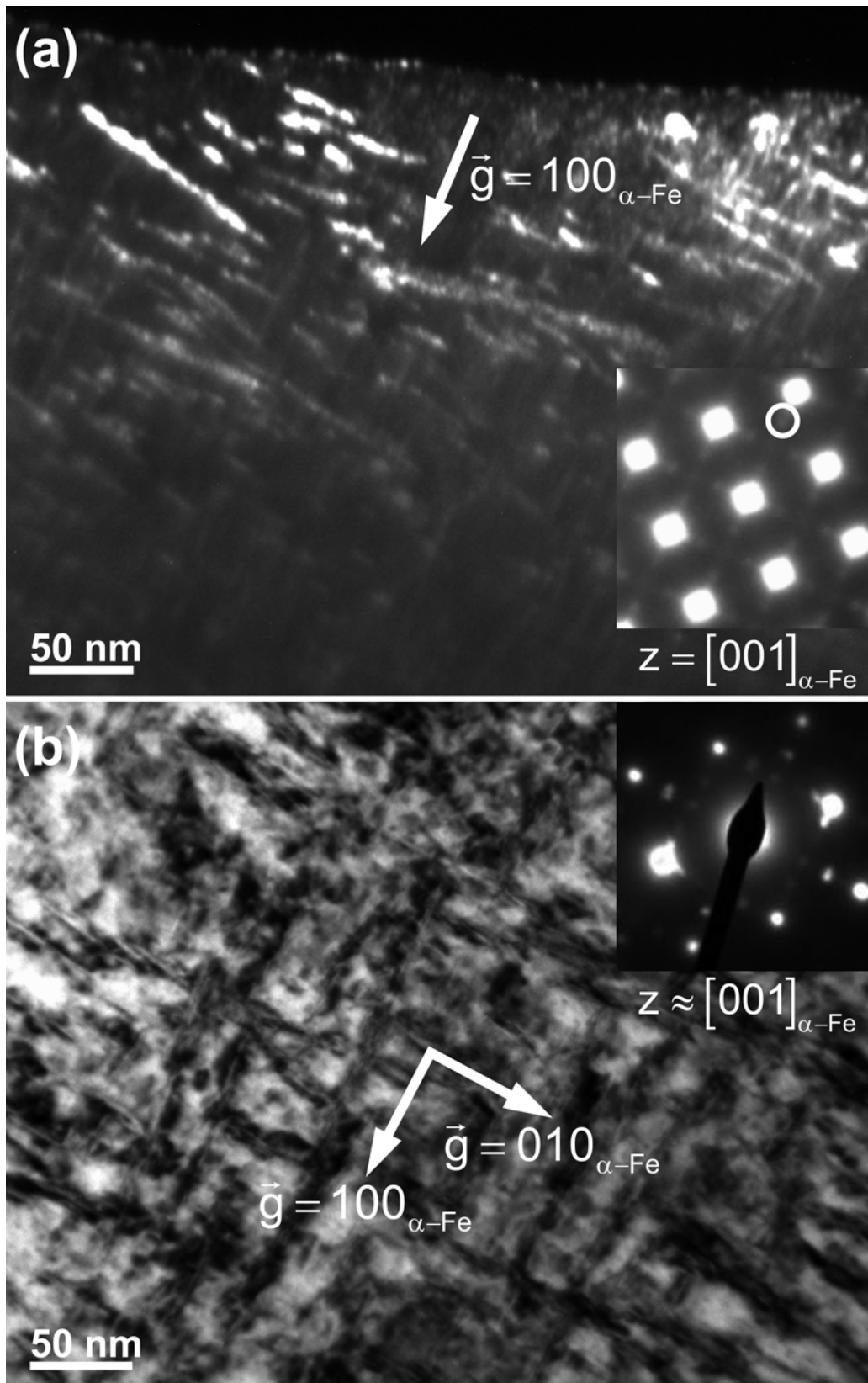


Fig. 2.4: (a) DF image obtained from a  $002_{\text{MeN}}$  spot of the rock-salt structure nitride precipitate and corresponding SADP (electron-beam axis:  $[001]_{\alpha\text{-Fe}}$ ) of an ion-milled TEM sample from a nitrated depth of about 140  $\mu\text{m}$ ; MeN with Bain OR with the ferrite matrix (see Fig. 2.3: variant 2). (b) BF image and corresponding SADP (electron-beam axis near  $[001]_{\alpha\text{-Fe}}$ ) of an ion-milled TEM sample from a nitrated depth of about 215  $\mu\text{m}$ . Note the strain-field contrast around the precipitates.



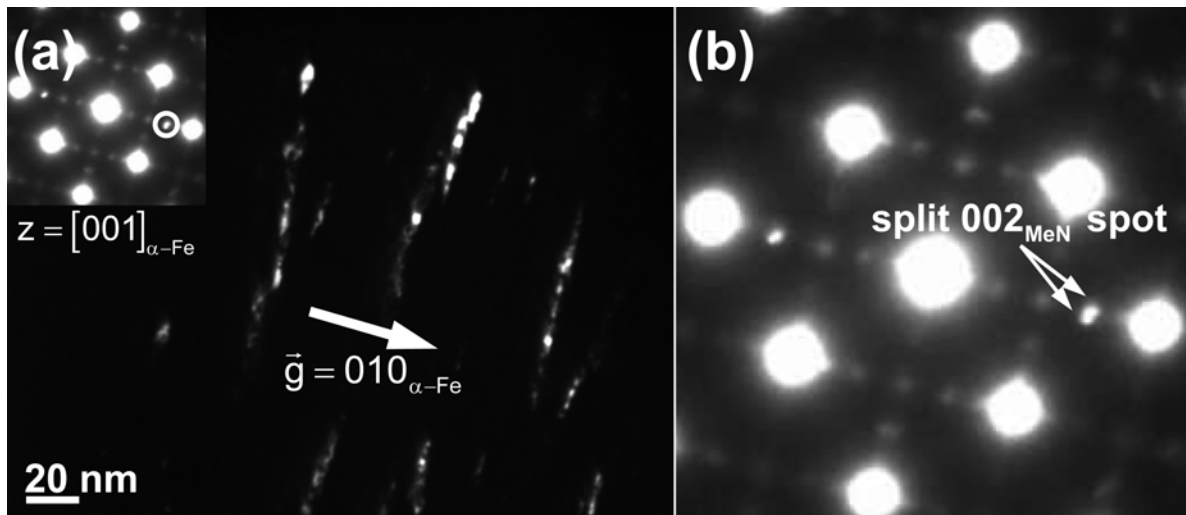


Fig. 2.5: (a) DF image obtained from a  $002_{MeN}$  spot of the rock-salt structure nitride precipitate and corresponding SADP (electron-beam axis:  $[001]_{\alpha-Fe}$ ) of an ion-milled TEM sample from a nitrified depth of about  $215 \mu\text{m}$ . Along each platelet a variation in the brightness occurs. (b) SADP of Fig. 2.5 a showing a split  $002_{MeN}$  spot of the rock-salt structure nitride precipitate with Bain OR with the ferrite matrix.

#### 2.3.4.2 High resolution transmission electron microscopy (HRTEM)

An HRTEM image (zone axis:  $[001]_{\alpha-Fe}$ ) of an ion-milled TEM sample taken near the *nitrified surface* and a fast Fourier transformation (FFT) pattern from a selected region of the image (see white square) are shown in Fig. 2.6 a. In the white-squared area two tiny platelet-like precipitates are visible, which are oriented perpendicularly with respect to each other (cf. arrows). The FFT pattern is congruent with variants 2 and 3 of the Bain OR (cf. Table 2.2 and Figs. 2.3 d and e), including the oxide spots.

The inverse FFT image of the ferrite matrix, containing a tiny precipitate (thickness about 1 nm) obeying the Bain OR (visible in the lower right corner (see arrow) of the white-squared area in Fig. 2.6 a), obtained utilising the  $\{110\}_{\alpha-Fe}$  and  $\{200\}_{\alpha-Fe}$  ferrite spots and precipitate spots corresponding to variant 2 of the Bain OR (cf. Table 2.2 and Fig. 2.3 d), is shown in Fig 2.6 b (cf. FFT image in the upper right corner of Fig 2.6 b). The precipitate is largely coherent with the ferrite matrix. A few dislocations have been observed in the ferrite matrix surrounding a precipitate (Burgers circuit analysis).

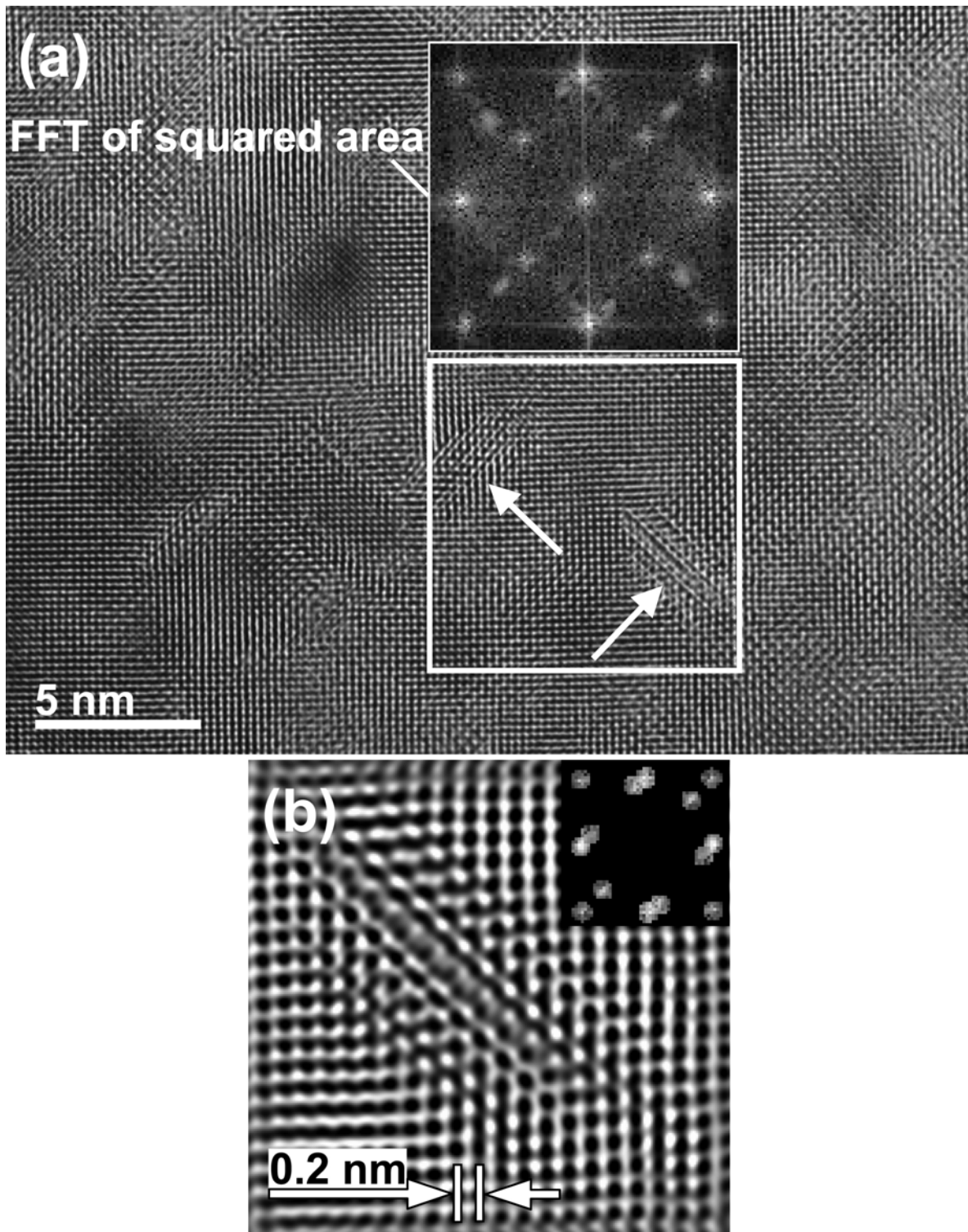


Fig. 2.6: (a) HRTEM image of an ion milled TEM sample from near the nitrated surface (electron-beam axis:  $[001]_{\alpha\text{-Fe}}$ ). The FFT pattern was generated from the area within the white square. (b) Inverse FFT filtered image of the ferrite matrix with precipitate; utilising  $110_{\alpha\text{-Fe}}$  and  $200_{\alpha\text{-Fe}}$  spots and precipitate spots corresponding to Bain OR variant 2 (cf. Table 2.2 and Fig. 2.3 d).

### 2.3.4.3 Composition of the nitride precipitates

A STEM BF image of a precipitate taken at a *nitrided depth of about 215  $\mu\text{m}$*  is shown in Fig. 2.7 a. Although the quality of the BF images is poor, due to an uncorrectable astigmatism caused by the ferromagnetism of the TEM samples, a platelet-like precipitate, appearing bright against its dark surroundings, is visible in Fig. 2.7 a. The arrow in the BF image depicts the path of the energy-dispersive X-ray spectroscopy (EDX) line-scan. The Cliff–Lorimer ratio technique [50] was applied for quantitative analysis of Fe, Cr and Al, considering the X-ray absorption and assuming a maximum TEM foil thickness of 200 nm. Due to the drift of the sample, the counting time was limited and reliable results for the N concentration could not be obtained, for which reason N was not taken into account for the quantitative analysis. The results for Cr and Al have been plotted as concentration in at.% versus the distance along the depicted path and are shown in Fig. 2.7 b. Evidently, in the precipitate both alloying elements Cr and Al are present. Although the atomic fractions shown in Fig. 2.7 b can only be considered relatively (as N was not taken into account; see above), the measurements do indicate that a higher atomic fraction of Al than Cr is contained in the nitride, which is compatible with the composition of the alloy, assuming that all Cr and all Al has precipitated as mixed nitride.

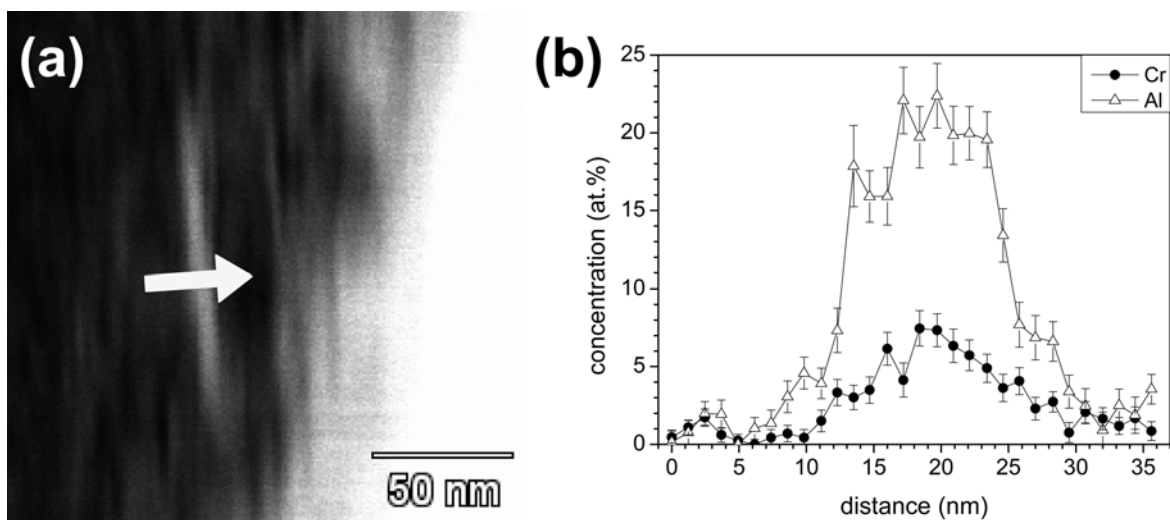


Fig. 2.7: (a) STEM BF image of a precipitate in an ion-milled sample from a nitrided depth of about 215  $\mu\text{m}$  (specimen nitrided for 15 h at 853 K). The image is strongly astigmatic because of the ferromagnetism of the sample. (b) Results of the EDX line-scan (indicated by arrow in Fig. 2.7 a). Both alloying elements Al and Cr are present in the precipitate. The atomic fraction values can only be applied relatively (see section 2.3.4.3).

#### 2.3.4.4 Jet-electropolished TEM samples

A BF image and the corresponding SADP of a jet-electropolished TEM sample from a nitrided depth of about  $215\ \mu\text{m}$  are shown in Fig. 2.8. The SADP not only shows discrete spots of the ferrite matrix and the rock-salt structure type nitride precipitates but also diffraction rings of the rock-salt structure type nitride reflections occur, which is compatible with the presence of very fine, not specifically oriented precipitates. Such diffraction rings were never observed in this work in SADPs of ion-milled samples. Ring patterns in SADPs were also observed by other authors [5, 37] examining jet-electropolished foils of nitrided Fe–Al alloys. The presence of such diffraction rings appear to be an effect of the jet-electropolishing preparation method: apparently part of the ferrite matrix dissolves preferentially during jet-electropolishing and the remaining tiny nitride crystals are no longer constrained by a surrounding matrix leading to a random orientation distribution.

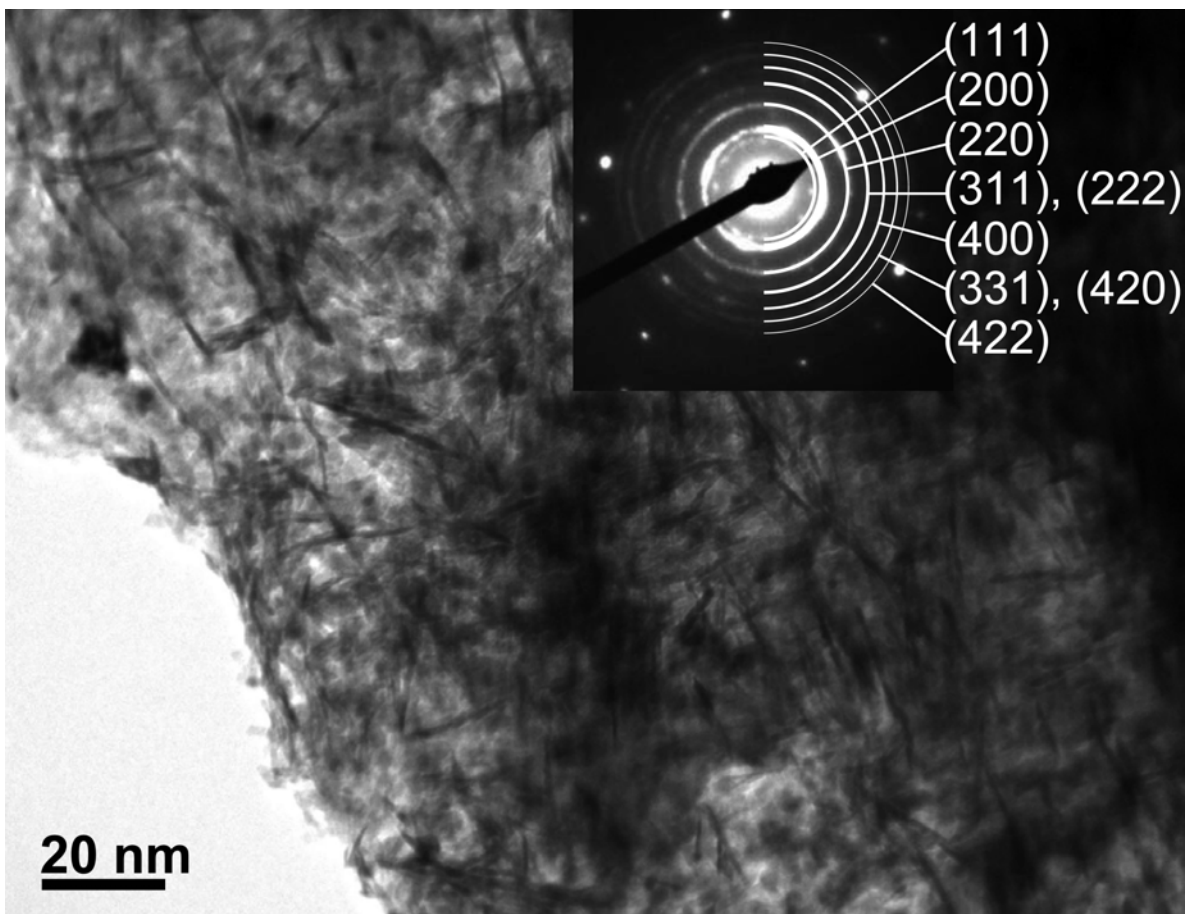


Fig. 2.8: BF image and SADP of a jet-electropolished TEM sample from a nitrided depth of about  $215\ \mu\text{m}$  (specimen nitrided for 15 h at 853 K). The rings in the SADP have been indexed according to the MeN rock-salt structure type (Me = Cr, Al). The platelet-like precipitates appear oriented randomly.

### 2.3.5 Analysis of excess nitrogen uptake

The nitrogen concentration  $[N]_{\text{total}}$  in the Fe–1.5wt.%Cr–1.5wt.%Al foil (i.e. Fe–1.58at.%Cr–3.07at.%Al) upon mass increase after homogeneous pre-nitriding (cf. section 2.2.4) was  $(5.911 \pm 0.004)$  at.%. The normal N uptake  $[N]_{\text{normal}} = [N]_{(\text{Cr, Al})\text{N}} + [N]_{\alpha\text{-Fe}}^0$  after pre-nitriding, where  $[N]_{(\text{Cr, Al})\text{N}}$  is the amount of N incorporated in the nitride precipitate and  $[N]_{\alpha\text{-Fe}}^0$  is the equilibrium solubility of N in the unstrained ferrite matrix corresponding to the applied temperature and nitriding potential<sup>3</sup>, can be calculated as  $(4.650 \pm 0.004)$  at.%, assuming that all Al and Cr has formed nitride precipitates (either AlN and CrN or (Al, Cr)N). Hence the total amount of excess nitrogen follows from  $[N]_{\text{total}}^{\text{excess}} = [N]_{\text{total}} - [N]_{\text{normal}}$ .  $[N]_{\text{total}}^{\text{excess}}$  has two parts: (i) mobile excess nitrogen, i.e. extra dissolved N due to the tensile hydrostatic component of misfit stress in the ferrite matrix [36],  $[N]_{\text{strain}}$  and (ii) immobile excess nitrogen. Immobile excess nitrogen consists of two components: N segregated at dislocations  $[N]_{\text{dislocations}}$ , and N adsorbed at the platelet faces  $[N]_{\text{interface}}$ . Due to the low dislocation density in recrystallised foils,  $[N]_{\text{dislocations}}$  can be neglected and thus  $[N]_{\text{strain}} + [N]_{\text{interface}} = (1.261 \pm 0.004)$  at.%.

After pre-nitriding, the foil was denitrided (cf. section 2.2.4). The remaining amount of N after denitriding, determined by weight measurement, was  $(4.527 \pm 0.001)$  at.%. The amount of N, which is necessary to transform all Cr and Al into nitride precipitates (i.e.  $[N]_{(\text{Cr, Al})\text{N}} = [\text{Cr}]_{\text{Cr}_{1-x}\text{Al}_x\text{N}} + [\text{Al}]_{\text{Cr}_{1-x}\text{Al}_x\text{N}}$ ) is  $(4.445 \pm 0.001)$  at.% and hence only 0.082 at.% lower than the experimentally remaining N concentration after denitriding. It is concluded that the N remaining after denitriding is the N strongly bonded in and at the MeN precipitates (see section 2.4.5).

---

<sup>3</sup> The equilibrium solubility of N in ferrite  $[N]_{\alpha\text{-Fe}}^0$  at 853 K for the nitriding potential of  $r_N = 0.104 \text{ atm}^{-1/2}$  was determined by nitriding a pure ferrite foil [47]: 0.30 at.% (cf. section 2.3.3).

The results of the pre-nitriding and denitriding experiments are summarised in Fig. 2.9 a, where the N content is expressed as the number of N atoms taken up per 100 (Fe + Cr + Al) matrix atoms.

In order to identify the contributions of mobile and/or immobile excess nitrogen in the total amount of excess nitrogen, a nitrogen absorption isotherm at 833 K was determined (cf. Fig. 2.9 b) for the Fe–1.5wt.%Cr–1.5wt.%Al foil after pre-nitriding (at 853 K) and denitriding (at 743 K). The above discussed N level after denitriding has been indicated by “A”. The expected amount of N required for the formation of the  $\text{Cr}_{1-x}\text{Al}_x\text{N}$  precipitates (i.e.  $[\text{N}]_{(\text{Cr, Al})\text{N}}$ ) has been indicated by “C”. At constant temperature the amount of interstitially dissolved N in the ferrite matrix increases linearly with  $r_{\text{N}}$  [4, 42]. Thus the straight line dependence above level “B” in Fig. 2.9 b represents N dissolved interstitially in the ferrite matrix. Fitting of a straight line to all four square data points leads to the dashed line in Fig. 2.9 b, which intersects the ordinate at  $r_{\text{N}} = 0$ ; the point of intersection has been indicated by “B”.

The difference between level “B” and level “C” corresponds with N taken up in excess of the amount needed to form the  $\text{Cr}_{1-x}\text{Al}_x\text{N}$  precipitates. In accordance with the earlier analyses of nitrogen absorption isotherms recorded for Fe–1wt.%Cr (i.e. Fe–1.04at.%Cr) [51] and Fe–2wt.%V (i.e. Fe–2.23at.%V) [47], such N is conceived as adsorbed at the faces of the tiny, (semi)coherent nitride platelets. The amount of this nitrogen is indicated by  $[\text{N}]_{\text{interface}}$ .

The equilibrium solubility of N in pure, unstrained ferrite  $[\text{N}]_{\alpha\text{-Fe}}^0$  at temperatures in the range of 773 K to 843 K has been determined as a function of nitriding potential in Refs. [47] and [52]. On this basis the equilibrium solubilities of N in ferrite at 833 K for the different nitriding potentials used in this work have been given in Table 2.3 and in Fig. 2.9 b.

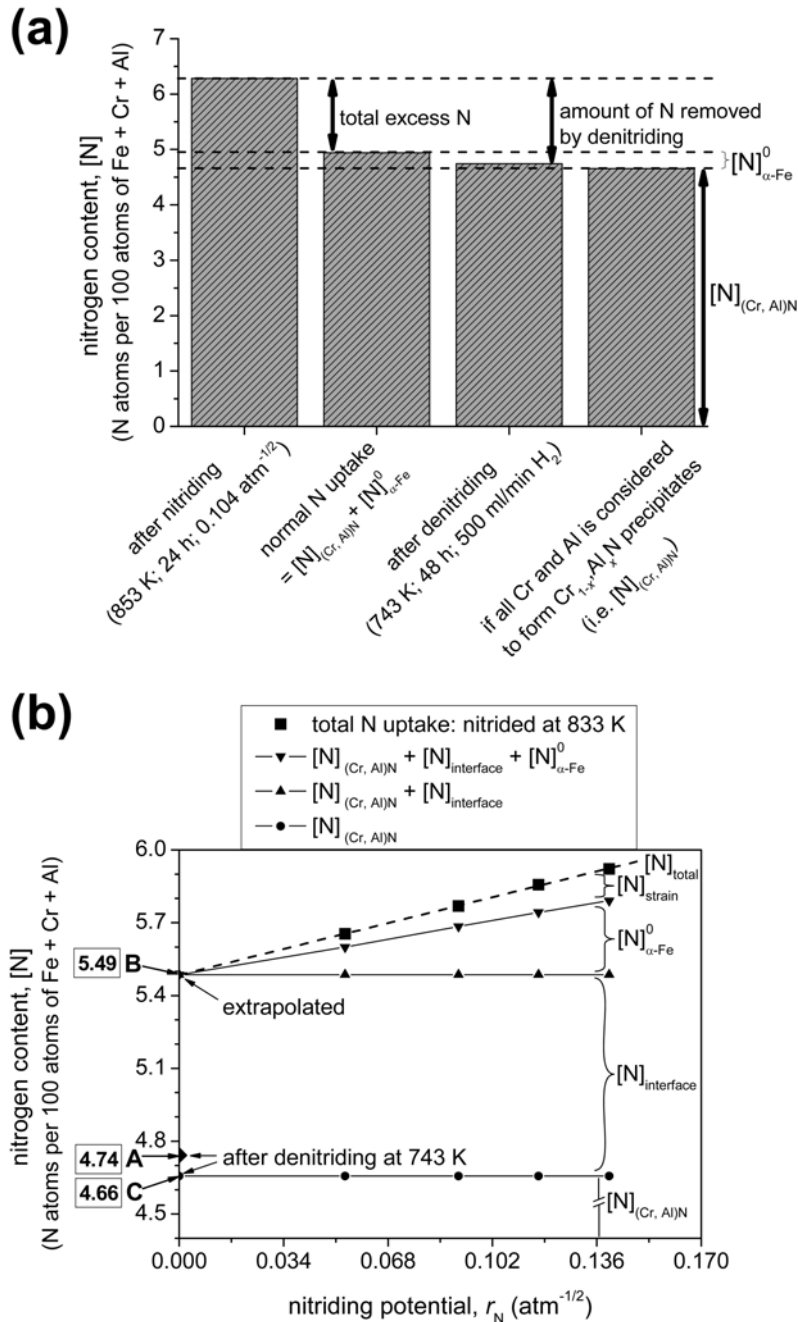


Fig. 2.9: (a) Summary of the pre-nitriding (24 h at 853 K,  $r_N = 0.104 \text{ atm}^{-1/2}$ ) and denitriding (48 h at 743 K in pure H<sub>2</sub>) experiments performed with a Fe–1.5wt.%Cr–1.5wt.%Al (i.e. Fe–1.58at.%Cr–3.07at.%Al) foil. The N content is related to 100 (Fe + Cr + Al) matrix atoms.  $[N]_{(Cr, Al)N}$  is the amount of N required for the precipitation of all Al and Cr as

$Cr_{1-x}Al_xN$ , and  $[N]_{\alpha-Fe}^0$  is the amount of N dissolved in an unstrained pure ferrite matrix at the pre-nitriding conditions. (b) Nitrogen absorption isotherm of the pre- and denitrided Fe–1.5wt.%Cr–1.5wt.%Al foil determined at 833 K for different nitriding potentials (N content related to 100 atoms of Fe + Cr + Al). The N level after denitriding has been indicated by “A”. The calculated N level  $[N]_{(Cr, Al)N}$  has been indicated by “C”. The linear portion of the absorption isotherm has been indicated by the dashed line which intersects the ordinate at  $r_N = 0$  at a N level indicated by “B”.  $[N]_{interface}$ ,  $[N]_{\alpha-Fe}^0$  and  $[N]_{strain}$  denote N adsorbed at the precipitate/matrix interface, N dissolved in unstrained ferrite and excess nitrogen dissolved in the ferrite matrix due to the precipitate-matrix misfit strain, respectively.

Table 2.3

Total N uptake in a pre-nitrided (at 853 K) and denitrided (at 743 K) Fe-1.5wt.%Cr-1.5wt.%Al foil (i.e. Fe-1.58at.%Cr-3.07at.%Al) nitrided at 833 K at different nitriding potentials. Values for N uptake in unstrained pure ferrite (i.e.  $[N]_{\alpha\text{-Fe}}^0$ ) at 833 K for the applied nitriding potentials were calculated using data in Refs. [47] and [52].

$r_N$ (atm- $^{1/2}$ )	$[N]^{\text{total}}$ (at.%)	$[N]^{\text{total}}$ (N at. / 100 at. Fe + Cr + Al)	$[N]_{\alpha\text{-Fe}}^0$ at 833 K (at.%)
0	5.20*	5.49*	0
0.054	5.351 $\pm$ 0.008	5.654 $\pm$ 0.009	0.12
0.091	5.454 $\pm$ 0.002	5.769 $\pm$ 0.003	0.21
0.117	5.533 $\pm$ 0.001	5.857 $\pm$ 0.002	0.27
0.140	5.590 $\pm$ 0.001	5.921 $\pm$ 0.002	0.32

\*Estimate: extrapolation of the straight line fitted through the data points to  $r_N = 0$  yields the N level "B" = 5.49 N atoms per 100 atoms of Fe + Cr + Al in Fig. 2.9 b

The subdivision of the total N uptake  $[N]_{\text{total}}$  in  $[N]_{(\text{Cr, Al})\text{N}}$ ,  $[N]_{\text{interface}}$ ,  $[N]_{\alpha\text{-Fe}}^0$  and  $[N]_{\text{strain}}$  at the different nitriding potentials has thus been indicated in Fig. 2.9 b. The number of N atoms per 100 atoms of Fe + Cr + Al incorporated in nitrides (i.e.  $[N]_{(\text{Cr, Al})\text{N}}$ ) and adsorbed at the nitride/matrix interface (i.e.  $[N]_{\text{interface}}$ ) are obviously independent of the nitriding potential.

The composition of a  $\text{Cr}_{1-x}\text{Al}_x\text{N}$  precipitate with adsorbed excess nitrogen  $[N]_{\text{interface}}$  can be described as  $\text{Cr}_{1-x}\text{Al}_x\text{N}_y$ , where

$$y = \frac{[N]_{(\text{Cr, Al})\text{N}} + [N]_{\text{interface}}}{[N]_{(\text{Cr, Al})\text{N}}} = \frac{\text{Level B}}{\text{Level C}} = 1.178 \quad (2.1)$$

Assuming that all Al and Cr has formed cubic  $\text{Cr}_{1-x}\text{Al}_x\text{N}_y$  platelets, the value  $y$  (cf. equation (2.1)) provides indirect information about the average thickness of a precipitate platelet. As shown in this work,  $\text{Cr}_{1-x}\text{Al}_x\text{N}$  precipitates develop as platelets in the cubic, rock-salt structure type obeying a Bain OR with the ferrite matrix. With  $\{001\}_{\text{Cr}_{1-x}\text{Al}_x\text{N}}$  as the habit planes (cf. Fig. 2.3), the thickness of a monolayer of  $\text{Cr}_{1-x}\text{Al}_x\text{N}$  is one half of the lattice parameter of the rock-salt structure type (i.e.  $\frac{a_{\text{Cr}_{1-x}\text{Al}_x\text{N}}}{2}$ ). If at every octahedral interstice in the ferrite matrix at the nitride/matrix interface one excess nitrogen atom is trapped, it follows



$$y = \frac{n+2}{n} \quad (2.2)$$

where  $n$  is the number of  $\text{Cr}_{1-x}\text{Al}_x\text{N}$  monolayers. Hence the thickness  $t$  of a  $\text{Cr}_{1-x}\text{Al}_x\text{N}$  platelet follows from

$$t = n \cdot \frac{a_{\text{Cr}_{1-x}\text{Al}_x\text{N}}}{2} = \frac{a_{\text{Cr}_{1-x}\text{Al}_x\text{N}}}{y-1}. \quad (2.3)$$

With  $a_{\text{Cr}_{1-x}\text{Al}_x\text{N}} \approx 0.411$  nm [53] the estimated average thickness  $t$  of a precipitate in the nitrided (at 853 K) foil is 2.3 nm.

## 2.4 General discussion

### 2.4.1 Combined precipitation of Al and Cr in mixed nitride precipitates

The equilibrium nitride precipitates developing in Fe–Cr and Fe–Al alloys are cubic, rock-salt structure type CrN [6, 11, 15-21] and hexagonal, wurtzite structure type AlN [5, 22-28]. The results obtained in this work show unambiguously that nitride precipitates developing in Fe–Cr–Al alloys are of mixed type: cubic, rock-salt structure type  $\text{Cr}_{1-x}\text{Al}_x\text{N}$  precipitates (see sections 2.3.4.1, 2.3.4.2 and 2.3.4.3). This finding can be interpreted as a metastable, intermediate stage of nitride precipitation in this system: indeed annealing of the nitrided system at elevated temperatures caused replacement of the mixed, cubic, rock-salt structure type  $\text{Cr}_{1-x}\text{Al}_x\text{N}$  precipitates by the equilibrium cubic, rock-salt structure type CrN and equilibrium hexagonal, wurtzite structure type AlN, involving a separation of the alloying elements (cf. chapter 3).

At the nitriding temperature, diffusion of the alloying elements Cr and Al is that slow relatively<sup>4</sup> that the Al atoms are “dragged” into the developing cubic, rock-salt structure type CrN precipitates: there is no time to diffuse away and form hexagonal, wurtzite structure type AlN precipitates (which, anyway, is a slow process due to the

---

<sup>4</sup> For 1 h at 853 K,  $\sqrt{Dt}$  (with  $D$  = diffusion coefficient of Me in ferrite and  $t$  = diffusion (i.e. nitriding) time) equals 19 nm for Cr and 13 nm for Al using diffusion data from Refs. [54, 55], whereas  $\sqrt{Dt}$  for nitrogen in pure ferrite equals  $2 \cdot 10^5$  nm using diffusion data from Ref. [56].

relatively large amount of misfit energy to be accommodated [26]). In other words: the system accepts the gain of a smaller than maximal amount of energy, released by nitride precipitation, as an intermediate solution: development of mixed, cubic, rock-salt structure type  $\text{Cr}_{1-x}\text{Al}_x\text{N}$  precipitates. The presence of Cr assures that substantial energy is set free upon precipitation of this mixed nitride, whereas this would not hold for precipitation of cubic, rock-salt structure type AlN (cf. Ref. [26]). Further, the development of the mixed, cubic, rock-salt structure type  $\text{Cr}_{1-x}\text{Al}_x\text{N}$  precipitates is facilitated by almost the same values for the lattice parameters of cubic, rock-salt structure type CrN and AlN: the size of the Cr and Al atoms/ions in this structure is almost the same.

### 2.4.2 Precipitate morphology and coherency effects

The mixed  $\text{Cr}_{1-x}\text{Al}_x\text{N}$  precipitates exhibit a plate-like morphology, with the platelets following a Bain-type orientation relationship with the ferrite matrix with  $\{001\}_{\alpha\text{-Fe}}$  habit planes parallel to the platelet faces. The platelet morphology is a consequence of the strongly anisotropic nature of the misfit with the surrounding matrix: The linear misfits along and perpendicular to the  $\{001\}_{\alpha\text{-Fe}}$  habit planes are maximally about 0.02 and 0.45, respectively, as estimated from data for pure CrN and AlN (cubic, rock-salt structure type) [25, 36].

The absence of separate nitride diffraction peaks in the X-ray diffractogram is associated to the largely coherent nature of the precipitate/matrix system: The surrounding ferrite matrix is distorted tetragonally due to the misfit between the nitride platelets and the ferrite lattice. The system composed of a coherent platelet and its tetragonally distorted ferrite surroundings diffracts coherently, giving rise to strongly broadened asymmetrical ferrite reflections (see Fig. 2.1), as has recently been discussed for VN platelets in ferrite [57]. The occurrence of many, in the ferrite matrix finely distributed, tiny, coherent precipitates explains the very high hardness values observed near the surface of about 1200 HV 0.015 (cf. Fig. 2.2 c), as compared to the hardness in the unnitrided core, which is about 150 HV 0.015.

### 2.4.3 Depth gradient of precipitate size

The length of the precipitates near the surface is about 10 nm (and smaller), whereas their thickness is about 1 nm (cf. Figs. 2.3 a, b and 2.6 b). Deeper in the nitrified layer (at depths of about 140  $\mu\text{m}$  and 215  $\mu\text{m}$ ) the precipitates are coarser than near the surface: The length of the precipitates here is about 100 nm, whereas their thickness is in the range of about 5 nm to 10 nm (cf. Figs. 2.4 a and 2.5 a).

The nitrogen supersaturation is higher near the surface than in deeper regions within the nitrified zone (this is a consequence of the necessity to maintain a nitrogen flux throughout the nitrified zone during nitriding). Hence, the driving force for nitride precipitation is higher near the surface than at larger depths. Consequently a higher nitride-nucleus density can occur near the surface. This is compatible with the observation of more and finer nitride precipitates near the surface (Figs. 2.3 a and b) than at larger depths (see Figs. 2.4 and 2.5)<sup>5</sup>.

### 2.4.4 The orientation relationship

Especially if the platelet precipitates become larger and thicker (see the observations at larger depths beneath the surface; cf. section 2.4.3), the platelets become distorted, bent and appear to “break up” (cf. contrast variation along the platelets and splitting of  $002_{\text{Cr}_{1-x}\text{Al}_x\text{N}}$  diffraction spots; cf. Figs. 2.4 a and 2.5). At this stage the Bain-type orientation relationship is no longer fulfilled exactly. This observation may be related to results reported in Ref. [16] where for thin platelets of TiN and CrN in ferrite the Bain orientation relationship and for coarser precipitates the Nishiyama–Wassermann orientation relationship was observed. Indeed, a rotation of only  $9.74^\circ$  around  $[001]_{\alpha\text{-Fe}}$  suffices to convert a Bain orientation relationship into a Nishiyama–Wassermann orientation relationship [58, 59]. For the case of fcc precipitates in a bcc matrix it may generally be expected that a continuous distribution of orientation relationships,

---

<sup>5</sup> A related phenomenon has been discussed on the same basis: occurrence of a larger number of  $\alpha\text{-Fe/CrN}$  lamellar colonies of smaller lamellar spacing near the surface of nitrified Fe–Cr alloys than at larger depths [21].

deviating a few degrees, by rotation around some axis, from the Bain orientation relationship can occur, depending on the precise state of local misfit [60, 61].

### 2.4.5 Excess nitrogen

The presence of excess nitrogen is a consequence of the coherency at the precipitate/matrix interface: the elastic accommodation of the misfit induces an elastic strain field in the matrix that allows the dissolution of mobile extra nitrogen in the ferrite matrix, and at octahedral interstices in the ferrite matrix adjacent to the platelet faces nitrogen atoms, via bonding to Cr or Al in the platelet, can be adsorbed, i.e. (immobile) excess nitrogen [36]. Evidently, the coherency can be the more pronounced the smaller and thinner the platelet. Hence, the occurrence of more excess nitrogen in the near surface region (see Fig. 2.2 b and its discussion; see also Fig. 2.6) can be a straightforward consequence of the platelets being smaller and thinner in the near surface region than at larger depths (cf. section 2.4.3).

After denitriding 0.08 at.% excess nitrogen remains in the foil (cf. Fig. 2.9 b; difference of levels A and C). This remaining excess nitrogen is apparently strongly bonded at the precipitate/matrix interface and cannot be removed easily even after longer denitriding times. This behaviour is only known from nitrided Fe–Al alloys [24, 48]. Thus it may be suggested that in particular the aluminium in the  $\text{Cr}_{1-x}\text{Al}_x\text{N}$  precipitates has a strong affinity for nitrogen and that the adsorbed excess nitrogen remaining after denitriding is that adsorbed excess nitrogen that is bonded to Al in the  $\text{Cr}_{1-x}\text{Al}_x\text{N}$  platelet.

### 2.4.6 Crack formation along grain boundaries

The hardness increase of about 800 % upon nitriding (cf. section 2.4.2) is that high that the nitrided surface region becomes brittle. The brittleness of the microstructure is enhanced by the ageing experienced during nitriding, in particular in the oldest part of the nitrided zone, i.e. near the surface: ageing leads to (partial) loss of coherency, causing a decrease of the elastic misfit strains in the matrix and thereby the capacity for excess nitrogen uptake in the matrix is reduced; excess nitrogen originally dissolved in the matrix may then precipitate as  $\text{N}_2$  gas at grain boundaries, leading to voids at grain boundaries. The presence of a tensile macrostress parallel to the surface

in the surface adjacent part of the nitrated zone (cf. chapter 4) can then easily lead to crack development, especially along those grain boundaries oriented more or less perpendicularly to the surface (cf. Figs. 2.2 a and c). Grains at the surface, eventually surrounded in the solid by open grain boundaries, can then simply “fall out” (cf. section 2.3.2 and Figs. 2.2 a and c).

## 2.5 Conclusions

- Nitriding of ternary iron-based Fe–Cr–Al alloys leads to the precipitation of cubic, rock-salt crystal structure type, mixed Cr<sub>1-x</sub>Al<sub>x</sub>N precipitates. These precipitates do not represent thermodynamic equilibrium, which would involve precipitation of cubic, rock-salt structure type CrN and hexagonal, wurtzite structure type AlN. The mixed, cubic, rock-salt structure type Cr<sub>1-x</sub>Al<sub>x</sub>N precipitates develop because diffusion of Cr and Al in ferrite, as compared to diffusion of N in ferrite, is very slow and precipitation of hexagonal, wurtzite structure type AlN is a process with difficult nucleation. The precipitation of mixed cubic, rock-salt structure type Cr<sub>1-x</sub>Al<sub>x</sub>N already releases a considerable (although not maximal) amount of energy.
- The Cr<sub>1-x</sub>Al<sub>x</sub>N precipitates develop as platelets initially coherent with the ferrite matrix according to the Bain orientation relationship. At this initial stage the nitride platelets diffract coherently with the matrix and separate nitride reflections do not occur in the X-ray diffractogram.
- More and finer nitride precipitates occur near the surface than at larger depths beneath the surface, because the driving force for nitride precipitation is largest near the surface.
- For coarser nitride platelets (i.e. at larger depths; see above) the Bain orientation relationship is no longer fulfilled exactly. The precipitates “break up” (contrast variation along the platelets in transmission electron micrographs and splitting of electron diffraction spots).
- Large amounts of excess nitrogen, 1.26 at.% in excess of the “normal” uptake of 4.65 at.%, are taken up upon precipitation of the Cr<sub>1-x</sub>Al<sub>x</sub>N precipitates, as a result of the elastic accommodation of the precipitate/matrix misfit. The excess nitrogen

uptake is largest near the surface, because the finest precipitates occur there (see above) and which are subjected to (almost) full elastic accommodation of the precipitate/matrix misfit.

- The excess nitrogen remaining after denitriding is ascribed to those nitrogen atoms, which are strongly bonded at the platelet surfaces to in particular the Al atoms in the mixed nitride at the platelet surfaces.

## **Acknowledgements**

The authors wish to thank Mr. J. Köhler and Mr. P. Kress for assistance with the nitriding experiments, Mrs. S. Haug for assistance with the EPMA experiments, Mr. W.-D. Lang for TEM sample preparation, Mrs. M. Kelsch for assistance during the first stage of TEM experiments, Dr. F. Phillipp for assistance during the first stage of HRTEM experiments, Dr. W. Sigle for assistance during the STEM experiments, discussion and critical reading of the manuscript, and Dr. A. Leineweber for discussion.

## References

- [1] C. H. Knerr, T. C. Rose and J. H. Filkowski (1991). Gas nitriding. ASM Handbook: Heat Treating. J. R. Davis, G. M. Davidson, S. R. Lampman, T. B. Zorc, J. L. Daquila, A. W. Ronke, K. L. Henniger and R. C. Uhl. Metals Park, Ohio, ASM International. 4: 387-409.
- [2] E. J. Mittemeijer and J. Grosch, Eds. Proceedings of 'AWT-Tagung Nitrieren und Nitrocarburieren', Arbeitsgemeinschaft Wärmebehandlung und Werkstofftechnik e.V., Wiesbaden (1991).
- [3] D. Liedtke, U. Baudis, J. Boßlet, U. Huchel, H. Klümper-Westkamp, W. Lerche and H. J. Spies, Wärmebehandlung von Eisenwerkstoffen Nitrieren und Nitrocarburieren, Renningen, Expert Verlag (2006).
- [4] E. J. Mittemeijer and J. T. Slycke, Surf. Eng. 12 (1996) 152-162.
- [5] M. H. Biglari, C. M. Brakman and E. J. Mittemeijer, Philos. Mag. A 72 (1995) 1281-1299.
- [6] R. E. Schacherl, P. C. J. Graat and E. J. Mittemeijer, Z. Metallk. 93 (2002) 468-477.
- [7] D. H. Jack, Acta Metall. 24 (1976) 137-146.
- [8] S. S. Hosmani, R. E. Schacherl and E. J. Mittemeijer, Acta Mater. 53 (2005) 2069-2079.
- [9] E. C. Bain, Trans. AIME 70 (1924) 25-46.
- [10] R. G. Baker and J. Nutting, Iron and Steel Inst. Spec. Rep. 64 (1959) 1-22.
- [11] B. Mortimer, P. Grieveson and K. H. Jack, Scand. J. Metall. 1 (1972) 203-209.
- [12] M. Pope, P. Grieveson and K. H. Jack, Scand. J. Metall. 2 (1973) 29-34.
- [13] J. H. Driver, D. C. Unthank and K. H. Jack, Philos. Mag. 26 (1972) 1227-1231.
- [14] B. J. Lightfoot and D. H. Jack, Proceedings of the conference on heat treatment 1973 (1975) 59-65.
- [15] P. M. Hekker, H. C. F. Rozendaal and E. J. Mittemeijer, J. Mater. Sci. 20 (1985) 718-729.

- [16] N. G. Chechenin, P. M. Bronsveld, A. Chezan, C. B. Craus, D. O. Boerma, J. T. M. De Hosson and L. Niesen, *Phys. Status Solidi A-Appl. Mat.* 177 (2000) 117-125.
- [17] M. Sennour, P. H. Jouneau and C. Esnouf, *J. Mater. Sci.* 39 (2004) 4521.
- [18] R. E. Schacherl, P. Zieba and E. J. Mittemeijer, *Diffusion in Materials: Dimat 2004, Pt 1 and 2* 237-240 (2005) 1270-1274.
- [19] S. S. Hosmani, R. E. Schacherl and E. J. Mittemeijer, *Materials Science and Technology* 21 (2005) 113-124.
- [20] S. S. Hosmani, R. E. Schacherl and E. J. Mittemeijer, *Int. J. Mater. Res.* 97 (2006) 1545-1549.
- [21] N. E. Vives Diaz, R. E. Schacherl and E. J. Mittemeijer, *Int. J. Mater. Res.* 99 (2008) 150-158.
- [22] K. Bohnenkamp, *Arch. Eisenhüttenw.* 38 (1967) 433-437.
- [23] H. H. Podgurski and H. E. Knechtel, *Trans. TMS-AIME* 245 (1969) 1595-1602.
- [24] H. H. Podgurski, R. A. Oriani, F. N. Davis, J. C. M. Li and Y. T. Chou, *Trans. TMS-AIME* 245 (1969) 1603-&.
- [25] M. H. Biglari, C. M. Brakman, M. A. J. Somers, W. G. Sloof and E. J. Mittemeijer, *Z. Metallk.* 84 (1993) 124-131.
- [26] M. H. Biglari, C. M. Brakman, E. J. Mittemeijer and S. van der Zwaag, *Metall. Mater. Trans. A* 26 (1995) 765-776.
- [27] H. J. Spies, H. Biermann and A. Fischer, *Z. Metallk.* 96 (2005) 781-786.
- [28] S. Meka, S. S. Hosmani, A. R. Clauss and E. J. Mittemeijer, *Int. J. Mater. Res.* 99 (2008) 808-814.
- [29] Landolt-Börnstein, *Numerical data and functional relationships in science and technology, New series, Group III: Crystal and solid state physics, Vol. 7c, Crystal structure data of inorganic compounds*, Springer-Verlag Berlin (1978).
- [30] Q. Xia, H. Xia and A. L. Ruoff, *J. Appl. Phys.* 73 (1993) 8198-8200.
- [31] W. Mader, D. Birkhölzer and H. Ichinose, *DVS-Berichte* 129 (1990) 93-97.
- [32] I. Petrov, E. Mojab, R. C. Powell, J. E. Greene, L. Hultman and J. E. Sundgren, *Appl. Phys. Lett.* 60 (1992) 2491-2493.
- [33] K. H. Jack, *Proceedings of the conference on heat treatment 1973* (1975) 39-50.



- [34] J. S. Steenaert, M. H. Biglari, C. M. Brakman, E. J. Mittemeijer and S. van der Zwaag, *Z. Metallk.* 86 (1995) 700-705.
- [35] W. Pitsch and A. Schrader, *Arch. Eisenhüttenw.* 29 (1958) 715-721.
- [36] M. A. J. Somers, R. M. Lankreijer and E. J. Mittemeijer, *Philos. Mag. A* 59 (1989) 353-378.
- [37] V. A. Phillips and A. U. Seybolt, *Trans. TMS-AIME* 242 (1968) 2415-2422.
- [38] W. Koch, C. Ilschner-Gensch and H. Rohde, *Arch. Eisenhüttenw.* 27 (1956) 701-706.
- [39] L. Rademacher, M. Hooek and K. K. Mehta, *Thyssen Edelst. Techn. Ber.* 5 (1979) 162-169.
- [40] R. Wiedemann, H. Oettel and D. Bergner, *HTM* 47 (1992) 14-20.
- [41] V. Massardier, L. Voron, C. Esnouf and J. Merlin, *J. Mater. Sci.* 36 (2001) 1363-1371.
- [42] E. J. Mittemeijer and M. A. J. Somers, *Surf. Eng.* 13 (1997) 483-497.
- [43] JCPDS-International Centre for Diffraction Data (2002), PCPDFWIN, Version 2.3.
- [44] J. L. Pouchou and F. Pichoir, *Rech. Aerosp.* (1984) 167-192.
- [45] A. Barna, *Materials Research Society Symposium Proceedings* 254 (1992) 3-22.
- [46] D. B. Williams and C. B. Carter, *Transmission electron microscopy*, New York, Plenum Press (1996).
- [47] S. S. Hosmani, R. E. Schacherl and E. J. Mittemeijer, *Acta Mater.* 54 (2006) 2783-2792.
- [48] M. H. Biglari, C. M. Brakman, E. J. Mittemeijer and S. van der Zwaag, *Philos. Mag. A* 72 (1995) 931-947.
- [49] S. Chen and J. Morris, *Metall. Mater. Trans. A* 8 (1977) 19.
- [50] G. Cliff and G. W. Lorimer, *J. Microsc.-Oxf.* 103 (1975) 203-207.
- [51] S. S. Hosmani, R. E. Schacherl and E. J. Mittemeijer, *J. Mater. Sci.* 43 (2008) 2618-2624.
- [52] S. S. Hosmani, R. E. Schacherl, L. Lityńska-Dobrzyńska and E. J. Mittemeijer, *Philos. Mag.* in press (2008).

- 
- [53] P. H. Mayrhofer, D. Music, T. Reeswinkel, H. G. Fuss and J. M. Schneider, *Acta Mater.* 56 (2008) 2469-2475.
- [54] C. G. Lee, Y. Iijima, T. Hiratani and K. Hirano, *Mater. Trans.* 31 (1990) 255-261.
- [55] M. Gemmaz, M. Afyouni and A. Mosser, *Surf. Sci.* 227 (1990) L109-L111.
- [56] J. D. Fast and M. B. Verrijp, *J. Iron Steel Inst.* 176 (1954) 24-27.
- [57] N. E. Vives Diaz, S. S. Hosmani, R. E. Schacherl and E. J. Mittemeijer, *Acta Mater.* 56 (2008) 4137-4149.
- [58] Z. Nishiyama, *Sci. Rep. Tohoku Univ.* 23 (1934) 637-664.
- [59] G. Wassermann, *Arch. Eisenhüttenw.* 6 (1933) 347-351.
- [60] U. Dahmen, *Acta Metall.* 30 (1982) 63-73.
- [61] Y. L. He, S. Godet and J. J. Jonas, *J. Appl. Cryst.* 39 (2006) 72-81.

## Chapter 3

# Phase transformation of mixed $\text{Cr}_{1-x}\text{Al}_x\text{N}$ nitride precipitates in ferrite

*A. R. Clauss, E. Bischoff, R. E. Schacherl and E. J. Mittemeijer*

### Abstract

Nitriding of specimens with the composition Fe–1.5wt.%Cr–1.5wt.%Al (Fe–1.6at.%Cr–3.1at.%Al) at 853 K leads to the formation of mixed, ternary  $\text{Cr}_{1-x}\text{Al}_x\text{N}$  nitride platelets precipitated in the cubic, rock-salt structure type obeying a Bain-type orientation relationship with the ferrite matrix. Upon subsequent annealing (at 973 K) the mixed, ternary nitrides transform into the two equilibrium, binary nitrides, namely CrN of cubic, rock-salt structure type in the Bain orientation relationship with the ferrite matrix and AlN of hexagonal, wurtzite structure type, obeying a Pitsch–Schrader orientation relationship with the ferrite matrix. At the same time the mobile excess nitrogen, dissolved in the ferrite matrix, diffuses towards the originally not nitrated core, where relatively coarse, cubic CrN and hexagonal AlN precipitates develop. The microstructure and (local) composition changes have been analysed by XRD, (HR)TEM, STEM, EDX and EPMA. It was found that the transformation proceeds by Al depletion of the original mixed  $\text{Cr}_{1-x}\text{Al}_x\text{N}$  precipitates.

### 3.1 Introduction; instability of nitrides

Nitriding is a thermochemical surface engineering process that is widely used in industry to improve technical properties of ferritic steel workpieces like the resistance against fatigue, wear and corrosion [1-3]. Nitriding implies the introduction of nitrogen into the specimen/workpiece through its surface. Alloying elements like Al and Cr have a strong affinity for nitrogen and can form nitride precipitates in the ferrite matrix, which improves the mechanical strength drastically [4, 5].

Very often a gas mixture containing  $\text{NH}_3$  is used as nitriding medium. During gaseous nitriding the chemical activity of nitrogen dissolved in the specimen at its surface can be accurately adjusted by the so-called nitriding potential  $r_{\text{N}} = \frac{P_{\text{NH}_3}}{P_{\text{H}_2}^{3/2}}$  [6].

By setting the value of the nitriding potential, the whether or not occurrence of a layer of iron nitrides at the surface, in addition to the formation of alloying-element nitrides in the ferritic matrix, can be controlled.

It should be realised that local (thermodynamic) equilibrium with the nitriding atmosphere can only be realised at the surface. As a matter of fact, beneath the surface the iron nitrides are metastable with respect to decomposition in iron and nitrogen gas (which leads to pore/channel formation along grain boundaries [6, 7]). Also the alloying-element nitrides developing in the ferritic substrate can be metastable. For example, the equilibrium modification of AlN is the hexagonal, wurtzite structure type. However, the nucleation of this thermodynamically stable structure is difficult in an annealed ferrite matrix [4, 8-11] and more easily nucleating metastable cubic, rock-salt structure type AlN precipitates occur, in particular in cold-rolled specimens. Transformation from such cubic AlN precipitates to hexagonal, wurtzite structure type AlN precipitates upon annealing of an Fe–Al–N alloy at 973 K was observed [12].

It was recently shown that upon nitriding a ternary Fe–Cr–Al alloy,  $\text{Cr}_{1-x}\text{Al}_x\text{N}$  precipitates of the cubic, rock-salt structure type develop in the ferrite matrix (cf. chapter 2). The development of  $\text{Cr}_{1-x}\text{Al}_x\text{N}$  precipitates is the consequence of kinetics: Al cannot precipitate separately as hexagonal, equilibrium AlN due to difficult nucleation. Instead mixed, cubic  $\text{Cr}_{1-x}\text{Al}_x\text{N}$  precipitates of rock-salt structure type develop and cause a considerable (although not maximal) amount of energy release. Such mixed, ternary nitrides may be unstable with respect to decomposition into the thermodynamically stable binary nitrides, i.e. CrN of cubic, rock-salt structure type and AlN of hexagonal, wurtzite structure type.

The purpose of the present paper is to investigate the behaviour of these presumably metastable, mixed nitrides upon annealing. Does the mixed nitride decompose? Further, if AlN precipitates directly upon such annealing, which crystal structure does occur? Moreover, an accompanying effect of the annealing after the nitriding is a

redistribution of the (mobile) excess nitrogen in the nitrated zone, which hitherto has not been investigated.

## 3.2 Experimental

### 3.2.1 Specimen preparation

Specimens were prepared as described in chapter 2. The chemical composition and the amount of impurities were measured by chemical analysis (inductively coupled plasma – optical emission spectroscopy, carrier gas hot extraction and combustion method). The thus determined alloy composition is shown in Table 3.1.

Table 3.1

Amounts of alloying elements and impurities of the used alloy.

Alloy	Cr		Al		N	O	S	C
	(wt.%)	(at.%)	(wt.%)	(at.%)	(wt.%)	(wt.%)	(wt.%)	(wt.%)
Fe–Cr–Al	1.52 ± 0.01	1.60 ± 0.01	1.52 ± 0.01	3.09 ± 0.02	< 0.0005	0.0043 ± 0.0004	< 0.0010	0.0025 ± 0.0002

The element distribution (homogeneity) was proven by electron probe microanalysis. No segregation was observed. The recrystallised specimens with a dimension of  $20 \times 15 \times 1 \text{ mm}^3$  had an average grain diameter of 22  $\mu\text{m}$ .

### 3.2.2 Nitriding and subsequent annealing

Gaseous nitriding was performed in a vertical, multizone quartz-tube furnace at 853 K (cf. chapter 2). The gas fluxes of  $\text{H}_2$  and  $\text{NH}_3$  were adjusted by means of mass-flow controllers. The corresponding nitriding potential (cf. Refs. [6] and [7]) was  $r_N = 0.104 \text{ atm}^{-1/2}$ . Under the chosen nitriding potential no iron nitrides develop at the surface, i.e. the nitrated layer consists only of the diffusion zone with nitride precipitates of the alloying elements.

After nitriding the specimens were annealed. To this end they were put in an  $\text{Al}_2\text{O}_3$ -crucible which was encapsulated in an evacuated quartz tube under a protective argon gas atmosphere (purity Ar: 99.999 vol.%) with a pressure of 0.3 atm (equivalent to 1 atm at 973 K). Subsequently the quartz tube was put into a muffle furnace at a temperature of about 973 K. After 168 h annealing time the quartz tube was taken out of the furnace and cooled down to ambient temperature.

### 3.2.3 Microstructural analysis

Phase analysis by X-ray diffraction applied to the surface of all specimens before nitriding, after nitriding and after subsequent annealing was performed on both a PANalytical (formerly Philips) X'Pert Multi-Purpose Diffractometer (MPD) in Bragg-Brentano geometry and a PANalytical (formerly Philips) Materials-Research Diffractometer (MRD) with a quasi-parallel beam geometry. Both diffractometers were equipped with graphite-diffracted beam monochromators set to Co-K $\alpha$  radiation. The specimens were rotated on a spinner around their vertical axis during each measurement, to improve crystal statistics. The diffraction angle  $2\theta$  was scanned over a range from 30° until 140° in steps of 0.05° (MPD) and 0.04° (MRD) with a counting time of 10 s (MPD) and 100 s up to 120 s (MRD) per step. Detected phases were identified by  $2\theta$  positions of their diffraction peaks in comparison with data from the ICDD data base [13].

Concentration depth profiles were determined by electron probe microanalysis (EPMA) performed on polished cross-sections. For light microscopy a piece of each nitrided and annealed specimen was cut off, embedded, ground, polished and etched with 2.5 % Nital (2.5 vol.% HNO<sub>3</sub> in ethanol) at a temperature of about 323 K for about 200 s. The microhardness was measured along the EPMA line-scans on the cross-sections of nitrided and annealed specimens. For details regarding the methods used for EPMA, light microscopy and microhardness measurements, see chapter 2.

Transmission electron microscopy (TEM) was applied to investigate the (crystal) structure and morphology of the nitride precipitates in the nitrided and annealed specimens. For this purpose TEM samples were produced by either the jet-electropolishing technique or by argon ion milling (cf. chapter 2 for details) from different depths of the nitrided and annealed zone. Specimens prepared by both preparation methods provide complementary insight (see section 3.3.2). Two different precipitate crystal structures and orientation relationships (OR) with the ferrite matrix are relevant for the analyses of the selected area diffraction patterns (SADPs) in the present work:

(i) the Bain-type OR [14] (sometimes also called after Baker and Nutting [15]) between the bcc ferrite matrix and the nitride (MeN) fcc rock-salt structure type precipitates

$$\{001\}_{\alpha\text{-Fe}} // \{001\}_{\text{MeN}}, \langle 100 \rangle_{\alpha\text{-Fe}} // \langle 110 \rangle_{\text{MeN}}; \text{Me} = \text{Cr, Al},$$

(ii) the Pitsch–Schrader OR [16] between the bcc ferrite matrix and nitride (MeN) hcp wurtzite structure type precipitates

$$\{110\}_{\alpha\text{-Fe}} // \{0001\}_{\text{MeN}}, \langle 001 \rangle_{\alpha\text{-Fe}} // \langle 11\bar{2}0 \rangle_{\text{MeN}}; \text{Me} = \text{Al}.$$

Schematic SADPs with  $[001]_{\alpha\text{-Fe}}$  incident electron-beam axis pertaining to the two cases above are shown in Fig. 3.1. The experimentally recorded SADPs (cf. section 3.3) exhibit additional spots at forbidden  $100_{\alpha\text{-Fe}}$  sites. These spots originate from  $220_{\text{Fe}_3\text{O}_4}$  reflections due to unavoidable oxidation at the faces of the electron-transparent foils [4, 17, 18].

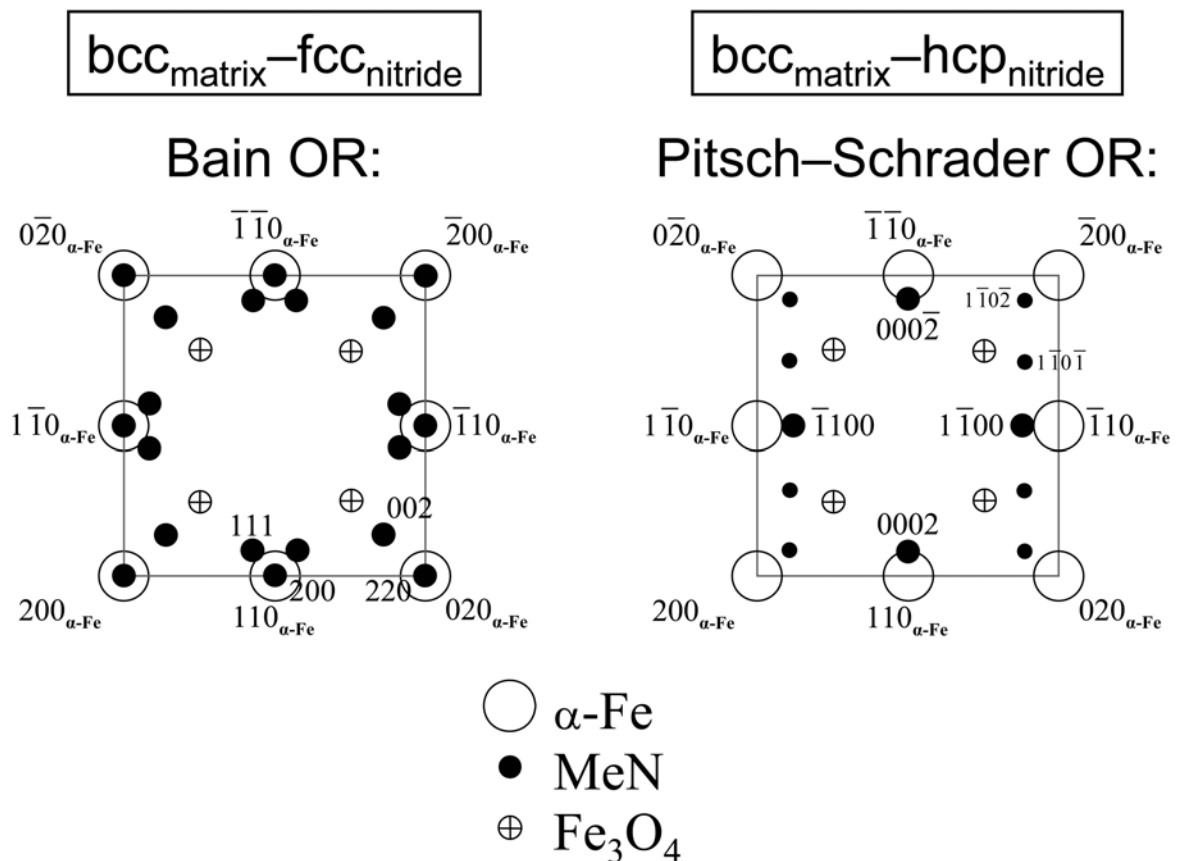


Fig. 3.1: Schematic SADPs with  $[001]_{\alpha\text{-Fe}}$  incident electron-beam axis pertaining to the Bain orientation relationship (OR) between cubic, rock-salt structure type precipitates and the ferrite matrix (including superposition of all variants) and of the Pitsch–Schrader OR between hexagonal, wurtzite structure type precipitates and the ferrite matrix (for clarity here only one variant is shown).

Scanning transmission electron microscopy (STEM) was applied to get information about the chemical composition of individual nitride precipitates. High resolution transmission electron microscopy (HRTEM) was performed in particular to reveal the structure of the precipitate/matrix interfaces. For details of the instruments and techniques used, see chapter 2.

### 3.3 Results and discussion

#### 3.3.1 Concentration depth and microhardness depth profiles; after nitriding and after subsequent annealing

EPMA concentration depth profiles of a nitrided (15 h at 853 K) and subsequently annealed (168 h at 973 K) specimen are shown in Fig. 3.2 a together with the corresponding LM micrograph. The depicted graph in Fig. 3.2 a consists of six graphically superimposed line-scans, determined at different locations on the cross-section perpendicular to the specimen surface. The dashed vertical white lines denote the depths from which TEM samples were prepared. The dotted horizontal black line denotes the so-called *normal* amount of N (i.e.  $[N]_{\text{normal}}$ ), which is necessary to transform all alloying elements (Al and Cr substitutionally dissolved in ferrite) into AlN, CrN and/or mixed  $\text{Cr}_{1-x}\text{Al}_x\text{N}$  precipitates (i.e.  $[N]_{\text{MeN}}$ ) plus the amount of N, which can be dissolved interstitially in the remaining pure, unstrained ferrite matrix in thermodynamic equilibrium with the nitriding gas atmosphere at the applied nitriding conditions (i.e.  $[N]_{\alpha\text{-Fe}}^0 = 0.30 \text{ at.}\%$  in pure ferrite [19]). The amount of N in excess of this normal amount is called “*excess*” nitrogen [19-22].

During nitriding of an Fe–1.5wt.%Cr–1.5wt.%Al specimen for 15 h at 853 K cracks develop along grain boundaries, in particular those running more or less from the surface towards the specimen centre (cf. the LM micrograph in Fig. 3.2 a); the nitrided layer is brittle. The nitrided zone *before* annealing ranges until a depth of about 360  $\mu\text{m}$  (cf. Fig. 3.2 b). After annealing the nitrogen is, overall, distributed more or less evenly over the cross-section of the specimen, except near the surface where the nitrogen concentration decreases towards the outer surface as a consequence of outward diffusion of N during annealing (see the EPMA concentration depth profiles



in Figs. 3.2 a and b). In the initially unnitrided core the N and Cr atomic concentrations scatter strongly after the annealing (see, for N, Cr and Al, at the “specimen centre” area in Fig. 3.2 a and for N also in Fig. 3.2 b).

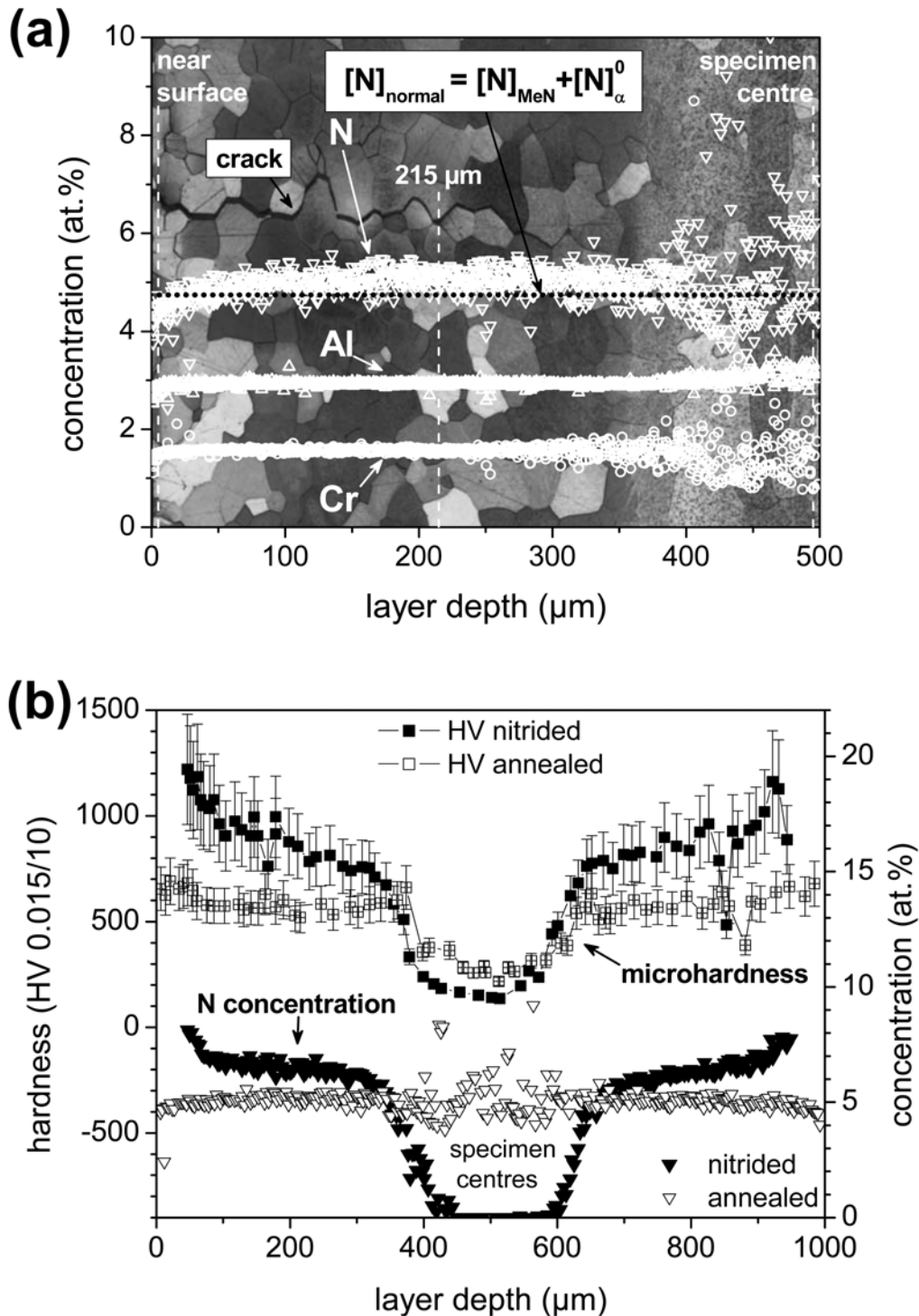


Fig. 3.2: (a) EPMA concentration depth profiles of a nitrided and annealed specimen together with the corresponding LM micrograph. The dashed vertical white lines indicate the depths at which TEM samples were prepared. The dotted horizontal black line represents the normal amount of N (see text). (b) Comparison of the microhardness depth profiles and the N concentration depth profiles of both an only nitrided specimen and a nitrided and subsequently annealed specimen. The centre lines of both specimens have been made coincident.

As can be concluded from the difference between the N concentration depth profiles after only nitriding and after nitriding plus annealing (Fig. 3.2 b), during annealing the *mobile* excess (i.e. dissolved in the  $\alpha$ -Fe matrix) nitrogen apparently diffuses towards the formerly not nitrided core. After the annealing the amount of nitrogen remaining in the former diffusion zone is still higher than the “normal” amount of nitrogen (cf. dotted horizontal black line in Fig. 3.2 a). This is ascribed to the presence of immobile excess nitrogen, which is trapped at the precipitate/matrix interface (cf. chapter 2).

After EPMA the embedded cross-section was etched to uncover the trace of the electron beam line-scan. Along such an EPMA line-scan the microhardness values were determined to get a microhardness depth profile. The N atomic concentration depth profiles of a specimen after nitriding and of a specimen after subsequent annealing together with the corresponding microhardness depth profiles are shown in Fig. 3.2 b. In view of the different widths of the cross sections of the two specimens, the centre line of the nitrided specimen was made coincident with the centre line of the nitrided plus annealed specimen. It follows that the microhardness depth profiles and the corresponding N concentration depth profiles have the same characteristic course, except in the core of the annealed specimen, where the N concentration scatters strongly, and the hardness values are only slightly increased as compared to the hardness increase observed upon nitriding in the initially nitrided zone, with reference to the formerly unnitrided core. The maximum Vickers microhardness at the nitrided specimen surface of about 1200 HV 0.015 had decreased upon annealing to a value of about 600 HV 0.015. The decrease of the microhardness during annealing, in particular in the near-surface region, indicates a coarsening and/or a transformation of the initially platelet-like (semi)coherent  $\text{Cr}_{1-x}\text{Al}_x\text{N}$  precipitates. The microhardness in the unnitrided core of about 150 HV 0.015 had increased to about 300 HV 0.015 upon annealing. This microhardness increase in the formerly unnitrided core is due to inward diffusion of excess nitrogen and the formation of relatively coarse and incoherent equilibrium nitride precipitates (cf. section 3.3.2.3), which explains the scatter in the N, Cr and Al concentrations in this region.

### 3.3.2 Precipitates after nitriding and after subsequent annealing; structure, composition and orientation relationships

#### 3.3.2.1 Near the surface

X-ray diffraction analyses were carried out on specimen surfaces before nitriding, after nitriding and after subsequent annealing; the corresponding diffractograms are shown in Fig. 3.3 a. No new phase is identifiable in the diffractogram after nitriding. However, a strong broadening of the ferrite-matrix reflections is apparent. This is due to the presence of tiny nitride precipitates, which diffract coherently with the ferrite matrix (see Ref. [23]). TEM and STEM–EDX analyses have shown that these precipitates are mixed  $\text{Cr}_{1-x}\text{Al}_x\text{N}$  nitrides (cf. chapter 2).

Annealing after nitriding leads to strong decrease of the line broadening of the ferrite-matrix reflections. Also some tiny intensity humps occur at the low-angle side of the  $\alpha\text{-Fe}$  110 reflection in the X-ray diffractograms; see Fig. 3.3 b. The intensity humps can be assigned to reflections from hexagonal AlN in the wurtzite structure that evidently diffracts incoherently with respect to the ferrite matrix. The presence of cubic, rock-salt AlN nitride and cubic, rock-salt CrN nitride cannot be verified because of overlap of corresponding nitride reflections with ferrite reflections. Therefore TEM analysis was performed next.

A BF image of a *jet-electropolished* TEM sample from near the surface (cf. Fig. 3.2 a), together with corresponding SADPs and EDX spectra, is shown in Fig. 3.4. “Round” particles are visible. The dissolution of the ferrite matrix during jet-electropolishing leads partially to “loosening” of the nitride particles (see the round particles in Fig. 3.4) and a distinct OR with the matrix then no longer occurs. The dark round particles on the BF image were big enough to get a separate SADP of mainly such a particle. By means of the measured lattice spacings in combination with the results from the EDX spectra (compare counting rate for Cr in the “matrix” spectrum and in the “round particle” spectrum; the Fe counts in the particle spectrum are from the surrounding matrix), the round particles can be identified as cubic, rock-salt structure type CrN.

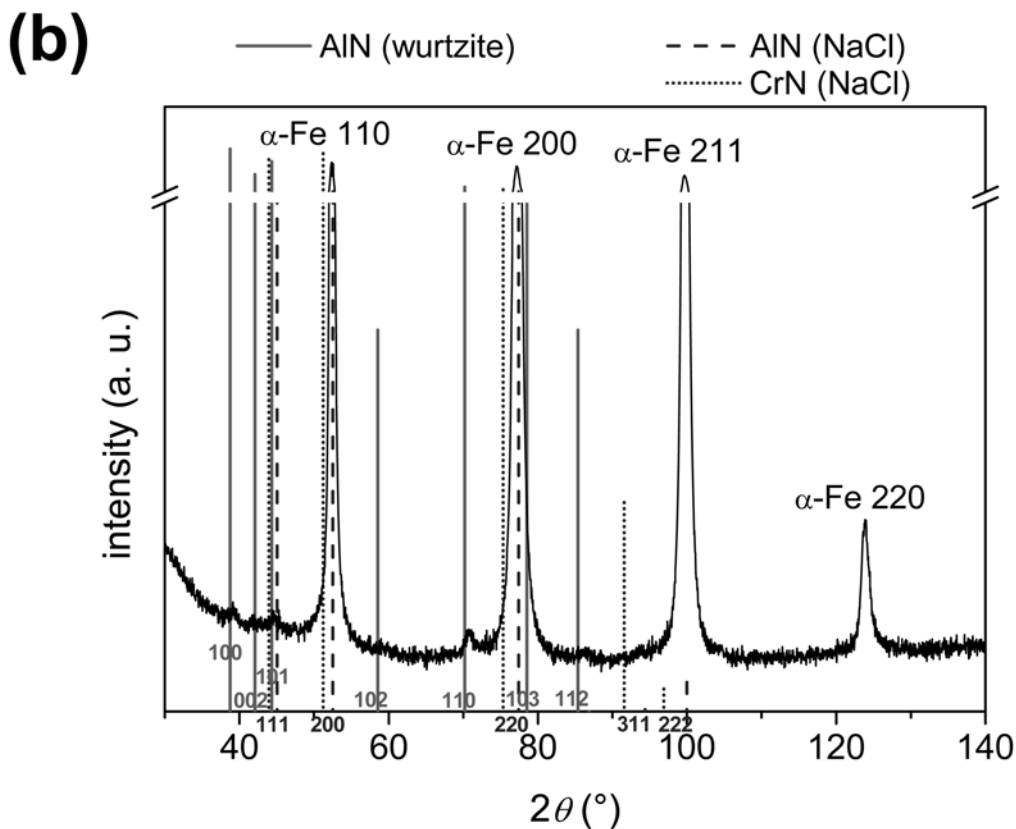
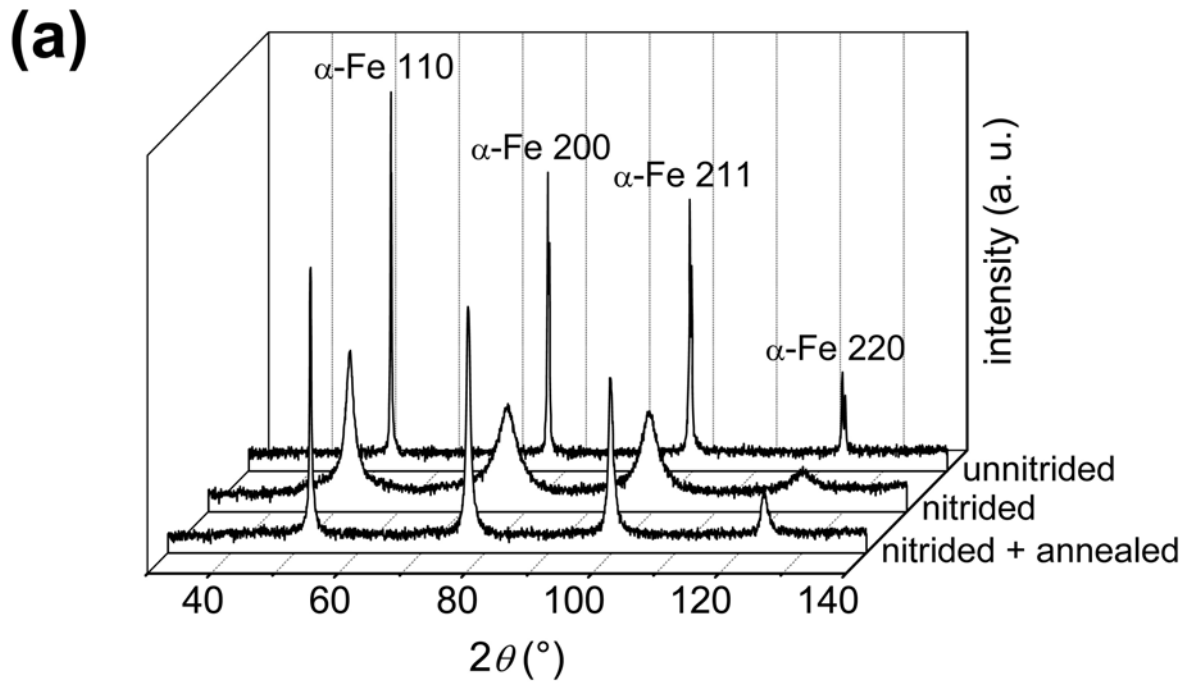


Fig. 3.3: (a) X-ray diffractograms taken from the specimen surface before nitriding, after nitriding and after nitriding and annealing (counting time 10 s/step). After nitriding a very pronounced peak broadening occurs, which becomes reduced upon subsequent annealing. (b) X-ray diffractogram of the specimen surface after nitriding and annealing recorded applying longer counting times (100 s/step) than in Fig. 3.3 a in order to identify the intensity humps at the low-angle side of the  $\alpha$ -Fe 110 reflection. Small peaks from the hexagonal AlN wurtzite structure can be observed. Presence or absence of peaks from the cubic-rock salt structure type AlN and CrN cannot be confirmed, because they generally are subject to strong overlapping with ferrite-matrix reflections.

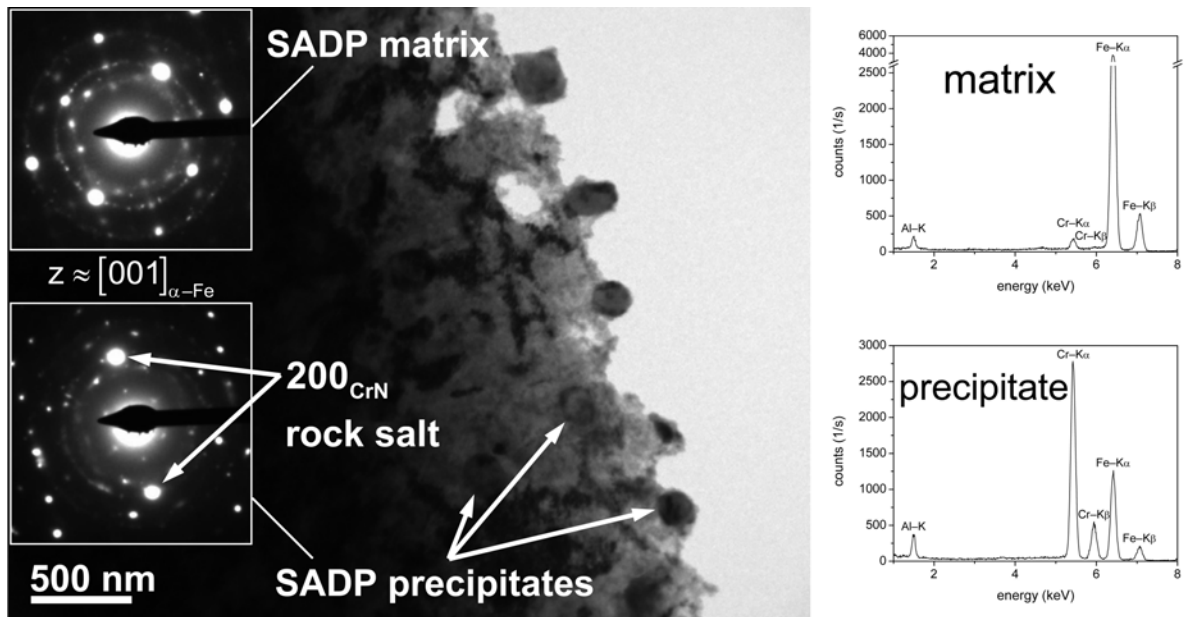


Fig. 3.4: BF image of a jet-electropolished TEM sample from the nitrated and annealed specimen near the surface, together with corresponding SADPs (electron-beam axis near  $[001]_{\alpha-Fe}$ ) and EDX spectra of the ferrite matrix and precipitate (round particle).

An HRTEM image of an *ion-milled* TEM sample from near the surface (cf. Fig. 3.2 a) is shown in Fig. 3.5. By this type of TEM specimen preparation the cohesion of nitride particles and matrix is maintained, in contrast with the jet-electropolishing technique (see above). In the dotted square A a roundish precipitate can be recognised (cf. white arrow) whereas in the solid square B two differently oriented smaller, more platelet-like precipitates are visible (cf. white arrows), which are perpendicular to each other. Fast Fourier transformation (FFT) patterns have been generated from selected regions from the square areas A and B. The FFT pattern of area A is congruent with the Pitsch–Schrader OR whereas the FFT pattern of area B is congruent with the Bain OR (cf. Fig. 3.1).

For the determination of the chemical composition of the nitride precipitates in the ion-milled foils, EDX line-scans were recorded by STEM. A STEM BF image of three adjacent grains in an ion-milled sample from the nitrated and annealed specimen near the surface is shown in Fig. 3.6, together with the results of the STEM line-scans (EDX), along paths indicated by the arrows b and c in the BF image. The drift of the samples imposed a practical limit on the counting time, and therefore, in contrast with the successful recording of the Cr and Al line-scans shown in the figure, a reliable

nitrogen line-scan could not be obtained (for details of the quantitative analysis see chapter 2).

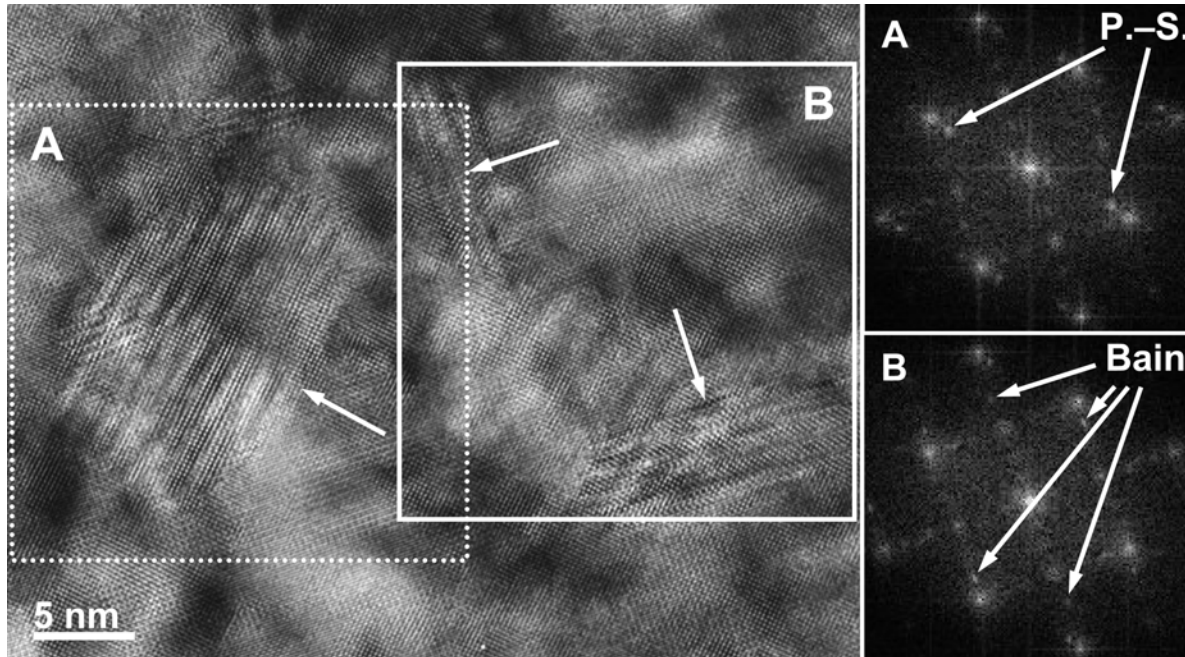


Fig. 3.5: HRTEM image of an ion-milled TEM sample from the nitrated and annealed specimen near the surface (electron-beam axis:  $[001]_{\alpha\text{-Fe}}$ ). The FFT patterns generated from an area with the roundish precipitate in the dotted square A and from an area with platelet-like precipitates in the solid square B are shown at the right. The roundish particle in A exhibits a Pitsch–Schrader OR with the ferrite matrix, whereas the more platelet-like particles in B satisfy the Bain OR with the ferrite matrix (cf. Fig. 3.1).

Along the grain boundaries and at the triple junction shown in Fig. 3.6 relatively large particles are visible with bright contrast. STEM line-scan b crosses such a particle. The line-scan reveals the distinct presence of Al, and not of Cr, in the particle. Such bright but smaller precipitates are also visible inside the grains. The STEM line-scan c across such a smaller precipitate shows a similar result like that for the bigger particle.

The above results, combined XRD and TEM, can be summarised: after annealing the microstructure in the near surface region reveals the presence of cubic, rock-salt structure type chromium-rich precipitates (“CrN”) and hexagonal, wurtzite structure type aluminium-rich precipitates (“AlN”). The particle size varies from 10 nm to 50 nm and more; the thickness of the initial  $\text{Cr}_{1-x}\text{Al}_x\text{N}$  platelets is 1-2 nm (cf. chapter 2). The cubic precipitates exhibit a Bain OR with the ferrite matrix, the hexagonal precipitates show a Pitsch–Schrader OR with the ferrite matrix. These results imply that in the near-surface region the initially present cubic, rock-salt

structure type  $Cr_{1-x}Al_xN$  precipitates are replaced by AlN and CrN upon sufficiently long annealing after nitriding.

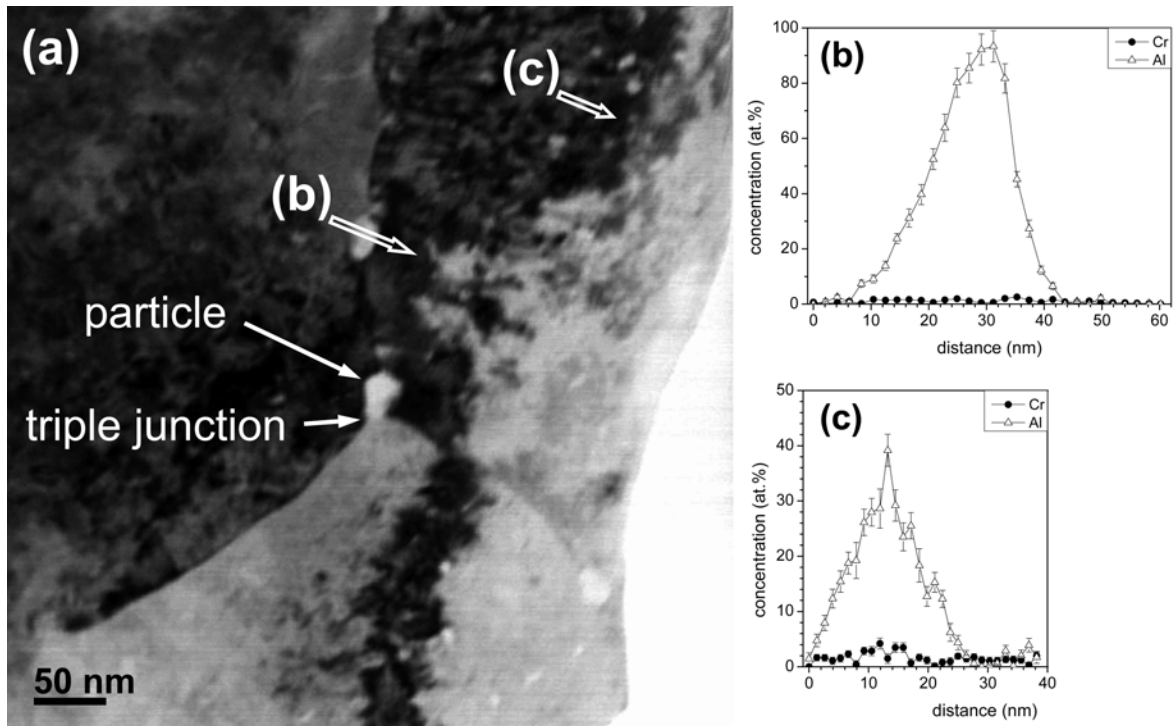


Fig. 3.6: (a) STEM BF image of three adjacent grains with triple junction in an ion-milled sample from the nitrided and annealed specimen near the surface and the results of STEM line-scans along paths (b) and (c) (see arrows).

### 3.3.2.2 In the nitrogen diffusion zone

A TEM BF image and corresponding DF images from an ion-milled sample, taken from the diffusion zone at a depth of about  $215\ \mu\text{m}$  (cf. Fig. 3.2 a), are shown in Fig. 3.7. The zone axis (incident electron-beam direction) is  $[001]_{\alpha\text{-Fe}}$ . Two kinds of precipitates are visible in the BF image and as evidenced by the SADP and DF images: (i) platelet-like cubic, rock-salt structure type precipitates (largely viewed edge-on for the operating zone axis of the ferrite matrix) possessing a Bain-type OR with the ferrite matrix and (ii) coarser hexagonal, wurtzite structure type precipitates exhibiting the Pitsch–Schrader OR with the ferrite matrix (cf. Fig. 3.7 and the SADP shown as inset in Fig. 3.7); see in particular the corresponding DF images taken from a rock-salt  $002_{\text{MeN}}$  spot (Fig. 3.7 b) and a wurtzite  $0002_{\text{MeN}}$  or  $1\bar{1}00_{\text{MeN}}$  (cannot be distinguished; cf. Fig. 3.1) spot (Fig. 3.7 c) indicated by circles in the SADP. The bright platelets in the DF image of Fig. 3.7 b are not exactly parallel and there is a variation in the brightness inside the platelets. Apparently deviations of the Bain OR occur along a

platelet, which is compatible with the slight splitting up of the  $002_{\text{MeN}}$  rock-salt spots in the SADP (cf. chapter 2). In the BF image the strain-field contrast around the precipitates is not pronounced, as compared to BF images from the same depth of the nitrated zone before annealing (cf. chapter 2).

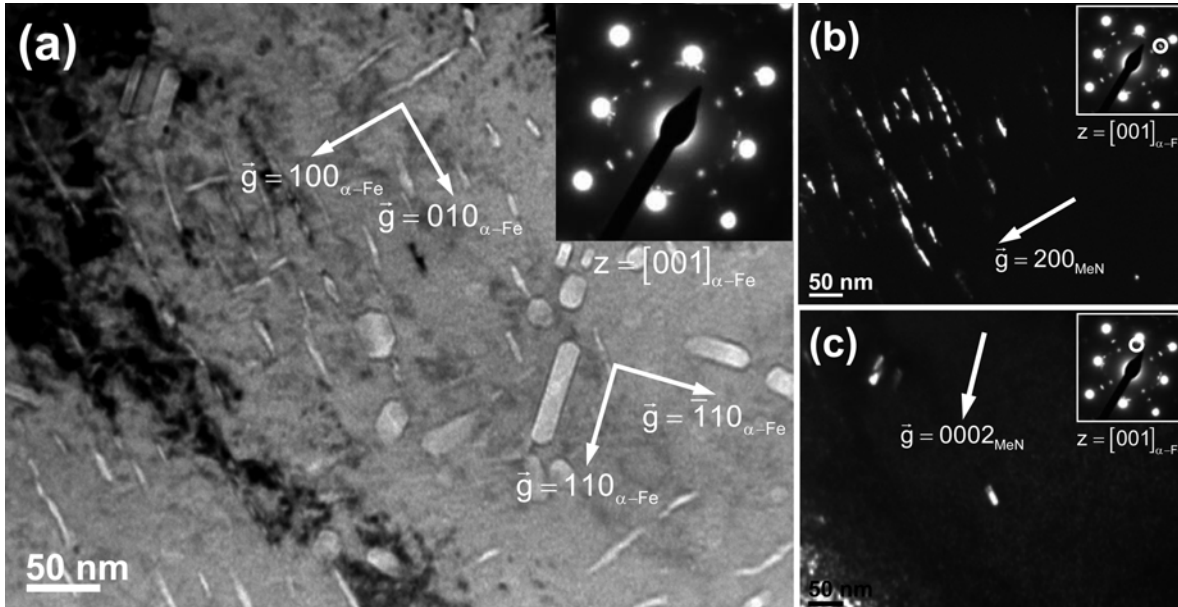


Fig. 3.7: (a) BF image and corresponding SADP of an ion-milled TEM sample from a nitrated and annealed specimen taken at a depth of about  $215 \mu\text{m}$  (electron-beam axis:  $[001]_{\alpha\text{-Fe}}$ ). (b) DF image obtained from a  $002_{\text{MeN}}$  spot of rock-salt structure type precipitates having a Bain OR with the ferrite matrix. (c) DF image obtained from a  $0002_{\text{MeN}}$  or  $1\bar{1}00_{\text{MeN}}$  (cannot be distinguished; cf. Fig. 3.1) spot of the wurtzite structure type precipitates exhibiting a Pitsch–Schrader OR with the ferrite matrix (for analysing the SADP, see Fig. 3.1).

A BF image recorded by STEM on an ion-milled sample, taken from the nitrated and annealed specimen at the same depth of about  $215 \mu\text{m}$ , is shown in Fig. 3.8 a. Two kinds of precipitates are visible with different orientation: bright particles and dark particles. The results of the STEM line-scans (EDX) shown in Figs. 3.8 b and c reveal that the bright particle b contains Al but no Cr, whereas the dark particle c contains both elements, Cr and Al. Hence, precipitates of the mixed  $\text{Cr}_{1-x}\text{Al}_x\text{N}$  cubic, rock-salt structure type are (still) present in the ferrite matrix at this depth (dark precipitate in Fig. 3.8 a). However, the Al content of the mixed  $\text{Cr}_{1-x}\text{Al}_x\text{N}$  nitride pertaining to the line-scan in Fig. 3.8 c appears to be decreased distinctly compared with STEM line-scan results from the nitrated specimen before annealing (cf. Fig. 2.7 b in chapter 2): Al depletion in  $\text{Cr}_{1-x}\text{Al}_x\text{N}$  has occurred due to the formation of the hexagonal, wurtzite AlN upon annealing.



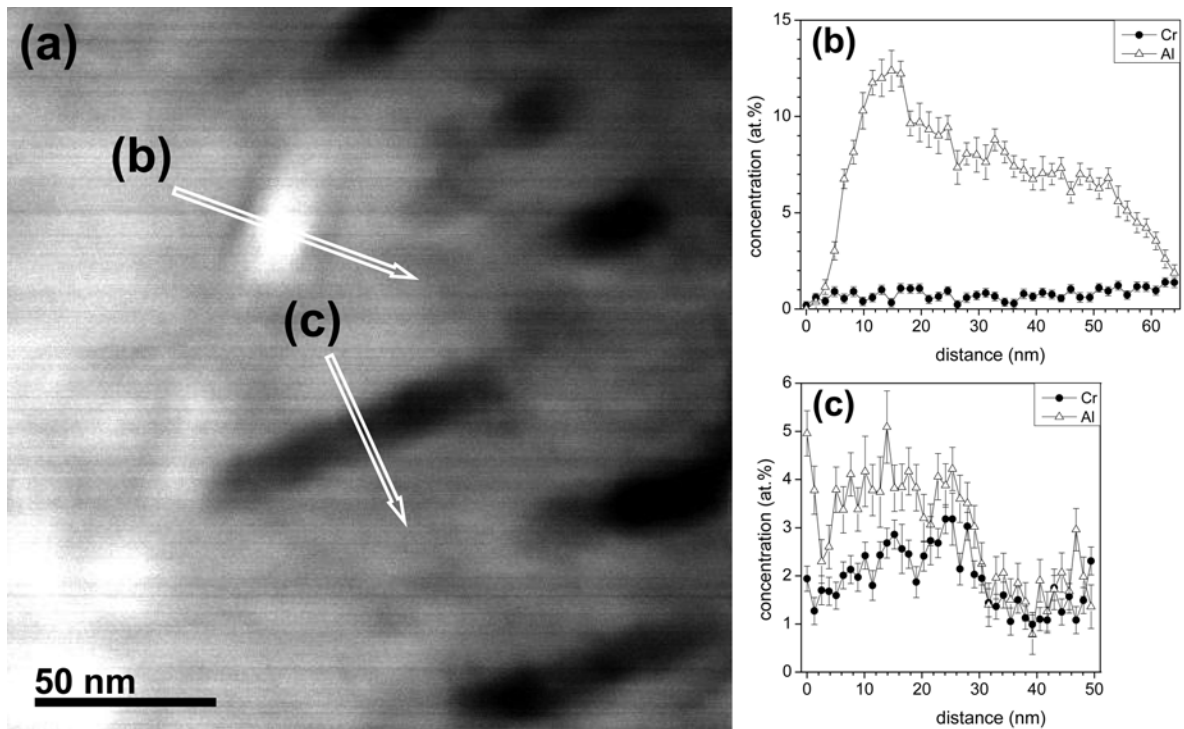


Fig. 3.8: (a) STEM BF image of an ion-milled TEM sample from a nitrided and annealed specimen taken at a depth of about 215  $\mu\text{m}$  showing two precipitates with different contrast. The image quality is poor because of the ferromagnetism of the material. (b) Results of the STEM line-scan of the bright precipitate in Fig. 3.8 a (see arrow). (c) Results of the STEM line-scan of the dark precipitate in Fig. 3.8 a (see arrow).

The above results suggest that the replacement of the initial cubic  $\text{Cr}_{1-x}\text{Al}_x\text{N}$  precipitates by (equilibrium) cubic CrN and hexagonal AlN precipitates, proceeds by Al depletion of the initial  $\text{Cr}_{1-x}\text{Al}_x\text{N}$  precipitates, which eventually become CrN, under simultaneous coarsening.

### 3.3.2.3 In the initially unnitrified core

Excess nitrogen from the original nitrogen diffusion zone diffuses upon annealing inwardly and brings about a “nitriding” of the initially unnitrified core (cf. Fig. 3.2 and its discussion in section 3.3.1). An EPMA concentration depth profile in the region of the specimen centre (before annealing: the unnitrified core) of an annealed specimen, together with the corresponding scanning electron microscopy (SEM) image, is shown in Fig. 3.9. The white arrow shows the trace of the line-scan. The dashed vertical lines denote points where the electron beam crossed black particles, which evidently led to local, abrupt increases of the N and Cr concentrations. These black particles, thus likely CrN, occur mainly along grain boundaries of the ferrite matrix and only sporadically within the grains. The Al concentration shows also a larger variation in the originally unnitrified core, as compared to the originally nitrified zone and the

un-nitrided state, but much less pronounced as for the Cr and N concentrations: apparently a distinctly preferred precipitation of AlN at grain boundaries does not occur (see what follows).

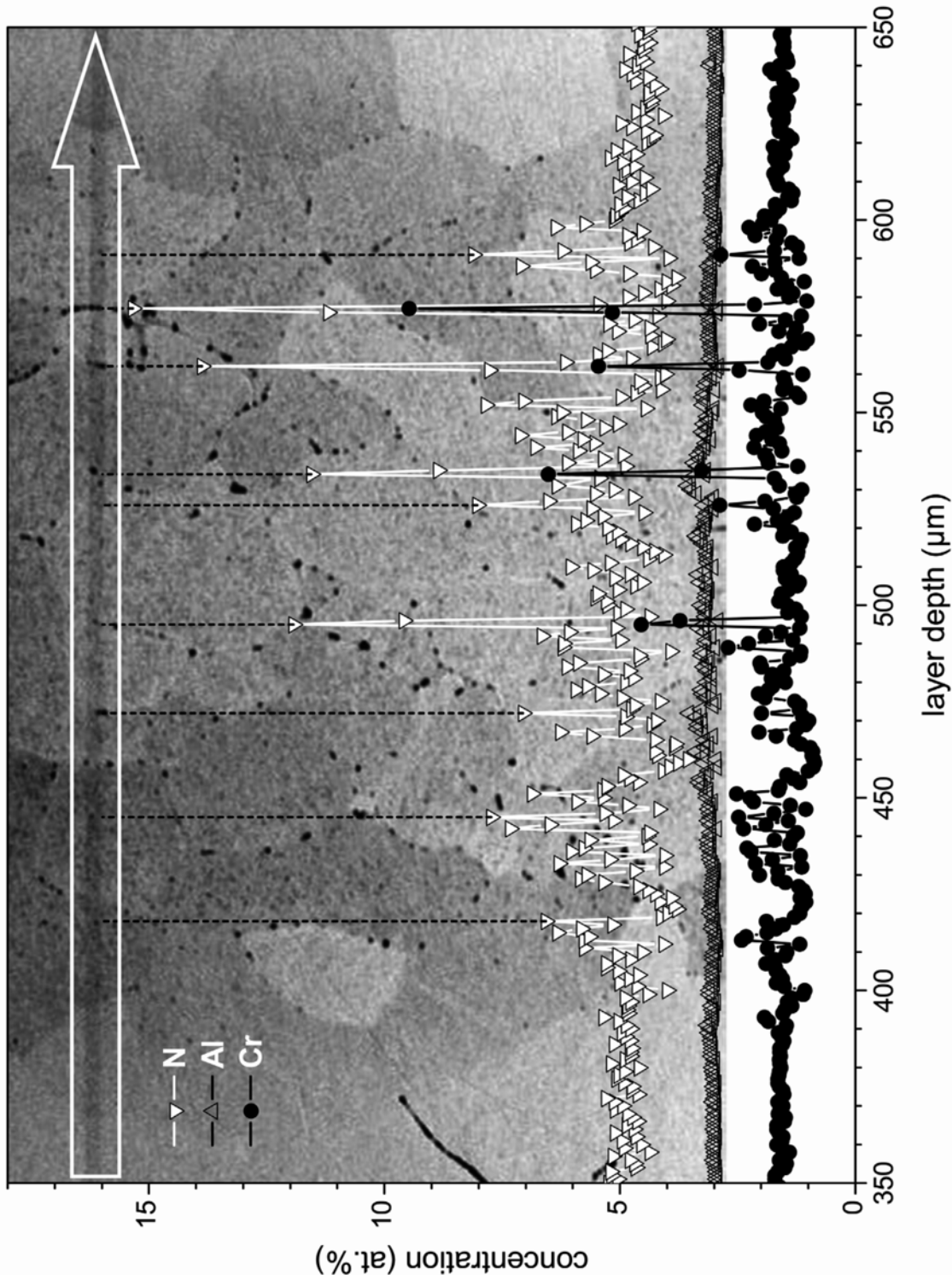


Fig. 3.9: EPMA concentration depth profile from the region around the specimen centre (initially the un-nitrided core) after nitriding and subsequent annealing, together with the corresponding SEM micrograph. The white arrow indicates the course of the line-scan. The dashed vertical black lines denote points where the electron beam hit black particles mostly at matrix grain boundaries, which exhibit a local concentration increase of N and Cr.

XRD phase analysis of the core region was carried out, with a high counting time, by recording an X-ray diffractogram from the surface obtained after material removal from one side of the specimen by grinding and polishing. The thus obtained diffractogram is shown in Fig. 3.10. Sharp reflections are visible, in addition to the ferrite-matrix reflections, the positions of which agree well with corresponding data from the ICDD data base [13] for both the hexagonal AlN wurtzite structure type phase and the cubic CrN rock-salt structure type phase. The presence of cubic, rock-salt structure type AlN cannot be excluded since the important possible reflections suffer from severe overlap with ferrite and CrN reflections.

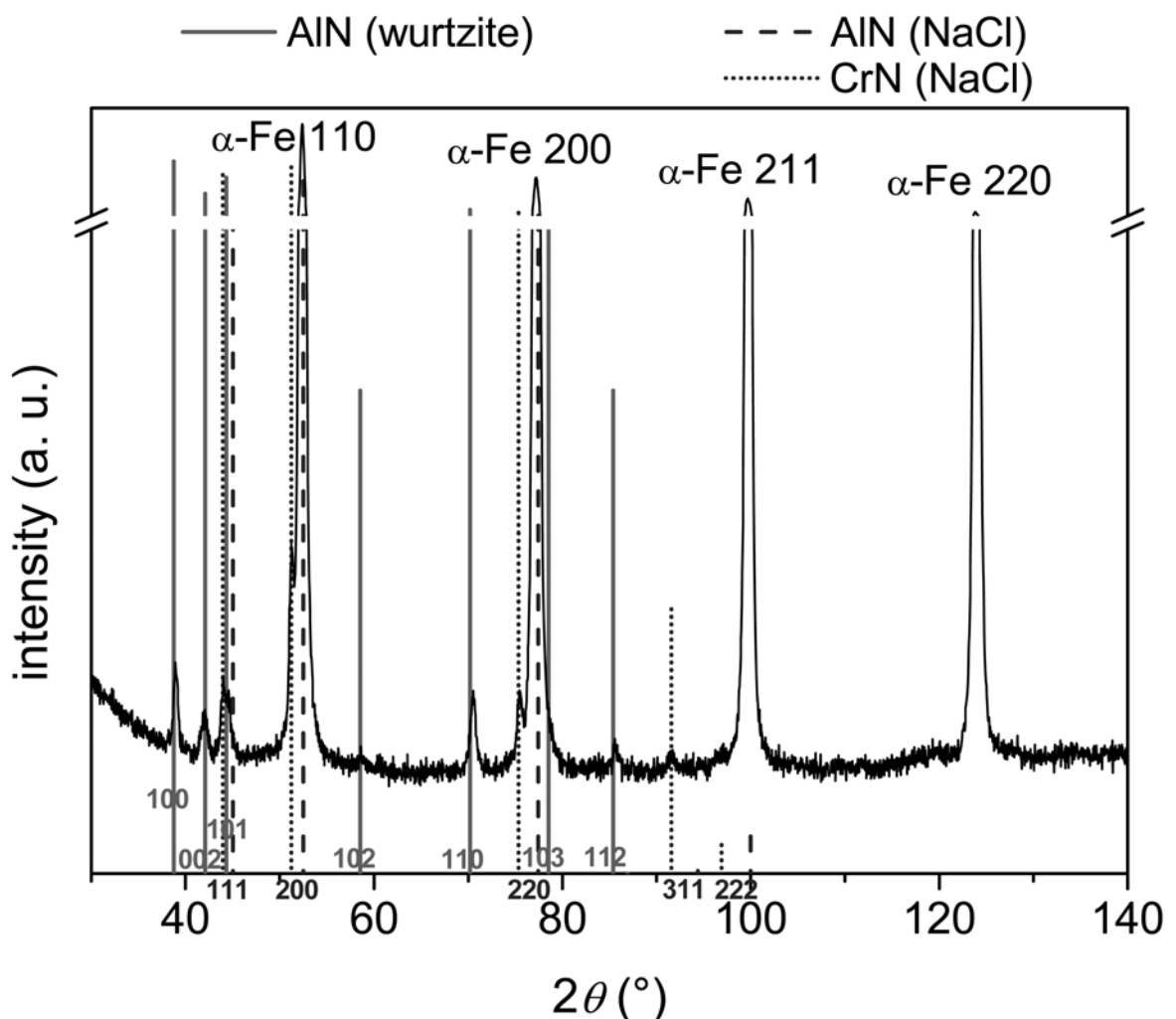


Fig. 3.10: X-ray diffractogram of the specimen centre (formerly unnitrided core, i.e. at about 500  $\mu\text{m}$  depth) for phase analysis after nitriding and annealing (counting time 120 s/step).

A BF image and the corresponding SADP (electron-beam axis:  $[001]_{\alpha\text{-Fe}}$ ) of an ion-milled TEM sample taken from the specimen centre are shown in Fig. 3.11. Besides

ferrite (and  $220_{\text{Fe}_3\text{O}_4}$ ; cf. section 3.2.3) spots, only AlN wurtzite structure type spots, indicating a Pitsch–Schrader OR of the precipitate with the ferrite matrix (cf. Fig. 3.1), can be observed in the SADP. The AlN precipitates in Fig. 3.11 appear bright in the ferritic matrix due to the considerable difference in atomic number of Al (precipitate) and Fe (matrix). The atomic numbers of Cr and Fe are not so different and hence a low contrast between chromium-rich precipitates and the ferrite matrix is expected: it is hardly possible to identify chromium-rich precipitates in Fig. 3.11.

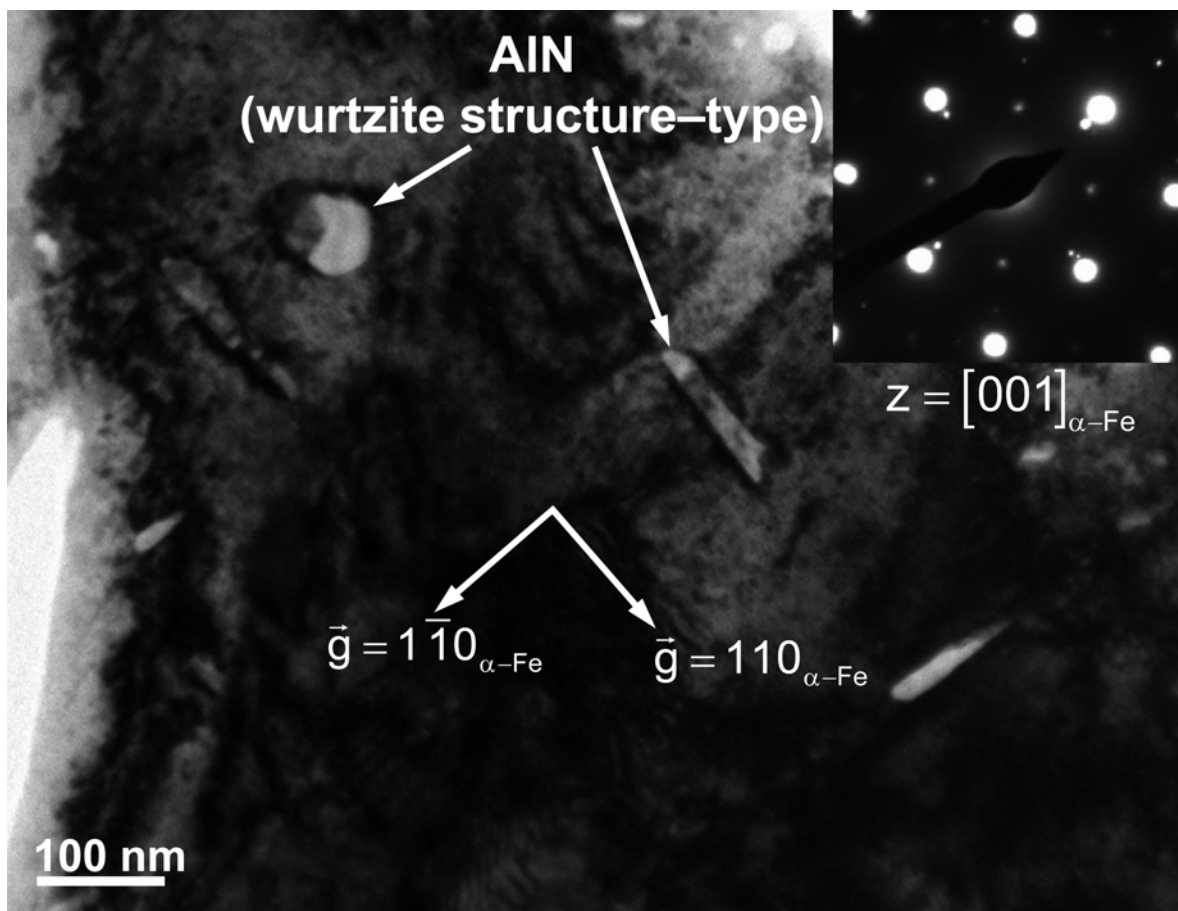


Fig. 3.11: BF image and corresponding SADP of an ion-milled TEM sample from a nitrided and annealed specimen taken at the specimen-centre area (initially the unnitrided core) showing coarse, wurtzite structure type precipitates, exhibiting a Pitsch–Schrader OR with the ferrite matrix (see SADP (inset; electron-beam axis:  $[001]_{\alpha\text{-Fe}}$ ) and cf. Fig. 3.1).

In order to characterise the precipitates by their chemical composition a STEM line-scan (EDX) was carried out across a bright precipitate (Figs. 3.12 a and b). In this bright particle only Al is detectable, but no Cr. Another STEM line-scan was carried out across a hardly visible precipitate (Figs. 3.12 c and d). In this precipitate only Cr is detectable, and not Al.

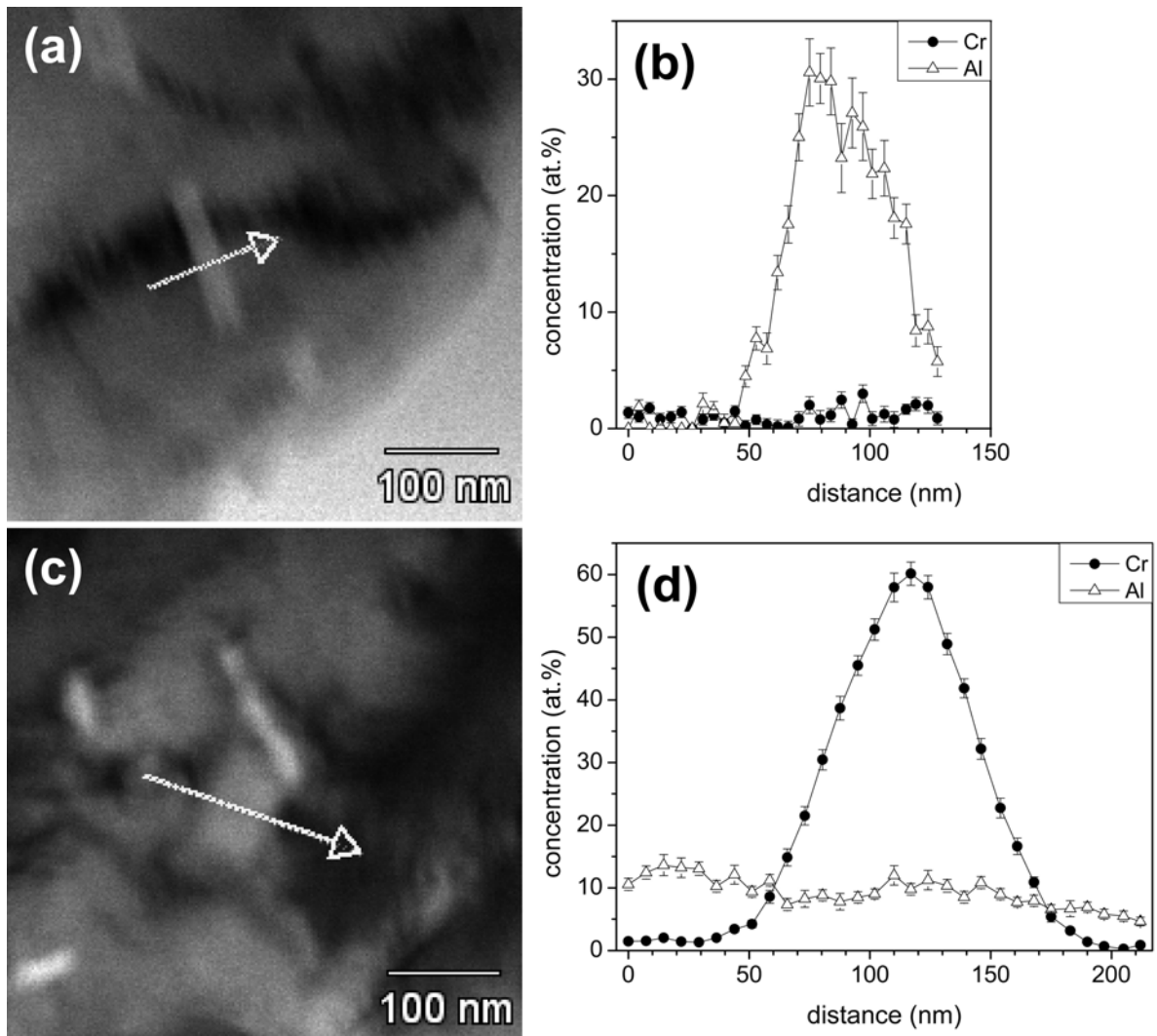


Fig. 3.12: (a) and (c) STEM BF images of an ion-milled TEM sample from a nitrided and annealed specimen taken at the specimen-centre area (initially the unnitrided core). (b) and (d) Results of the corresponding STEM line-scans (EDX; see arrows in Figs. 3.12 a and c). Figs. 3.12 a and b: only Al is detectable in the bright precipitate. Figs. 3.12 c and d: only Cr is detectable in the hardly visible precipitate.

A STEM BF image and EDX elemental maps for N-K, Al-K and Cr-K at this location are shown in Fig. 3.13. The aluminium-rich (also nitrogen-rich) areas can clearly be assigned to the bright (AlN) precipitates in the BF image. The chromium-rich area (also nitrogen-rich) cannot be assigned to a distinct contrast in the BF image: CrN precipitates are hardly visible in the BF images (see above).

From the above results it is concluded that the bright particles consist of the hexagonal, equilibrium AlN wurtzite structure type, whereas the dark, hardly visible particles consist of the cubic, equilibrium CrN rock-salt structure type. There is no indication for the presence of the mixed, metastable  $Cr_{1-x}Al_xN$  nitride as an intermediate precipitation stage.

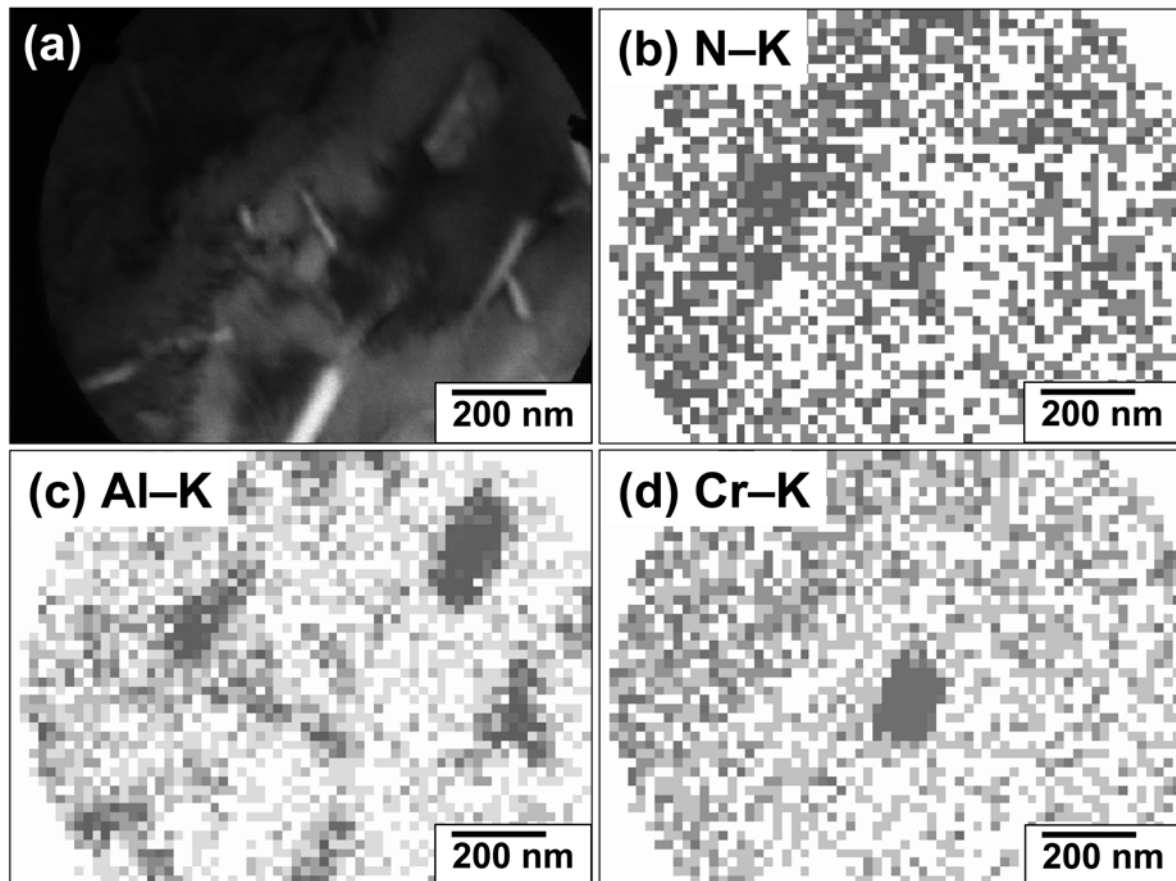


Fig. 3.13: (a) STEM BF image of an ion-milled sample from a nitrided and annealed specimen taken at the specimen-centre area (the formerly unnitrided core) and the results of element mapping for intensities of N–K, Al–K and Cr–K: (b), (c) and (d) respectively. The bright precipitates can clearly be interpreted as AlN, whereas the CrN precipitate is hardly visible in the BF image.

It follows that during annealing after nitriding in the originally unnitrided core relatively coarse (size 100 nm to 200 nm) hexagonal, wurtzite structure type AlN and cubic, rock-salt structure type CrN precipitates develop in the grain interiors; mixed  $\text{Cr}_{1-x}\text{Al}_x\text{N}$  precipitates are not observed.

### 3.4 Conclusions

- (i) Upon nitriding (here at 853 K) ferritic iron-based Fe–Cr–Al alloy, mixed, metastable cubic, rock-salt structure type  $\text{Cr}_{1-x}\text{Al}_x\text{N}$  nitrides develop in the nitrided zone, which contains considerably more nitrogen than necessary to precipitate all Cr and all Al: excess nitrogen.
- (ii) *In the nitrided zone*, annealing (here at 973 K) subsequent to nitriding leads to the development of the equilibrium precipitates CrN and AlN:

- Cubic, rock-salt structure type and hexagonal, wurtzite structure type particles occur after annealing, which exhibit a Bain-type orientation relationship and a Pitsch–Schrader orientation relationship, respectively, with the ferrite matrix, and which correspond with (compositional analysis) CrN and AlN, respectively. Part of the cubic, rock-salt structure type particles is (still) mixed Cr<sub>1-x</sub>Al<sub>x</sub>N nitride, however containing less Al than initially present.
- Transformation of the initial mixed Cr<sub>1-x</sub>Al<sub>x</sub>N nitrides proceeds by their Al depletion. The subsequent precipitation of AlN occurs in the interior and at grain boundaries of the matrix. A coarser microstructure results.
- The precipitates no longer exhibit strong coherency with the ferrite matrix, as reflected by the strong decrease of the broadening of the XRD ferrite-matrix reflections and the distinct decrease of hardness.

(iii) *In the originally unnitrided core*, annealing leads to the presence of nitrogen by diffusion of the mobile excess nitrogen from the nitrated zones. This nitrogen immediately precipitates as relatively coarse CrN at grain boundaries and as smaller (~100 nm to 200 nm) cubic, rock-salt structure type CrN and hexagonal, wurtzite structure type AlN in the interior of the grains. Mixed Cr<sub>1-x</sub>Al<sub>x</sub>N nitride does not develop.

## **Acknowledgements**

The authors wish to thank Mr. J. Köhler and Mr. P. Kress for assistance with the nitriding experiments, Mrs. S. Haug for assistance with the EPMA experiments, Mr. W.-D. Lang for TEM sample preparation, Mrs. M. Kelsch for assistance during the first stage of TEM experiments, Dr. F. Phillipp for assistance during the first stage of HRTEM experiments, Dr. W. Sigle for assistance during the STEM experiments, discussion and critical reading of the manuscript, and Dr. A. Leineweber for discussion.

## References

- [1] C. H. Knerr, T. C. Rose and J. H. Filkowski (1991). Gas nitriding. ASM Handbook: Heat Treating. J. R. Davis, G. M. Davidson, S. R. Lampman, T. B. Zorc, J. L. Daquila, A. W. Ronke, K. L. Henniger and R. C. Uhl. Metals Park, Ohio, ASM International. 4: 387-409.
- [2] E. J. Mittemeijer and J. Grosch, Eds. Proceedings of 'AWT-Tagung Nitrieren und Nitrocarburieren', Arbeitsgemeinschaft Wärmebehandlung und Werkstofftechnik e.V., Wiesbaden (1991).
- [3] D. Liedtke, U. Baudis, J. Boßlet, U. Huchel, H. Klümper-Westkamp, W. Lerche and H. J. Spies, Wärmebehandlung von Eisenwerkstoffen Nitrieren und Nitrocarburieren, Renningen, Expert Verlag (2006).
- [4] M. H. Biglari, C. M. Brakman and E. J. Mittemeijer, Philos. Mag. A 72 (1995) 1281-1299.
- [5] K. H. Jack, Proceedings of the conference on heat treatment 1973 (1975) 39-50.
- [6] E. J. Mittemeijer and J. T. Slycke, Surf. Eng. 12 (1996) 152-162.
- [7] E. J. Mittemeijer and M. A. J. Somers, Surf. Eng. 13 (1997) 483-497.
- [8] H. H. Podgurski and H. E. Knechtel, Trans. TMS-AIME 245 (1969) 1595-1602.
- [9] M. H. Biglari, C. M. Brakman, M. A. J. Somers, W. G. Sloof and E. J. Mittemeijer, Z. Metallk. 84 (1993) 124-131.
- [10] M. H. Biglari, C. M. Brakman, E. J. Mittemeijer and S. van der Zwaag, Metall. Mater. Trans. A 26 (1995) 765-776.
- [11] J. S. Steenaert, M. H. Biglari, C. M. Brakman, E. J. Mittemeijer and S. van der Zwaag, Z. Metallk. 86 (1995) 700-705.
- [12] M. Sennour and C. Esnouf, Acta Mater. 51 (2003) 943-957.
- [13] JCPDS-International Centre for Diffraction Data (2002), PCPDFWIN, Version 2.3.
- [14] E. C. Bain, Trans. AIME 70 (1924) 25-46.
- [15] R. G. Baker and J. Nutting, Iron and Steel Inst. Spec. Rep. 64 (1959) 1-22.
- [16] W. Pitsch and A. Schrader, Arch. Eisenhüttenw. 29 (1958) 715-721.



- [17] S. Chen and J. Morris, *Metall. Mater. Trans. A* 8 (1977) 19.
- [18] M. Sennour, P. H. Jouneau and C. Esnouf, *J. Mater. Sci.* 39 (2004) 4521.
- [19] S. S. Hosmani, R. E. Schacherl and E. J. Mittemeijer, *Acta Mater.* 54 (2006) 2783-2792.
- [20] P. M. Hekker, H. C. F. Rozendaal and E. J. Mittemeijer, *J. Mater. Sci.* 20 (1985) 718-729.
- [21] M. A. J. Somers, R. M. Lankreijer and E. J. Mittemeijer, *Philos. Mag. A* 59 (1989) 353-378.
- [22] M. H. Biglari, C. M. Brakman, E. J. Mittemeijer and S. van der Zwaag, *Philos. Mag. A* 72 (1995) 931-947.
- [23] N. E. Vives Diaz, S. S. Hosmani, R. E. Schacherl and E. J. Mittemeijer, *Acta Mater.* 56 (2008) 4137-4149.



## Chapter 4

# The microstructure of the diffusion zone of a gaseously nitrided Fe–1.5wt.%Cr–1.5wt.%Al alloy

*A. R. Clauss, E. Bischoff, R. E. Schacherl and E. J. Mittemeijer*

### Abstract

Gaseous nitriding experiments of an Fe–1.5wt.%Cr–1.5wt.%Al (i.e. Fe–1.6at.%Cr–3.1at.%Al) alloy were carried out as function of time at 853 K. The microstructure of the diffusion zone was characterised by microhardness, electron probe microanalysis (EPMA), X-ray diffraction analysis (XRD), scanning transmission electron microscopy (STEM) in combination with energy-dispersive X-ray spectroscopy (EDX) and Auger electron spectroscopy (AES). Chromium and aluminium precipitate together as a mixed  $\text{Cr}_{1-x}\text{Al}_x\text{N}$  phase in the diffusion zone. The size of the (semi)coherent precipitates and the amount of excess nitrogen have a strong influence on the microstructure of the diffusion zone. Crack formation occurs after a certain nitriding time starting from the specimen surface and propagating along grain boundaries more or less perpendicularly to the surface towards larger depth. The grain-boundary brittleness could be ascribed to the precipitation of excess nitrogen as nitrogen gas at the grain boundaries and to the segregation of Al at grain boundaries promoting precipitation of AlN at the grain boundaries. The residual stress-depth profile was determined and a simple model was proposed to explain the surprising initially occurrence of tensile stress parallel to the surface in the diffusion zone.

### 4.1 Introduction

Nitriding is used in industry as an important thermochemical surface engineering process to greatly improve the fatigue, wear and corrosion resistances of ferritic steel workpieces [1-3]. Nitriding is usually performed in a gaseous, ammonia containing atmosphere. The process leads to, in dependence on the nitriding conditions (i.e.

temperature, pressure and chemical potential of nitrogen in the gas atmosphere [4]), the formation of iron nitrides at the outer surface of the specimen (external nitriding), and the precipitation of alloying-element nitrides within the nitrated zone (diffusion zone) underneath the possible surface layer of iron nitrides (internal nitriding). Although gaseous nitriding allows an accurate adjustment of the chemical activity of dissolved nitrogen at the interface between the nitriding atmosphere and the specimen surface [4-6], the application practice in industry is still largely based on phenomenology, in particular due to the lack of fundamental knowledge on the nitriding of multicomponent, technical alloys. This contrasts with the level of understanding reached about the nitriding behaviour of simple *binary* iron-based alloys (e.g. see Refs. [7-10]).

Recently, the nitriding behaviour of a *ternary* Fe–1.5wt.%Cr–1.5wt.%Al (i.e. Fe–1.6at.%Cr–3.1at.%Al) alloy was investigated, since aluminium and chromium often occur simultaneously as alloying elements in typical nitriding steels. It was shown that Cr and Al precipitate together as metastable, mixed  $\text{Cr}_{1-x}\text{Al}_x\text{N}$  precipitates, of which the crystal structure (cubic, rock-salt structure type) and the morphology (platelet-like) and orientation relationship with the ferrite matrix (Bain-type) could be clarified (cf. chapter 2). Subsequent transformation of this initially metastable phase into the stable binary equilibrium nitrides, i.e. cubic CrN of rock-salt structure type and hexagonal AlN of wurtzite structure type was shown to occur upon annealing (cf. chapter 3).

In the course of this research project some peculiar observations were made, especially concerning crack formation along grain boundaries and characteristic contrast of bright and dark zones in light micrographs of etched specimen cross-sections after nitriding. The purpose of the present paper is to present an explanation of these phenomena, in terms of residual stress development, segregation effects and the occurrence of excess nitrogen. To this end a detailed microstructural characterisation of the microstructure of the diffusion zone was performed using X-ray diffraction analysis (XRD), electron probe microanalysis (EPMA), scanning transmission electron microscopy (STEM) and Auger electron spectroscopy (AES) techniques.

## 4.2 Experimental

### 4.2.1 Specimen preparation

An alloy of the composition Fe–1.5wt.%Cr–1.5wt.%Al (i.e. Fe–1.6at.%Cr–3.1at.%Al) was produced by weighing appropriate amounts of pure iron (99.98 wt.%), pure chromium (99.999 wt.%) and pure aluminium (99.999 wt.%). The mixture of coarse Al pieces and granules of Cr and Fe was first pre-molten to small cakes in an arc furnace and subsequently molten in an Al<sub>2</sub>O<sub>3</sub> crucible by means of an inductive furnace, in both cases under protective argon gas atmospheres (99.999 vol.%). The melt was cast in a copper mould to obtain a cylindrical rod ( $\varnothing$ : 10 mm, *l*: 100 mm). The chemical composition and the amounts of impurities were determined by chemical analysis. The chromium and aluminium concentrations were determined by inductively coupled plasma – optical emission spectroscopy, the nitrogen and oxygen contents were measured applying carrier gas hot extraction and the sulphur and carbon contents were determined by the combustion method. The results are shown in Table 4.1.

Table 4.1

Amounts of alloying elements and impurities of the used alloy (balance Fe)

Alloy	Cr		Al		N (wt.%)	O (wt.%)	S (wt.%)	C (wt.%)
	(wt.%)	(at.%)	(wt.%)	(at.%)				
Fe–Cr–Al	1.52 ± 0.02	1.60 ± 0.03	1.52 ± 0.02	3.09 ± 0.04	0.0010 ± 0.0003	0.0054 ± 0.0009	< 0.0010	0.0025 ± 0.0002

The homogeneity of the element distribution was validated by electron probe microanalysis line-scans (EPMA, cf. section 2.2.3.2) on a polished cross-section of the rod.

After cutting the rod in pieces, the shell of each piece was removed by grinding. Subsequently the pieces were cleaned, first with ethanol and finally with water in an ultrasonic bath, before they were cold rolled to sheets of a thickness of about 1 mm. Rectangular specimens (20 × 15 × 1 mm<sup>3</sup>) were cut out of the sheets and a little hole was drilled ( $\varnothing$ : 1.5 mm) in each specimen to hang it up in the nitriding facility. The specimen surfaces were ground, polished and cleaned first with ethanol and finally with water in an ultrasonic bath before encapsulation in a quartz tube under a protective argon gas atmosphere (99.999 vol.%). Subsequently the samples were

recrystallised in a muffle furnace for 1 h to 2 h at a temperature between 1073 K and 1123 K. The average grain diameter of the resulting, more or less equiaxed, single-phase microstructure was 27  $\mu\text{m}$ .

## 4.2.2 Nitriding

Before nitriding the specimen surface was polished (final step: 1  $\mu\text{m}$  diamond suspension), cleaned in an ultrasonic bath and dried in a nitrogen gas flow. The nitriding facility consists of a vertical multizone quartz-tube furnace ( $\varnothing$ : 28 mm) in which the nitriding process was performed in a  $\text{H}_2/\text{NH}_3$  gas mixture flux of 500 ml/min (purity  $\text{H}_2$ : 99.999 vol.%, purity  $\text{NH}_3$ : > 99.998 vol.%; linear gas velocity at room temperature: 13.5 mm/s) at a temperature of  $(853 \pm 1)$  K. Mass-flow controllers adjusted the gas fluxes (455 ml/min  $\text{H}_2$  and 45 ml/min  $\text{NH}_3$ ), which correspond to a nitriding potential of  $r_{\text{N}} = 0.104 \text{ atm}^{-1/2}$  (cf. Refs. [4, 6]). The nitriding process was interrupted by breaking mechanically the quartz fibre, at which the specimen was suspended in the facility, so that the specimen fell through an opened valve into a bottle where the specimen was quenched in water. Under the chosen nitriding potential the formation of iron nitrides in pure iron is not possible [6], i.e. the nitrated layer consists only of the diffusion zone with precipitated alloying element nitrides (internal nitriding; cf. section 4.1).

## 4.2.3 Specimen characterisation

### 4.2.3.1 X-ray diffractometry

Phase analysis via X-ray diffraction applied to all specimens before nitriding, after nitriding and after uncovering deeper areas of the nitrated zone by removing material from the surface (cf. section 4.2.4) was performed on a PANalytical (formerly Philips) X'Pert Multi-Purpose Diffractometer (MPD) in Bragg-Brentano geometry, which was equipped with a graphite diffracted beam monochromator set to  $\text{Co-K}\alpha$  radiation. For better crystallite statistics, the specimens were rotated on a spinner around their vertical axis during each measurement. The range of the diffraction angle ( $30^\circ \leq 2\theta \leq 140^\circ$ ) was scanned in steps of  $0.05^\circ$  with a counting time of 10 s per step.

The identification of phases from the  $2\theta$  positions of the XRD reflections was carried out by means of data from the ICDD data base [11].

#### *4.2.3.2 Electron probe microanalysis (EPMA)*

The determination of concentration depth profiles was performed by EPMA on polished specimen cross-sections embedded in Struers PolyFast (final step: 1  $\mu\text{m}$  diamond suspension). For this purpose a Cameca SX100 microprobe (acceleration voltage  $U_a = 15$  kV, current  $I = 100$  nA, spot size about 1  $\mu\text{m}$ ) was used equipped with five wavelength-dispersive spectrometers. At least four different line-scans across the specimen cross-sections, with step sizes from 1  $\mu\text{m}$  to 3  $\mu\text{m}$ , were performed perpendicular to the nitrided zone, starting from the surface towards the centre of the specimen. For determination of the element contents at each measurement point, the intensities of the characteristic Fe–K $\beta$ , Cr–K $\alpha$ , Al–K $\alpha$  and N–K $\alpha$  X-ray emission peaks were measured and divided by the corresponding intensities obtained from standard samples of pure Fe, Cr, Al and  $\gamma$ -Fe $_4$ N (for N–K $\alpha$ ). Elemental concentrations were calculated from the intensity ratios applying the  $\Phi(\rho z)$  approach according to Pouchou and Pichoir [12].

#### *4.2.3.3 Light microscopy (LM)*

For LM investigations on specimen cross-sections, pieces of nitrided specimens were cut off (Struers Accutom–50, Al $_2$ O $_3$  cut-off wheel), embedded in Struers PolyFast, ground and polished (last polishing step: 1  $\mu\text{m}$  diamond suspension). Each cross-section was etched with 0.5 % Nital (i.e. 0.5 vol.% HNO $_3$  in ethanol) at a temperature of about 293 K for about 30 s to 90 s. LM micrographs were taken using a Zeiss Axiophot microscope equipped with a digital camera (Olympus ColorView IIIu).

#### *4.2.3.4 Microhardness measurement (Vickers hardness)*

Microhardness measurements on cross-sections of nitrided specimens were carried out with a Vickers microhardness tester (Leica VMHT Mot) applying loads between 49 mN (determination of microhardness profiles across single grains; see section 7) and 490 mN (determination of microhardness depth profiles across specimen cross-sections; see section 3), an indenter speed of 30  $\mu\text{m/s}$  and a dwell time of 10 s. The

distances of the indentations on the cross-sections from the specimen surface and the lengths of indentation diagonals were measured with the microhardness tester or on calibrated LM micrographs applying computer software (analySIS Imaging–Software).

#### 4.2.4 Determination of the residual stress depth profile by X-ray diffractometry

To determine the residual stress depth profile alternating XRD stress measurements, using the  $\sin^2\psi$  method [13-15], and removals of a surface layer with a certain thickness were performed. The XRD  $\sin^2\psi$  method for stress measurement was performed at a constant penetration depth of 0.5  $\mu\text{m}$  (i.e. the penetration depth of the X-rays was constant for variable  $\psi$ , for details of this method see Ref. [16]). The surface layers were removed mechanically layer by layer from the original specimen surface, by controlled polishing to exhibit deeper areas of the nitrated zone, to allow X-ray stress determination of the occurring surfaces. The procedure of polishing and the way of evaluating the results is described in detail in Ref. [17]. The stress relaxation due to removal of material was corrected for by the same method as described in Appendix A of Ref. [17].

Lattice strains were calculated from the peak position of the  $\alpha\text{-Fe}$  211 reflection in dependence on the tilt angle  $\psi$ . The measurements were performed on a Bruker AXS D8 Discover diffractometer equipped with a quasi-parallel beam geometry,  $\text{Cu-K}\alpha$  radiation, an Eulerian cradle and an energy-dispersive detector. The range of the diffraction angle ( $76^\circ \leq 2\theta \leq 88^\circ$ ) was scanned in steps of  $0.06^\circ$  with a counting time of 40 s per step. The change of the tilt angle  $\psi$  from  $34^\circ$  to  $68^\circ$  in steps of  $2^\circ$  yields 18 points in the  $\sin^2\psi$  plot [15]. It was confirmed that the results do not depend on  $\varphi$  (i.e. the rotation angle around the specimen surface normal): a plane state of stress prevails. Therefore the specimen was rotated on a spinner around its vertical axis during each residual stress measurement to improve crystallite statistics. The specimen texture also did not depend on  $\varphi$ : pole figures were recorded before and after nitriding on a PANalytical Materials–Research Diffractometer (MRD) equipped with a quasi-parallel beam geometry, an Eulerian cradle and a graphite diffracted beam monochromator set to  $\text{Co-K}\alpha$  radiation. The obtained pole figures show a weak texture that is rotationally symmetric with respect to the specimen surface normal.



The measured line profiles of the  $\alpha$ -Fe 211 reflection were evaluated by fitting split Pearson VII functions using a custom peak fit program. Besides other fit parameters (e.g. full width at half maximum, shape parameter and asymmetry parameter) the program refines the position of the peak maximum and provides corresponding error estimates. The lattice spacings  $d_{\alpha\text{-Fe } 211}$  were calculated from the peak positions using the Bragg equation. The calculated lattice spacings were plotted against  $\sin^2 \psi$ , yielding straight lines within experimental accuracy. The residual stress values were calculated from the slopes of these straight lines according to Refs. [15] and [17], for the case of a macroscopically elastically isotropic specimen with a plane, rotationally symmetric biaxial stress state at the investigated surface (see above).

#### **4.2.5 Scanning transmission electron microscopy (STEM)**

Scanning transmission electron microscopy (STEM) was employed to investigate the elemental distribution at and near to grain boundaries at different selected depths in nitrided specimens. Appropriate STEM specimens were produced by the argon ion milling technique using special titanium specimen carrier (for details see chapter 2). The investigation was performed in a VG HB 501UX scanning transmission electron microscope operating at 100 kV with a focused beam of less than 1 nm size and a NORAN EDX system (multi-channel analyser; 10 eV per channel) for energy dispersive X-ray spectroscopy (EDX). The element composition at and near to grain boundaries was determined by line-scans conducted across the grain boundaries. For each line-scan 30 to 50 points were measured with a dwell time of 5 s per point (evaluation software: NORAN System SIX).

#### **4.2.6 Auger electron spectroscopy (AES)**

Auger electron spectroscopy (AES) was performed to investigate the fracture surface of a nitrided specimen and to determine sputter depth profiles for different fracture sites. For this purpose a through-nitrided foil was broken in the scanning Auger microscope (JEOL JAMP-7830F operating at 10 kV and 15 nA to 70 nA) under ultra-high vacuum (UHV:  $p = 2.5 \cdot 10^{-8}$  Pa). AES analysis was carried out on selected points at different fracture sites employing a focused electron beam with a diameter of about 30 nm. Qualitative elemental concentration depth profiles were determined by

sputtering and measuring alternately. Sputtering was performed, using an  $\text{Ar}^+$  ion beam (0.5 keV) rastering over an area of about  $300 \times 300 \mu\text{m}^2$ .

### 4.3 Phase analysis and ferrite-matrix lattice strains

X-ray diffractograms were recorded from the specimen surfaces. No separate phases were detected at the surface, both before and after nitriding, except the ferrite phase. However, the ferrite reflections had broadened very strongly after nitriding due to the precipitation of tiny, coherent  $\text{Cr}_{1-x}\text{Al}_x\text{N}$  precipitates, which diffract coherently with the immediately surrounding, strained ferrite matrix (cf. chapter 2; see further section 4).

### 4.4 Development of nitrogen concentration- and microhardness-depth profiles

The elemental distributions on cross-sections of several specimens, nitrided for 0.25 h, 1 h, 2 h, 5 h, 7 h and 15 h at 853 K, were determined by EPMA. The N concentration-depth profiles, for each specimen obtained from several different line-scans perpendicular to the surface, have been superposed graphically in Fig. 4.1. The distributions of Al and Cr remained, after nitriding, homogeneous at levels of 3.1 at.% and 1.6 at.%, respectively, and have not been depicted in Fig. 4.1.

The N concentration-depth profiles are characterised by three areas: (i) an area near the surface (0  $\mu\text{m}$  to about 50  $\mu\text{m}$  depth, independent of nitriding time), where the maximum N concentration decreases strongly towards larger depth, (ii) a subsequent more or less plateau-like N profile with a modest negative slope (width of plateau depends on the nitriding time) and (iii) a transition zone between nitrided layer and unnitrided core where the N concentration drops to zero. At some locations in the EPMA line-scans the electron beam hits single pores, which cause a seeming concentration increase of light elements as N and Al since the physical assumptions used in the quantitative evaluation of the element concentrations (absorption and atomic number correction) are not fulfilled near pores [12]. For this reason some

points in the characteristic course, particularly of the N concentration-depth profiles, scatter.

The nitrogen uptake and the formation of nitride precipitates starts immediately upon the start of nitriding (cf. the nitrogen concentration-depth profile and the microhardness-depth profile after 0.25 h nitriding time in Figs. 4.1 and 4.2 a, respectively). The expected amount of “normal” nitrogen  $[N]_{\text{normal}} = 4.74 \text{ at.}\%$  (i.e. the sum of  $[N]_{(\text{Cr, Al})\text{N}}$ , which corresponds to precipitation of all substitutionally dissolved Al and Cr as  $\text{Cr}_{1-x}\text{Al}_x\text{N}$  precipitates, and  $[N]_{\alpha\text{-Fe}}^0$ , which is interstitially dissolved nitrogen in the remaining pure, unstrained ferrite matrix in thermodynamic equilibrium at the applied nitriding conditions<sup>6</sup>) has been indicated by the dashed horizontal line ( $[N]_{\text{normal}} = [N]_{(\text{Cr, Al})\text{N}} + [N]_{\alpha\text{-Fe}}^0$ ) in Fig. 4.1. The difference of the actually incorporated amount of N and the value represented by  $[N]_{\text{normal}}$  is called “*excess nitrogen*” [19-21]. Evidently, the nitrided specimens take up a huge amount of excess nitrogen, in particular near the surface. The amount of excess nitrogen in the surface-adjacent region does not decrease noticeably with increasing nitriding time (cf. Fig. 4.1 b).

The microhardness-depth profiles can be compared with the N concentration-depth profiles for 0.25 h, 1 h, 2 h and 5 h nitriding time in Fig. 4.2, both superimposed on the corresponding LM micrographs taken from the etched cross-sections. It follows that in the bright zone of the nitrided layer, which forms immediately, the amount of excess nitrogen is significantly larger than in the darker zone below, which starts to form after 1 h nitriding time (see also Fig. 4.5). The bright zone adjacent to the surface has a constant thickness of about 50  $\mu\text{m}$ . The width of the darker zone below depends on the nitriding time. The microhardness ranges from about 120 HV 0.05/10 in the unnitrided core to about 1330 HV 0.05/10 at the nitrided surface. The shape of the microhardness-depth profiles resembles roughly the shape of the N concentration-depth profiles, except in the dark zone, where a certain scattering of microhardness

---

<sup>6</sup> The value  $[N]_{\alpha\text{-Fe}}^0 = 0.30 \text{ at.}\%$  was experimentally determined under similar conditions as applied to the nitriding of the ternary Fe–Cr–Al alloy, by nitriding a pure ferrite foil [18].

values can be recognised (cf. Fig. 4.2 d). This scattering is related to an inhomogeneous N distribution in the interior of grains (cf. elemental segregation at grain boundaries discussed in section 4).

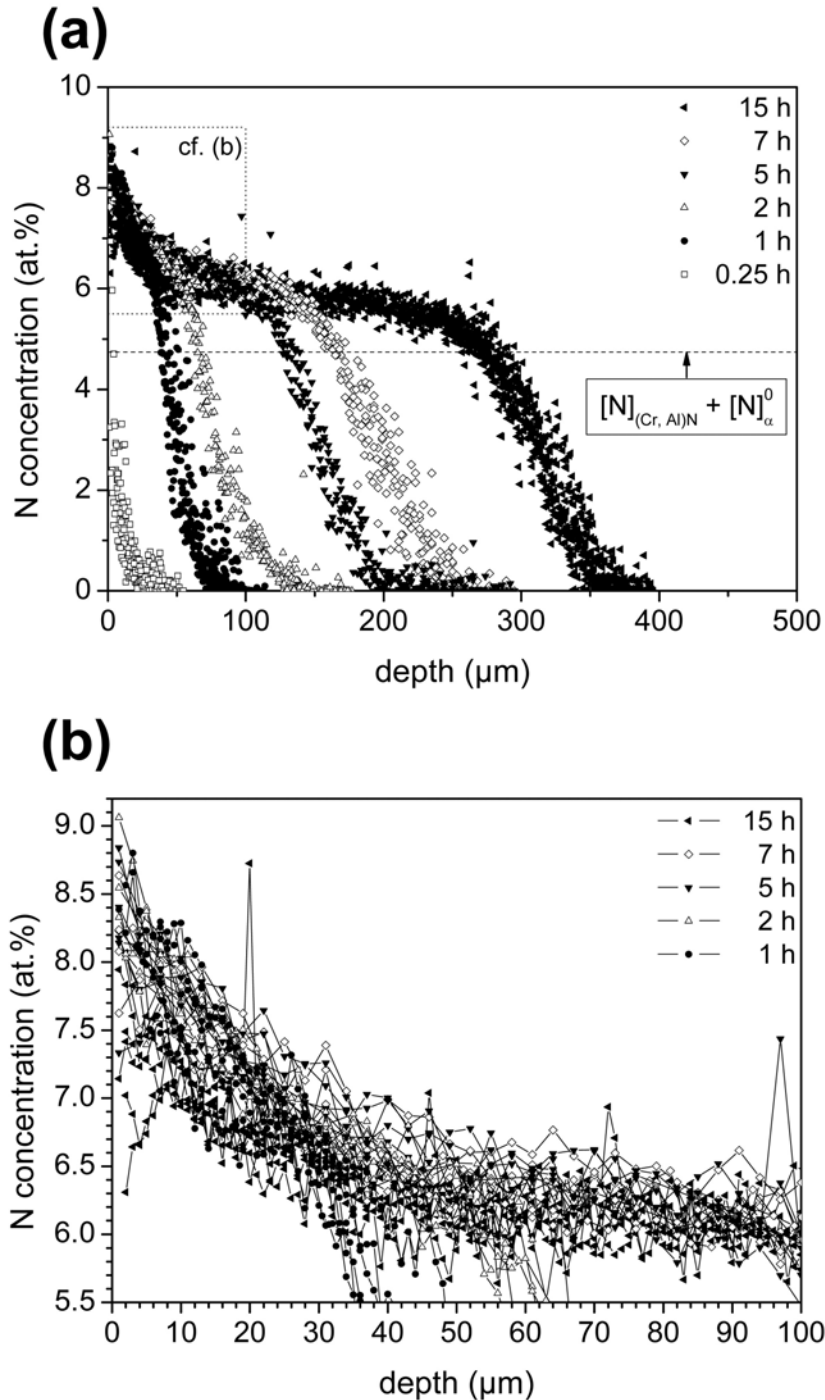


Fig. 4.1: (a) EPMA nitrogen concentration-depth profiles of several specimens nitrided for 0.25 h, 1 h, 2 h, 5 h, 7 h and 15 h at 853 K. The dashed horizontal line denotes the normal amount of N (i.e.  $[N]_{\text{normal}}$ ), which is necessary to transform all alloying elements into nitrides (i.e.  $[N]_{(Cr, Al)N}$ ) plus the amount of N, which can be dissolved interstitially in the unstrained ferrite matrix (i.e.  $[N]_{\alpha-Fe}^0$ ). (b) Enlargement of the surface adjacent region in Fig. 4.1 a.

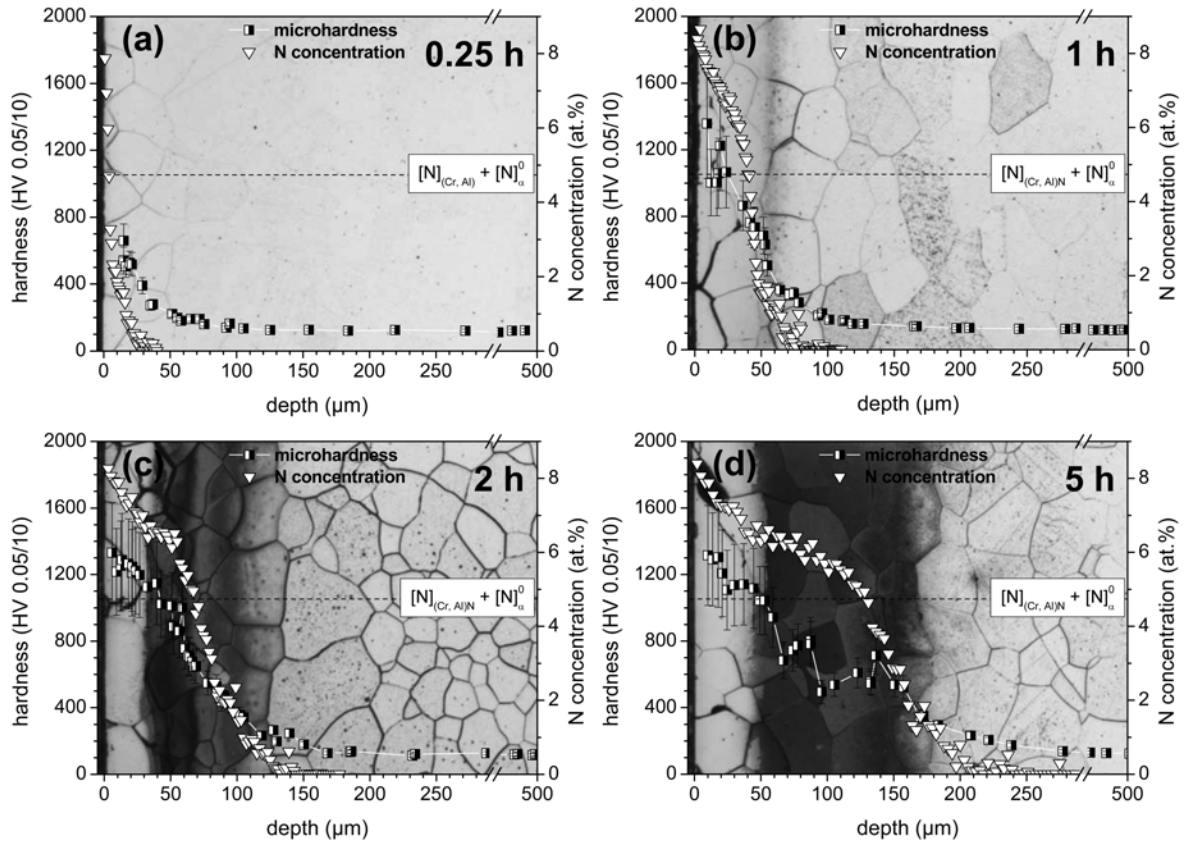


Fig. 4.2: Microhardness and N concentration depth profiles of nitrated specimens (a) 0.25 h, (b) 1 h, (c) 2 h and (d) 5 h at 853 K combined with the corresponding LM micrographs (only one representative EPMA line-scan is depicted each).

The high amount of excess nitrogen in the bright, surface adjacent zone can be explained considering the size of the nitride precipitates and their degree of coherency with the matrix. The precipitates in the bright zone are significantly finer than in the deeper, darker zone, as shown in chapter 2: The precipitate platelets near the surface of the nitrated zone (i.e. in the bright zone; cf. Fig. 4.2 d) have a length of 10 nm and smaller and a thickness of about 1 nm; at larger depths (i.e. in the dark zone; cf. Fig. 4.2 d) the precipitates are coarser: their length is about 100 nm and their thickness is up to 10 nm. The reason for this depth gradient in precipitate size is the dependence of nitrogen supersaturation on depth in the ferrite matrix upon nitriding; the supersaturation is higher near the specimen surface than at larger depths of the nitrated zone. Hence, the driving force for nitride precipitation is higher near the surface than deeper in the nitrated zone and accordingly a higher nitride-nucleus density can occur near the surface. A high nitride-nucleus density corresponds with the precipitation of more tiny, coherent, platelet-like nitride precipitates, as compared to a smaller nucleus

density as prevails at larger depths (cf. chapter 2; see also results and discussion in section 3).

Now, if the misfit between nitride precipitate and matrix is accommodated fully elastically, as can be expected for fine, coherent precipitates, the most pronounced state of misfit stress will occur (in the matrix). This elastic accommodation of misfit leads to enhanced solubility of interstitially dissolved N in the ferrite matrix (so-called mobile excess N) and to the adsorption of excess N at the nitride-platelet/ferrite-matrix interface (so-called immobile excess N); see discussion in Ref. [21]. Hence, near the surface, where the most fine, coherent nitride platelets occur, the highest amounts of (mobile and immobile) excess N can be expected, as observed (Fig. 4.1).

The attack by the etching solvent is apparently stronger in the dark zone (coarser precipitates) than in the bright surface adjacent region (finest precipitates) and in the unnitrided core (no precipitates). This can be explained as follows. In the unnitrided core a protective chromium- and aluminium-oxide layer prevents an attack of the ferrite matrix underneath and hence the unnitrided core appears bright in the etched cross-sections (cf. Fig. 4.2 a). The strong attack by the etchant in the dark zone is then due to the depletion of Al and Cr in the ferrite matrix due to their precipitation as nitride (cf. Figs. 4.2 c and d). In the bright zone, adjacent to the surface, the tiny, coherent  $\text{Cr}_{1-x}\text{Al}_x\text{N}$  nitrides are distributed homogeneously in the ferrite matrix. The strongly coherent nature of the precipitate/matrix assembly in this region (precipitate-platelet size: about  $10 \text{ nm} \times 1 \text{ nm}$ ; see above) provides a high, homogeneous, chemical resistivity and thus the etching effect is less pronounced than in the less coherent, less homogeneous dark zone underneath (precipitate-platelet size: about  $100 \text{ nm} \times 10 \text{ nm}$ ; see above).

## 4.5 Residual stress-depth profile

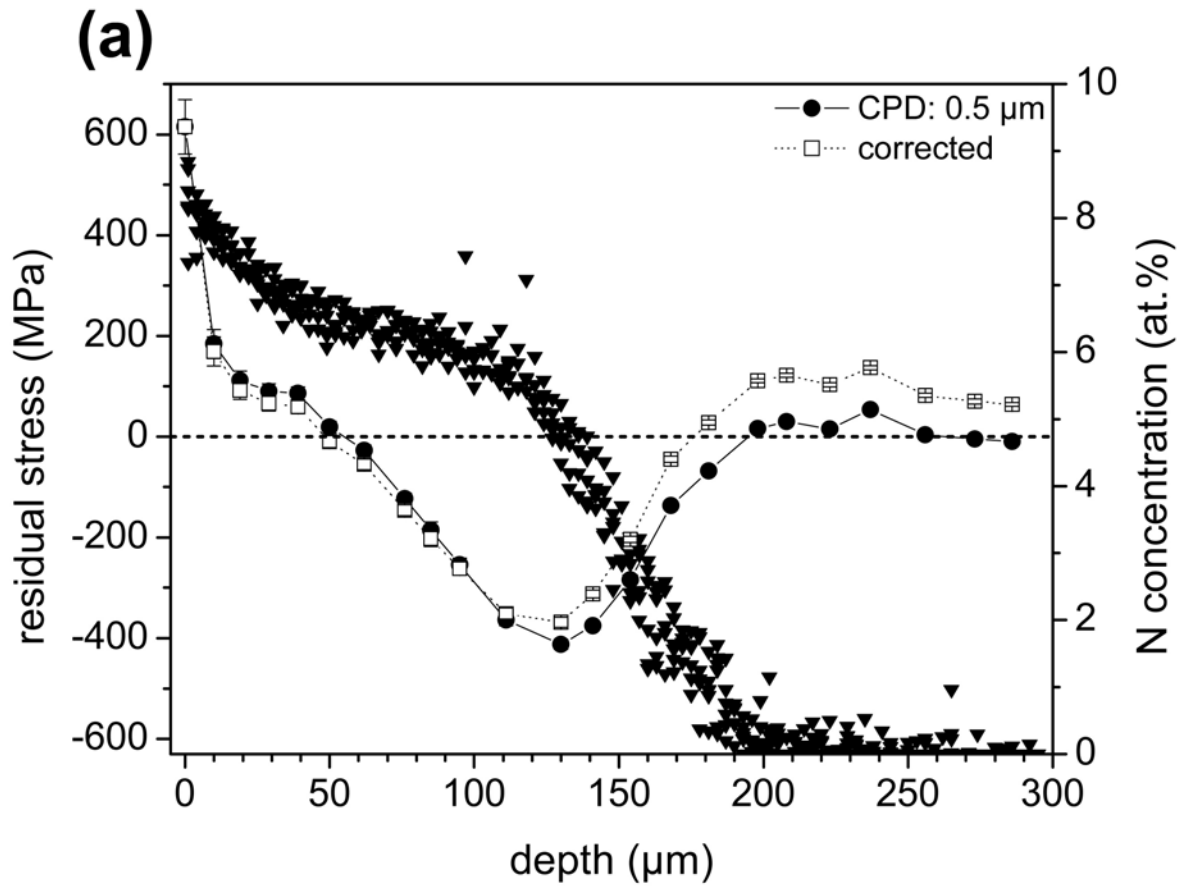
The residual (macro)stress-depth profile of a specimen nitrided for 5 h at 853 K is shown in Fig. 4.3 a together with the corresponding N concentration-depth profile as obtained from several, different EPMA line-scans; a LM micrograph of the cross-section is shown in Fig. 4.3 b. Near the surface the residual stress-depth profile shows a large tensile stress parallel to the surface of about 600 MPa. The tensile stress

decreases pronouncedly with increasing depth. At the transition of the bright and dark etching regions, the stress is about zero. In the dark etching region (beyond 50  $\mu\text{m}$  depth), the stress becomes distinctly compressive. The maximum compressive stress, about -400 MPa, is reached at a depth of about 130  $\mu\text{m}$ . Subsequently the compressive stress decreases with increasing depth until a more or less constant stress of small tensile value occurs in the region of the unnitrided core adjacent to the nitrided zone.

To understand the measured residual stress depth profile the following model is proposed:

(a) During the first stage of nitriding  $\text{Cr}_{1-x}\text{Al}_x\text{N}$  precipitates as coherent, submicroscopical particles. Due to the mismatch of the lattices of ferrite and  $\text{Cr}_{1-x}\text{Al}_x\text{N}$ , the precipitation of the nitride particles tends to expand (laterally) the nitrided zone, which is opposed by the unnitrided core, and as a result a compressive residual stress, parallel to the surface, is generated in the nitrided zone (mechanical equilibrium requires the simultaneous occurrence of a small tensile stress in the (large) unnitrided core; see Fig. 4.4 a).

(b) Upon continued nitriding the compressive stress reaches such a high value that plastic deformation (accommodation of the precipitate/matrix misfit; e.g. by creep) is induced. This will first happen in the surface adjacent region where the highest compressive stress level would be induced, in accordance with the nitrogen concentration-depth profile. This leads to relaxation of stress. This relaxation can be most pronounced near the surface also because there expansion perpendicular to the “free” surface can occur, implying that moderate levels of compressive stress can be maintained at some depth below the surface. Then, upon continued nitriding, coherent, submicroscopical  $\text{Cr}_{1-x}\text{Al}_x\text{N}$  particles are formed at larger depths beneath the surface (see Fig. 4.4 b), i.e. at the transition between nitrided zone and unnitrided core. Consequently, compressive stress develops in this region, as explained in (a). Then, as a consequence of the requirement of mechanical equilibrium of the specimen (cf. Fig. 4.4 b): (i) a tensile stress contribution is generated in the surface adjacent region of the nitrided zone, and (ii) a (small) tensile stress arises in the (large) unnitrided core near the transition between nitrided zone and unnitrided core.



**(b)**

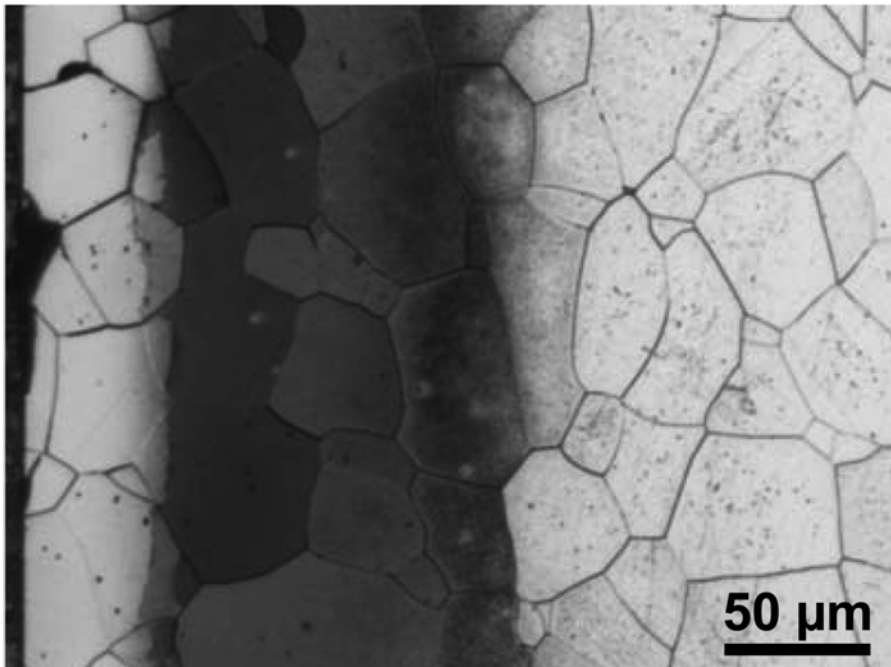


Fig. 4.3: (a) Residual stress-depth profile as measured at constant penetration depth (CPD = 0.5  $\mu\text{m}$ ) and as after the corresponding calculated correction for stress relaxation due to sublayer removal (for details see appendix A of Ref. [17]), together with the N concentration-depth profile of the nitrided specimen (5 h at 853 K). (b) LM micrograph of the corresponding cross-section (etched with 0.5 vol%  $\text{HNO}_3$  in ethanol at room temperature for about 60 s).



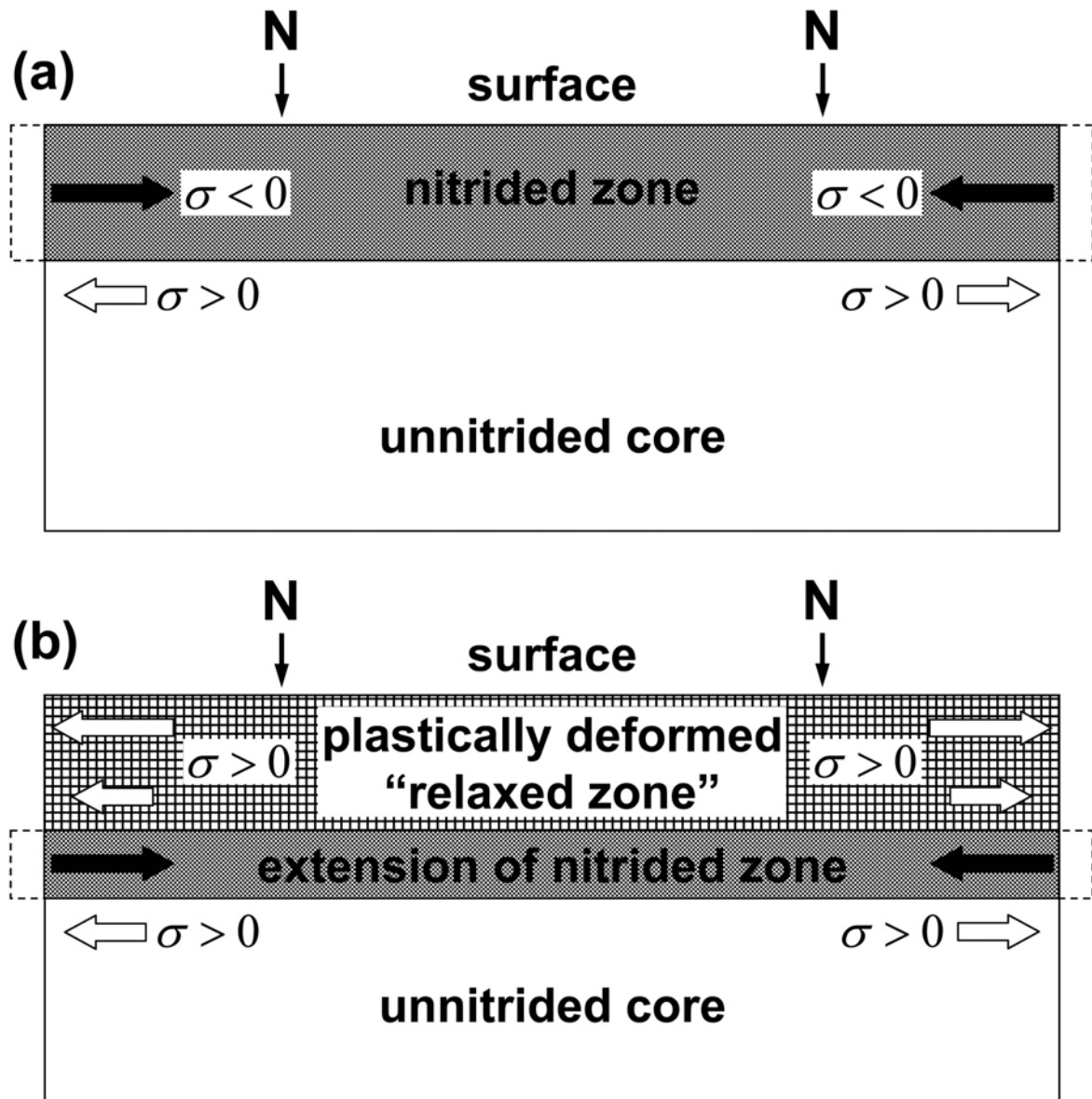


Fig. 4.4: Schematic illustration of the stress development during nitriding of Fe–1.5wt.%Cr–1.5wt.%Al. An initial compressive stress parallel to the surface occurs in the nitrided zone at the surface (a), which upon continued nitriding relaxes by plastic deformation and becomes tensile as a consequence of compressive stress build up in a newly nitrided, deeper layer of the specimen (b).

## 4.6 Crack formation

The LM micrographs taken from the cross-sections of four specimens, nitrided for 0.25 h, 1 h, 2 h and 5 h at 853 K, respectively, show the formation of “open” grain boundaries (already after 0.25 h nitriding time) and crack formation (starting between 2 h and 5 h nitriding time), in directions more or less perpendicular to the surface (see Fig. 4.5). The open grain boundaries can be due to the precipitation of excess nitrogen as  $N_2$  gas in pores, which coalesce at grain boundaries [4, 19], as well as a

consequence of Al segregation at grain boundaries, already before nitriding, leading to hexagonal AlN precipitation at these grain boundaries during nitriding (cf. section 8), which weakens the structural cohesion at grain boundaries due to the large volume misfit between nitride and ferrite. The growth of the cracks, initiated as open grain boundaries at the surface, from the surface and preferentially along grain boundaries more or less perpendicular to the surface (cf. arrows in Fig. 4.5) is obviously promoted by the development of residual tensile stress parallel to the surface in the surface adjacent region of the nitrided zone upon prolonged nitriding (cf. section 4.5 and Fig. 4.4 b).

The microscopical appearance of the microstructure in Fig. 4.5 is influenced by the embedding procedure, during which a load pressure of about 30 MPa is exerted on the specimen. This pressure may distort the brittle, (partly) open grain boundaries.

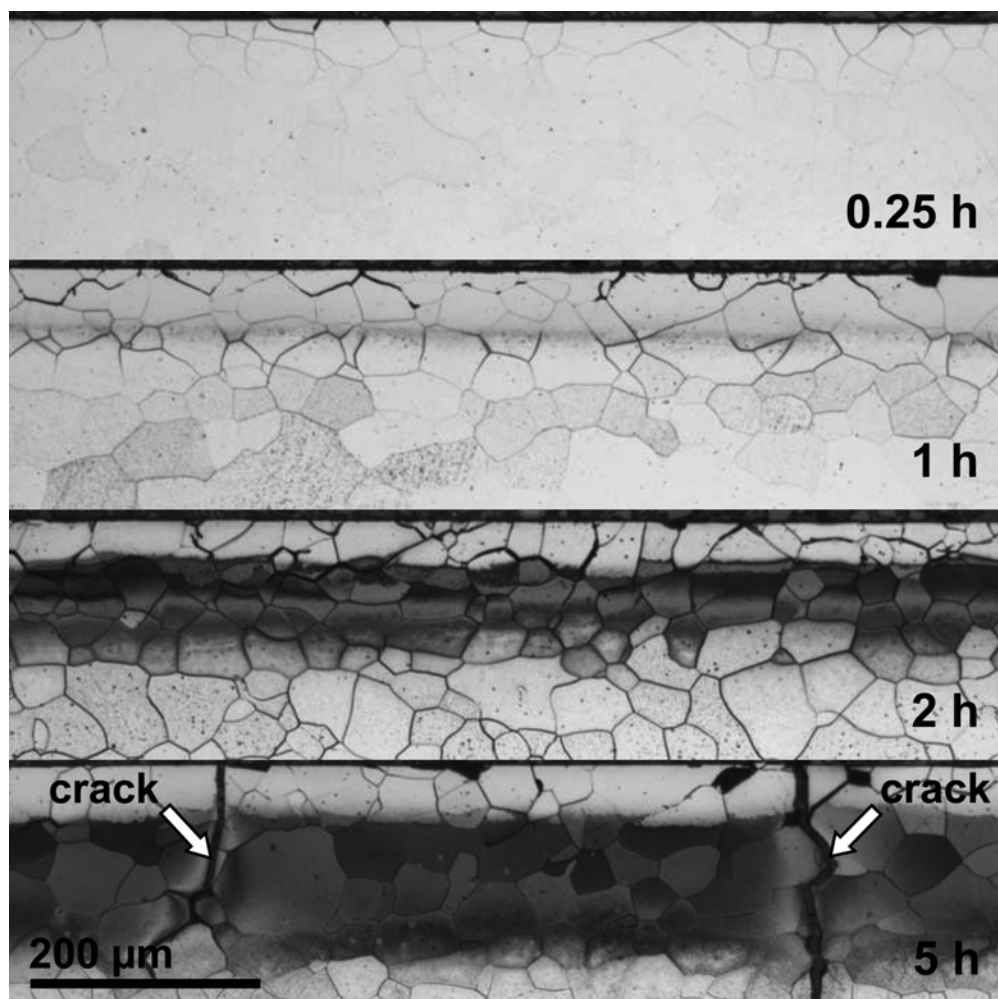


Fig. 4.5: LM micrographs taken from cross-sections (etched with 0.5 vol%  $\text{HNO}_3$  in ethanol at room temperature for about 60 s) of four specimens, nitrided for 0.25 h, 1 h, 2 h and 5 h at 853 K. The specimen surfaces are on the top of each micrograph (cf. transition between black embedding material and cross-section). Crack formation starts between 2 h and 5 h nitriding time.

## 4.7 Ferrite-matrix lattice strains

XRD measurements were carried out not only at the surface of a nitrided specimen (5 h at 853 K) but also after removing several layers of material (cf. section 4.5). Again (cf. section 4.3), no reflections are visible in the X-ray diffractograms recorded within the nitrided zone other than the (strongly) broadened ferrite reflections. For determination of the full width at half maximum (FWHM) of the only structurally broadened line profiles the instrumental resolution was determined on the basis of the X-ray diffractogram recorded from an unnitrided specimen. The structural line broadening of the nitrided specimen was determined by convoluting the instrumental broadening by a split pseudo-Voigt function for each of the four ferrite reflections under refinement of the FWHM, the asymmetry parameter  $A$  and the mixing parameter  $\eta$  respectively (software: Topas Bruker AXS). The dependence of the FWHM of the ferrite peaks as a function of depth in the nitrided zone is shown in Fig. 4.6 a. The FWHM has its maximum at the surface. It decreases strongly within the first 50  $\mu\text{m}$  of layer depth (cf. bright zone in LM micrographs shown in Figs. 4.2, 4.3 and 4.5). The nitride precipitates in the ferrite matrix obey the Bain-type orientation relationship with  $\{001\}_{\alpha\text{-Fe}}$ -type habit planes (cf. chapter 2). The misfit-strain field in ferrite is strongly tetragonally anisotropic [22] and thus it can be understood that the broadening of the  $\alpha\text{-Fe}$  200 reflection in the nitrided zone is particularly pronounced. Beyond 50  $\mu\text{m}$  layer depth the FWHM is much smaller; this is the region of coarser nitride precipitates (cf. section 4.4) associated with less pronounced misfit-strain development (only partial elastic accommodation of nitride/matrix misfit).

The  $\alpha\text{-Fe}$  200 diffraction-line profile taken from the nitrided surface is presented in Fig. 4.6 b together with the  $\alpha\text{-Fe}$  200 diffraction-line profile taken from the unnitrided surface. The strongly broadened line profile after nitriding can be interpreted as the superposition of two line profiles (cf. Ref. [22]): (i) the first line profile is due to the coherent diffraction of the tetragonally distorted ferrite matrix surrounding the  $\text{Cr}_{1-x}\text{Al}_x\text{N}$  particle and the  $\text{Cr}_{1-x}\text{Al}_x\text{N}$  particle, and (ii) the second line profile is due to the undistorted ferrite matrix. Therefore the overall reflection denoted by  $\alpha\text{-Fe}$  200 until now, could better be indicated as “ $\alpha\text{-Fe}$ ” 200. The anisotropic, tetragonal deformation of nitride particle and its surrounding ferrite matrix implies that the first

line profile presents itself as a tetragonal doublet in the X-ray diffractogram, revealed by an enhanced intensity at the low-angle side of the overall “ $\alpha$ -Fe” 200 reflection in Fig. 4.6 b.

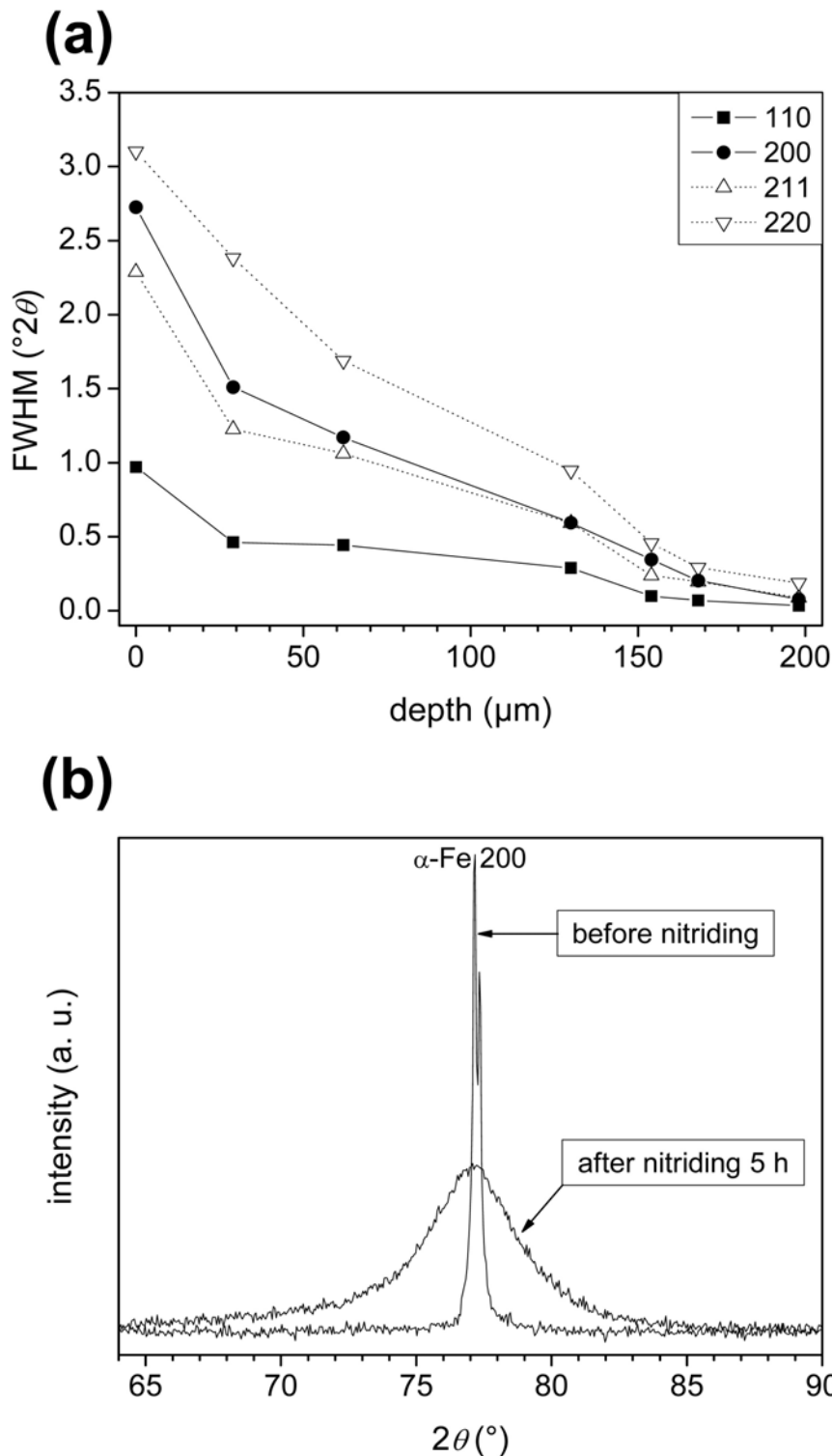


Fig. 4.6: (a) Structural line broadening (FWHM = full width of half maximum) of XRD ferrite reflections ( $\alpha$ -Fe 110,  $\alpha$ -Fe 200,  $\alpha$ -Fe 211 and  $\alpha$ -Fe 220) as function of depth in the nitrided zone of a nitrided specimen (5 h at 853 K). (b) The  $\alpha$ -Fe 200 reflection before nitriding and the strongly broadened overall “ $\alpha$ -Fe” 200 reflection after nitriding (Co-K $\alpha$  radiation; see text).

From the plots of lattice spacing versus  $\sin^2 \psi$  (cf. section 4.2.4) also a value for the strain-free lattice spacing can be obtained, if a biaxial state of plane stress prevails, by interpolation at the strain-free direction,  $\sin^2 \psi_0$  (cf. Ref. [15]). Thus, for the strain-free lattice spacing of the  $\alpha$ -Fe (ferrite) matrix lattice planes,  $d_0^{211}$ , it was obtained: at the nitrated surface  $d_0^{211} = 1.1763 \text{ \AA}$ , which is significantly larger than the value determined for the unnitrated core,  $d_0^{211} = 1.1735 \text{ \AA}$ . This is a clear indication of the presence of a hydrostatic tensile component of stress in the ferrite matrix (in addition to the plane state of stress) in the surface adjacent region. This hydrostatic tensile stress component is a straightforward consequence of the elastic accommodation of the positive volume misfit between nitride precipitate and ferrite matrix [21].

#### **4.8 Nitrogen and aluminium segregation at grain boundaries**

In the transition region between nitrated zone and unnitrated core a relatively enhanced amount of nitrogen can be observed at grain boundaries; see the concentration-*depth* profiles (EPMA) shown in Fig. 4.7: the white dotted arrows indicate the course of the electron beam line-scans (as revealed by carbon deposition on the scanned tracks in the scanning electron microscopy (SEM) micrographs). At sites where the electron beam hits grain boundaries, indicated by “GB” in the SEM micrographs, the nitrogen concentration is increased, whereas the concentration levels of Cr and Al remain constant (but see results of STEM analysis of much higher lateral resolution, discussed below).

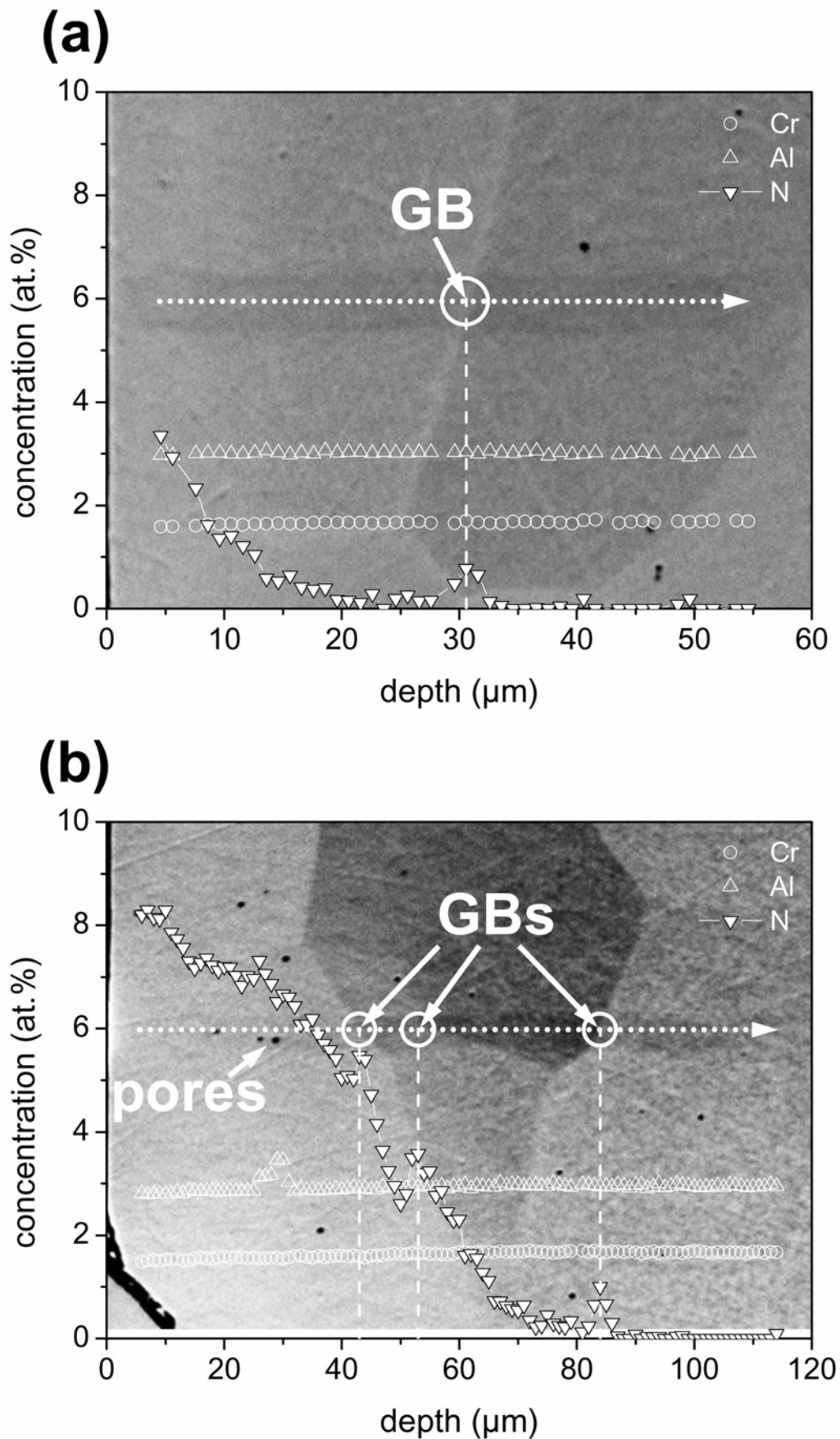


Fig. 4.7: EPMA concentration-depth profiles of (a) a specimen nitrided for 0.25 h at 853 K and (b) a specimen nitrided for 1 h at 853 K, and the corresponding SEM images. The N concentration increases abruptly at grain boundaries in the transition region between nitrided zone and unnitrided core.

The concentration profiles (EPMA) showing the elemental distribution *parallel* to the specimen surface at depths from 50  $\mu\text{m}$  to 80  $\mu\text{m}$  (i.e. in the transition region between nitrided zone and unnitrided core of a specimen nitrided for 1 h at 853 K; cf. Fig. 4.1) *in and across a single grain* are shown in the left-hand column of Fig. 4.8. The overall N content decreases with increasing depth due to the overall N concentration-depth profile (along the vertical direction in the figures) in the nitrided zone. The N concentration at the boundaries of the grain considered, in comparison with the N concentration in the grain centre, is clearly increased. The right-hand column in Fig. 4.8 shows the corresponding microhardness results. The overall microhardness decreases with increasing depth and thus decreasing N content. The microhardness at the grain boundary is significantly increased, in comparison with the microhardness inside the grain, except in Fig. 4.8 j (very close to the unnitrided core), where the nitride precipitation has just started.

The microhardness was determined in the grain centre and close to the grain boundary for two single grains at depths of about 100  $\mu\text{m}$  (Fig. 4.9 a) and 120  $\mu\text{m}$  (Fig. 4.9 b), respectively, within the nitrided zone of a nitrided specimen (15 h at 853 K). The microhardness inside the grains is significantly higher than close to the grain boundary (also note the contrast difference between the centre of the grain (less dark) and near the grain boundaries (dark); see Fig. 4.9). It follows from Fig. 4.8 (corresponding with the transition region nitrided zone/unnitrided core) and Fig. 4.9 (within the nitrided zone) that upon nitriding the microhardness starts to increase at grain boundaries (cf. Figs. 4.8 d, f, h and j), but the maximum microhardness in a single grain occurs upon continued nitriding eventually in the grain centre (cf. Fig. 4.9).

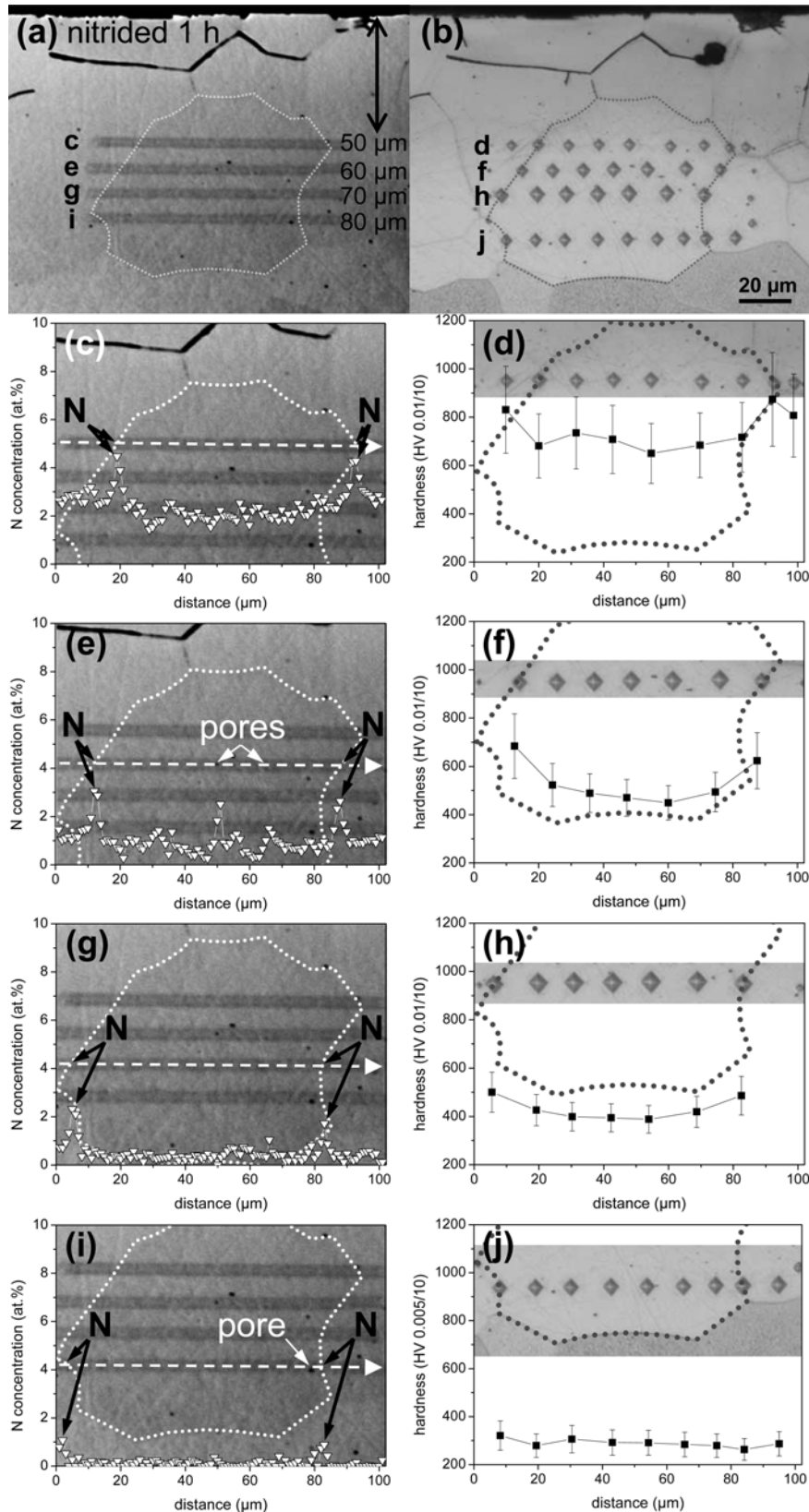


Fig. 4.8: (a) SEM image of the cross-section of a nitrided specimen (1 h at 853 K) showing EPMA line-scans taken parallel to the surface (as revealed by carbon deposition; see Fig. 4.8 a) across a single grain at several depths (50  $\mu\text{m}$  to 80  $\mu\text{m}$ ) in the transition zone between nitrided zone and unnitrided core. (b) LM micrograph of the same grain as in Fig. 4.8 a with tracks of microhardness indentations along lines across the grain, parallel to the surface, near the sites of the EPMA line-scans of Fig. 4.8 a. Results of the microhardness measurements across the grain have been depicted in Fig. 4.8 b. The load in Figs. 4.8 d, f, and h was 98 mN, whereas the load in Fig. 4.8 j was 49 mN.



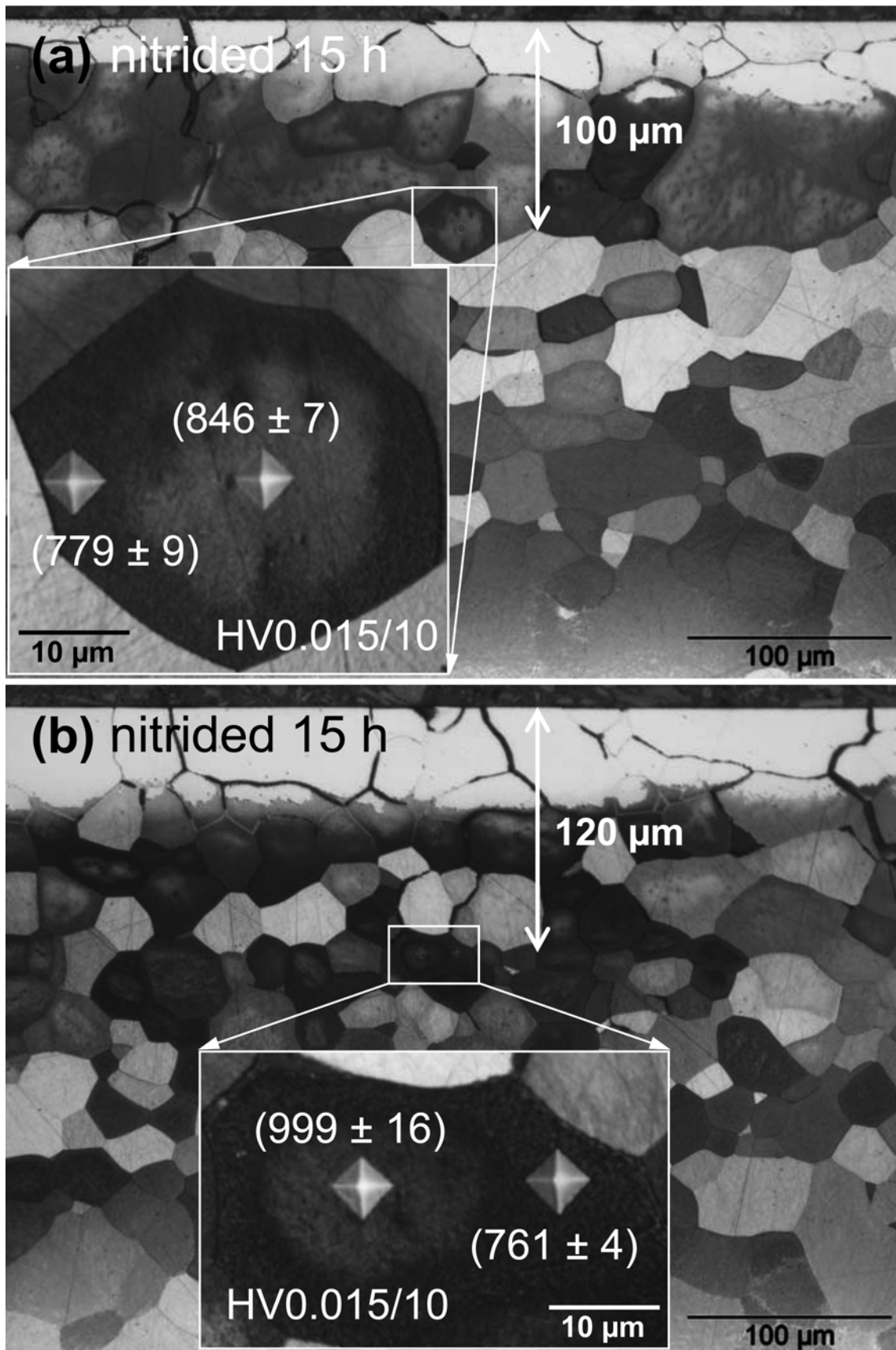


Fig. 4.9: LM micrographs of an etched cross-section (0.5 % Nital) of a nitrided specimen (15 h at 853 K) showing microhardness indentations (load: 147 mN, dwell time 10 s) in the centre and close to the grain boundaries of single grains at a depth of about (a) 100  $\mu\text{m}$  and (b) 120  $\mu\text{m}$ , i.e. *within the nitrided zone*. The error margins indicated represent the standard error of the mean of ten read-outs of the indentations. The microhardness in the grain centres is slightly higher than the microhardness close to the grain boundaries.

STEM line-scans (EDX with an electron beam of diameter two to three orders of magnitude smaller than as used in EPMA), shown in Fig. 4.10, reveal that the Al concentration is enhanced at grain boundaries in the nitrated zone and in the transition region, and also at grain boundaries in the unnitrated core (cf. Fig. 4.10 f; for quantitative analysis of Fe, Cr and Al the Cliff–Lorimer ratio technique [23] was used, considering X-ray absorption and assuming a maximum TEM foil thickness of 200 nm; since the drift of the sample limited the counting time, reliable results for the N concentration could not be obtained). The segregation of Al at grain boundaries is apparently not an effect of the nitriding process, because Al has segregated at grain boundaries before nitriding occurred. Evidently, no segregation of Cr at grain boundaries occurs before and during nitriding. Because N has a strong affinity to Al, a relatively enhanced presence of N at grain boundaries can be expected in the transition zone, as observed (cf. Fig. 4.7).

A foil ( $20 \times 15 \times 0.2 \text{ mm}^3$ ) of the alloy considered in this paper was through-nitrated (24 h at 853 K) and broken under ultra-high vacuum in the AES facility to investigate the fracture surface by Auger electron spectroscopy. Two kinds of fracture are visible on the SEM image in Fig. 4.11 a: transgranular fracture (smooth fracture surface) and intergranular fracture (rough fracture surface). Concentration-depth profiles perpendicular to the fracture surfaces were acquired by AES for both types of fracture surfaces (cf. section 4.2.6). The corresponding element distributions are shown as function of sputter time in Figs. 4.11 b and c. In case of the transgranular fracture surface (fracture through a grain), the elemental distribution does not change significantly with increasing sputter time (Fig. 4.11 b). However, in case of intergranular fracture area (fracture along a grain boundary), the Al and N concentrations (and not the Cr concentration) are significantly increased at the grain boundary (Fig. 4.11 c).

The relatively enhanced presence of only Al and N, and not of Cr, at the grain boundaries suggests that at the grain boundaries AlN has precipitated upon nitriding, and not  $\text{Cr}_{1-x}\text{Al}_x\text{N}$  as occurs in the interior of the nitrated grains. TEM evidence (in combination with EDX elemental analysis) was obtained in this project for the occurrence of some hexagonal, wurtzite structure type AlN precipitates in the nitrated zone.

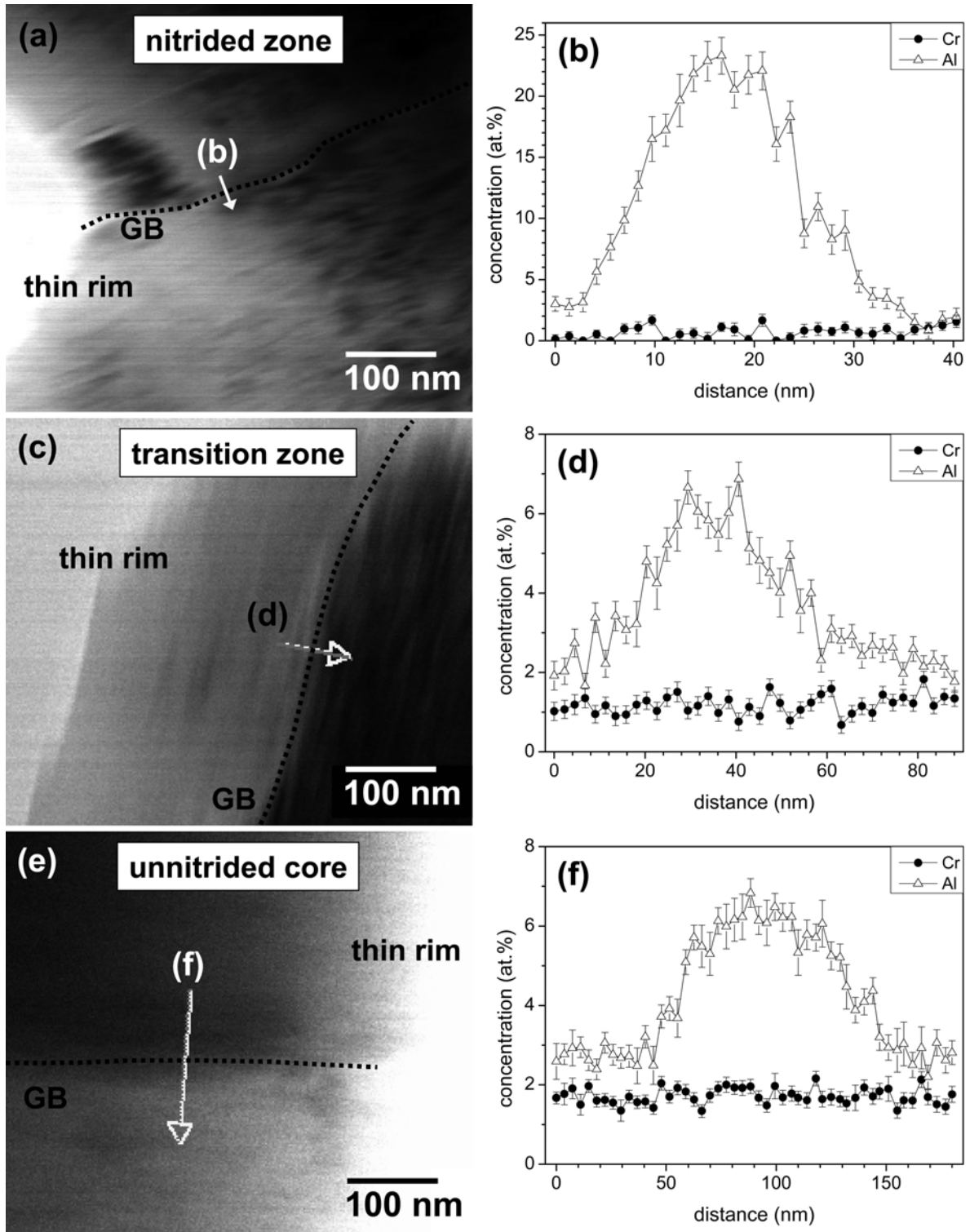


Fig. 4.10: STEM results from specimens nitrated 15 h at 853 K: (a) bright field (BF) image (the image is strongly astigmatic because of the ferromagnetism of the sample) of a grain boundary (GB) in the nitrided zone (taken from a depth of about 215  $\mu\text{m}$ ). (b) Results of the corresponding EDX line-scan (indicated by the arrow in Fig. 4.10 a). (c) BF image of a GB in the transition zone (taken from a depth of about 340  $\mu\text{m}$ ). (d) Results of the corresponding EDX line-scan (indicated by the arrow in Fig. 4.10 c). (e) BF image of a GB in the unnitrided core (taken from the sample centre at a depth of about 500  $\mu\text{m}$ ). (f) Results of the corresponding EDX line-scan (indicated by the arrow in Fig. 4.10 e). Evidently some Al, and no Cr at all, has segregated at grain boundaries over the whole cross-section.

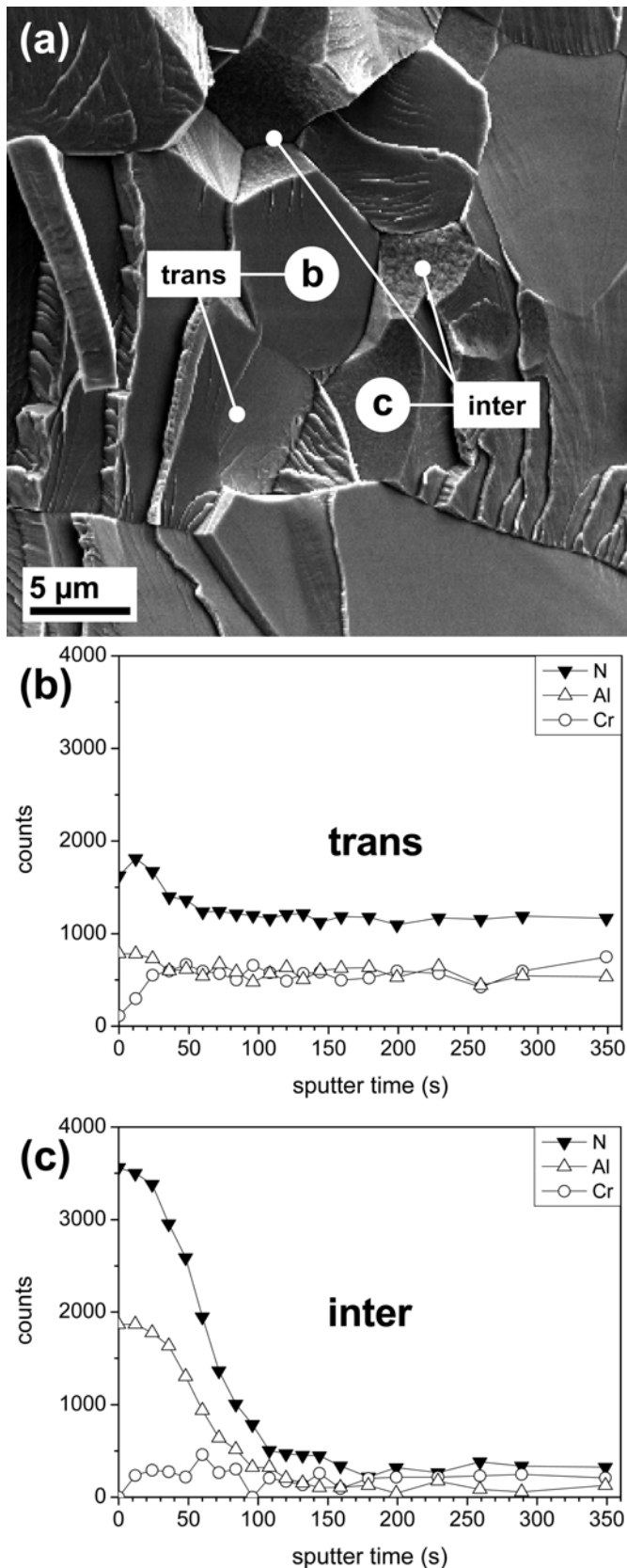


Fig. 4.11: (a) SEM image of the fracture surface of a through-nitrided foil (24 h at 853 K) showing trans- and intergranular fracture behaviour. (b) AES sputter depth profile of a *transgranular* fracture area (i.e. fracture through a grain) showing the elemental depth distribution at the site indicated in Fig. 4.11 a. (c) AES sputter depth profile of an *intergranular* fracture area (i.e. fracture along a grain boundary) showing the elemental depth distribution at the site indicated in Fig. 4.11 a. Relatively enhanced N and Al contents occur at the grain boundary.

The precipitation of AlN in the hexagonal, wurtzite structure type does not occur in the interior of the grains upon nitriding the Fe–1.5wt.%Cr–1.5wt.%Al (i.e. Fe–1.6at.%Cr–3.1at.%Al) alloy; there  $\text{Cr}_{1-x}\text{Al}_x\text{N}$  precipitates develop (cf. chapter 2). However, the Al segregated at the grain boundaries can lead to such hexagonal, wurtzite structure type AlN precipitates upon nitriding as accommodation of the appreciable volume misfit between the hexagonal, wurtzite structure type AlN and the  $\alpha$ -Fe matrix may be realised relatively easily at grain boundaries with their inherent relatively irregular and flexible atomic arrangement. The presence of such precipitates at the grain boundaries in the nitrided zone contributes to the apparent grain-boundary brittleness (cf. section 4.6).

## 4.9 Conclusions

The following picture emerges for the development of the microstructure of ferritic Fe–1.5wt.%Cr–1.5wt.%Al (i.e. Fe–1.6at.%Cr–3.1at.%Al) alloy upon nitriding.

- (i) Upon nitriding cubic, rock-salt structure type  $\text{Cr}_{1-x}\text{Al}_x\text{N}$  precipitates develop in the nitrided zone, with a higher density and smaller size in the surface adjacent region due to the higher supersaturation near the surface in the nitrided zone.
- (ii) Elastic accommodation of the misfit between the  $\text{Cr}_{1-x}\text{Al}_x\text{N}$  precipitates and the ferrite matrix leads to uptake of a large amount of excess nitrogen, in particular in the surface adjacent region of the nitrided zone, which is compatible with (i).
- (iii) The ferrite matrix of the nitrided zone is highly strained (most pronouncedly in the surface adjacent region; cf. (i) and (ii)) and exhibits a hydrostatic tensile component of stress, in agreement with the state of stress corresponding with (ii).
- (iv) The presence of Al segregated at grain boundaries, already before nitriding, leads to the precipitation of AlN at grain boundaries in the nitrided zone. Cr does not segregate.
- (v) Plastic deformation (e.g. by creep) occurs in the nitrided zone, first in the oldest part (i.e. surface adjacent region) of the nitrided zone. Upon continued nitriding, this leads to planar tensile stress components of pronounced value in the surface adjacent region followed by planar compressive stress components in a deeper (and thus less aged) region of the nitrided zone.

(vi) The precipitation of initially dissolved excess nitrogen at grain boundaries in the surface adjacent region (i.e. the oldest part) of the nitrified zone, and the presence of AlN precipitates at the grain boundaries (see (iv) above), and the occurrence of tensile planar stress in the surface adjacent region (see (v) above), promote the initialisation and growth of cracks starting at the surface and propagating more or less perpendicular to the surface along grain boundaries.

## Acknowledgements

The authors wish to thank Mr. J. Köhler and Mr. P. Kress for assistance with the nitriding experiments, Mrs. S. Haug for assistance with the EPMA experiments, Mr. W.-D. Lang for TEM sample preparation, Mrs. M. Kelsch for assistance during the first stage of TEM experiments, Dr. W. Sigle for assistance during the STEM experiments, discussion and critical reading of the manuscript, Mr. B. Siegle for assistance with the AES experiments and Dr. U. Welzel and Dr. A. Leineweber for scientific discussion.

## References

- [1] C. H. Knerr, T. C. Rose and J. H. Filkowski (1991). Gas nitriding. ASM Handbook: Heat Treating. J. R. Davis, G. M. Davidson, S. R. Lampman, T. B. Zorc, J. L. Daquila, A. W. Ronke, K. L. Henniger and R. C. Uhl. Metals Park, Ohio, ASM International. 4: 387-409.
- [2] E. J. Mittemeijer and J. Grosch, Eds. Proceedings of 'AWT-Tagung Nitrieren und Nitrocarburieren', Arbeitsgemeinschaft Wärmebehandlung und Werkstofftechnik e.V., Wiesbaden (1991).
- [3] D. Liedtke, U. Baudis, J. Boßlet, U. Huchel, H. Klümper-Westkamp, W. Lerche and H. J. Spies, Wärmebehandlung von Eisenwerkstoffen Nitrieren und Nitrocarburieren, Renningen, Expert Verlag (2006).
- [4] E. J. Mittemeijer and J. T. Slycke, Surf. Eng. 12 (1996) 152-162.
- [5] H. J. Grabke, Ber. Bunsenges. Physik. Chem. 72 (1968) 533-541.
- [6] E. J. Mittemeijer and M. A. J. Somers, Surf. Eng. 13 (1997) 483-497.

- [7] D. H. Jack, *Acta Metall.* 24 (1976) 137-146.
- [8] M. H. Biglari, C. M. Brakman and E. J. Mittemeijer, *Philos. Mag. A* 72 (1995) 1281-1299.
- [9] R. E. Schacherl, P. C. J. Graat and E. J. Mittemeijer, *Z. Metallk.* 93 (2002) 468-477.
- [10] S. S. Hosmani, R. E. Schacherl and E. J. Mittemeijer, *Acta Mater.* 53 (2005) 2069-2079.
- [11] JCPDS-International Centre for Diffraction Data (2002), PCPDFWIN, Version 2.3.
- [12] J. L. Pouchou and F. Pichoir, *Rech. Aerosp.* (1984) 167-192.
- [13] I. C. Noyan and J. B. Cohen, *Residual stress: measurement by diffraction and interpretation*, Berlin, Springer (1987).
- [14] V. Hauk, *Structural and residual stress analysis by nondestructive methods*, Amsterdam, Elsevier (1997).
- [15] U. Welzel, J. Ligot, P. Lamparter, A. C. Vermeulen and E. J. Mittemeijer, *J. Appl. Cryst.* 38 (2005) 1-29.
- [16] A. Kumar, U. Welzel and E. J. Mittemeijer, *J. Appl. Cryst.* 39 (2006) 633-646.
- [17] N. E. Vives Diaz, R. E. Schacherl, L. F. Zagonel and E. J. Mittemeijer, *Acta Mater.* 56 (2008) 1196-1208.
- [18] S. S. Hosmani, R. E. Schacherl and E. J. Mittemeijer, *Acta Mater.* 54 (2006) 2783-2792.
- [19] P. M. Hekker, H. C. F. Rozendaal and E. J. Mittemeijer, *J. Mater. Sci.* 20 (1985) 718-729.
- [20] M. H. Biglari, C. M. Brakman, E. J. Mittemeijer and S. van der Zwaag, *Philos. Mag. A* 72 (1995) 931-947.
- [21] M. A. J. Somers, R. M. Lankreijer and E. J. Mittemeijer, *Philos. Mag. A* 59 (1989) 353-378.
- [22] N. E. Vives Diaz, S. S. Hosmani, R. E. Schacherl and E. J. Mittemeijer, *Acta Mater.* 56 (2008) 4137-4149.
- [23] G. Cliff and G. W. Lorimer, *J. Microsc.-Oxf.* 103 (1975) 203-207.





## Chapter 5

# Summary

### 5.1 Introduction

Gaseous nitriding is an important thermochemical surface engineering process that improves technical properties like fatigue, wear and corrosion resistance of ferritic steel workpieces. It is usually performed in an ammonia/hydrogen gas mixture at temperatures between about 500 °C and 600 °C (i.e. 773 K and 873 K). In the process ammonia dissociates at the workpiece surface and atomic nitrogen diffuses into the surface adjacent ferrite matrix towards larger depths. Depending on the nitriding conditions (i.e. temperature, pressure and chemical potential of nitrogen in the gas atmosphere), different phases can be formed at the sample surface. According to the Fe–N phase diagram the following phases (in the given order) will be formed with increasing nitrogen content:  $\alpha$ -Fe (ferrite with dissolved nitrogen),  $\gamma'$ -Fe<sub>4</sub>N<sub>1-x</sub> and  $\epsilon$ -Fe<sub>3</sub>N<sub>1+y</sub>. The formation of iron nitrides ( $\epsilon$ -Fe<sub>3</sub>N<sub>1+y</sub> and/or  $\gamma'$ -Fe<sub>4</sub>N<sub>1-x</sub>) at the surface adjacent region of the workpiece (external nitriding) leads to the development of a compound layer (sometimes also called “white layer”), which improves the wear and corrosion properties. Underneath the possible compound layer, alloying-element nitrides precipitate within the nitrated zone (internal nitriding), the so-called diffusion zone, and improve the fatigue properties. During gaseous nitriding the chemical activity of nitrogen dissolved in the workpiece at its surface can be accurately adjusted by the so-called nitriding potential  $r_N = \frac{p_{\text{NH}_3}}{p_{\text{H}_2}^{3/2}}$ . By setting the value of the nitriding

potential, the occurrence of a compound layer at the workpiece surface can be controlled. Since nitriding processes are widely used in industry and since the application practice is still largely based on phenomenology, in particular on the nitriding of multicomponent, technical alloys, there is a great interest in fundamental knowledge on this topic.

A certain level of understanding has been reached in the past about the nitriding behaviour of simple binary iron-based alloys. In practice, however, more than one alloying element occurs in technical alloys. Typical alloying elements in technical nitriding steels with a strong affinity for nitrogen are, amongst others, Cr and Al. Nitriding of *binary* Fe–Cr and Fe–Al alloys has been investigated rather extensively. However, there is sparse and ambiguous information about the nitriding behaviour of iron-based alloys containing both Cr and Al as alloying elements and fundamental work on the nitriding of the *ternary* system Fe–Cr–Al does not exist yet.

The purpose of the present thesis is to give a deeper insight in the nitriding behaviour of the ternary iron-based alloy with the composition Fe–1.5wt.%Cr–1.5wt.%Al (i.e. Fe–1.6at.%Cr–3.1at.%Al), and the microstructure and properties of the diffusion zone.

## 5.2 Experimental

### 5.2.1 Specimen preparation

The Fe–1.5wt.%Cr–1.5wt.%Al alloy was produced by melting appropriate amounts of the pure elements in a furnace under a protective gas atmosphere. After casting the chemical composition and the impurities of the alloy were determined by chemical analysis (inductively coupled plasma – optical emission spectroscopy, carrier gas hot extraction and combustion method). The element distribution (homogeneity) after casting was validated by electron probe microanalysis (EPMA). Nitriding specimens with a more or less equiaxed, single phase microstructure were manufactured by cold-rolling and subsequent recrystallisation.

### 5.2.2 Nitriding

The nitriding process was performed in a multizone quartz-tube furnace with an ammonia/hydrogen gas mixture flux at a temperature of  $(853 \pm 1)$  K. The gas fluxes were adjusted by mass-flow controllers and correspond to a nitriding potential of  $r_N = 0.104 \text{ atm}^{-1/2}$ . The nitriding process was stopped by quenching the nitrified specimen in water. The nitriding potential was chosen such that no iron nitrides developed at the specimen surface, i.e. the nitrified layer consisted of the surface

adjacent diffusion zone exhibiting only alloying element nitride precipitation and no iron nitrides.

### 5.2.3 Specimen characterisation

Phase analysis was performed by means of X-ray diffraction (XRD) applied to the surface of all specimens before nitriding, after nitriding, after subsequent annealing and after uncovering deeper areas of the nitrated zone by removing material from the surface. Detected phases were identified by the  $2\theta$  positions of their XRD reflections.

For the preparation of light micrographs, pieces of specimens were embedded, ground, polished and etched with Nital (i.e.  $\text{HNO}_3$  dissolved in ethanol).

Microhardness measurements of specimens were performed with a Vickers microhardness tester.

Elemental concentration depth profiles were determined by EPMA performed on cross-sections perpendicular to the surface, starting from the surface across the cross-section towards the centre of the specimen.

The structure, morphology and chemical composition of nitride precipitates in the nitrated and annealed specimens were investigated by transmission electron microscopy (TEM) techniques. TEM samples taken at selected depths of the nitrated zone were produced by the jet-electropolishing technique or by argon ion milling. Bright field images, dark field images and selected area diffraction patterns provided insight in the (crystal) structure and morphology of the nitride precipitates. To reveal the (atomic) structure at the precipitate/matrix interfaces, high resolution transmission electron microscopy (HRTEM) was performed. Scanning transmission electron microscopy (STEM) in combination with energy dispersive X-ray spectroscopy (EDX) was applied to get information about the chemical composition of individual nitride precipitates and to investigate the elemental distribution at and near grain boundaries.

For quantitative analysis of excess nitrogen (e.g. nitrogen additionally dissolved in the strain field around the precipitates and at the precipitate/matrix interface) uptake a nitrogen absorption isotherm was determined by pre-nitriding a foil at constant temperature adjusting different nitriding potentials and subsequently denitriding it. The excess nitrogen uptake was measured by weighing the mass difference of the foil after pre- and denitriding.

Auger electron spectroscopy (AES) was performed to investigate the fracture surface of a through-nitrided specimen and to determine sputter depth profiles for different fracture sites. Quantitative elemental concentration depth profiles were determined by sputtering and measuring alternatively.

To determine the residual stress depth profile alternating XRD stress measurements, using the  $\sin^2\psi$  method, and removals of a surface layer with a certain thickness were performed. The XRD  $\sin^2\psi$  method for stress measurement was performed at a constant penetration depth of 0.5  $\mu\text{m}$  (i.e. the penetration depth of the X-rays was constant for variable  $\psi$ ). The surface layers were removed mechanically layer by layer from the original specimen surface. The peak position of the  $\alpha$ -Fe 211 reflection was determined in dependence on the tilt angle  $\psi$ . The lattice spacings  $d_{\alpha\text{-Fe } 211}$  were calculated from the peak positions using the Bragg equation. The calculated lattice spacings were plotted against  $\sin^2\psi$ , yielding straight lines within experimental accuracy. The residual stress values were calculated from the slopes of these straight lines for the case of a macroscopically elastically isotropic specimen with a plane, rotationally symmetric biaxial stress state at the investigated surface.

## 5.3 Results

### 5.3.1 Crystal structure and morphology of mixed $\text{Cr}_{1-x}\text{Al}_x\text{N}$ nitride precipitates

Nitriding of the ternary iron-based alloy Fe–1.5wt.%Cr–1.5wt.%Al (i.e. Fe–1.6at.%Cr–3.1at.%Al) leads to the precipitation of mixed, cubic, rock-salt structure type  $\text{Cr}_{1-x}\text{Al}_x\text{N}$  precipitates. These precipitates are not in thermodynamic equilibrium, which would involve precipitation of cubic, rock-salt structure type CrN and hexagonal, wurtzite structure type AlN. The mixed, cubic, rock-salt structure type  $\text{Cr}_{1-x}\text{Al}_x\text{N}$  precipitates develop because diffusion of Cr and Al in ferrite, as compared to diffusion of N in ferrite, is very slow and precipitation of hexagonal, wurtzite structure type AlN is a process with difficult nucleation. The precipitation of mixed cubic, rock-salt structure type  $\text{Cr}_{1-x}\text{Al}_x\text{N}$  already releases a considerable (although not maximal) amount of energy. The  $\text{Cr}_{1-x}\text{Al}_x\text{N}$  precipitates develop as platelets initially coherent with the ferrite matrix according to the Bain orientation relationship. At this

initial stage the nitride platelets diffract coherently with the matrix and separate nitride reflections do not occur in the X-ray diffractogram. More and finer nitride precipitates occur near the surface than at larger depths beneath the surface, because the driving force for nitride precipitation is largest near the surface. For coarser nitride platelets (i.e. at larger depths; see above) the Bain orientation relationship is no longer fulfilled exactly. The precipitates “break up” (contrast variation along the platelets in transmission electron micrographs and splitting of electron diffraction spots).

Large amounts of excess nitrogen are taken up upon precipitation of the  $\text{Cr}_{1-x}\text{Al}_x\text{N}$  precipitates, as a result of the elastic accommodation of the precipitate/matrix misfit. The excess nitrogen uptake is largest near the surface, because the finest precipitates occur there (see above) and are subjected to (almost) full elastic accommodation of the precipitate/matrix misfit. Excess nitrogen, which remains in the specimen after denitriding is ascribed to nitrogen atoms strongly bonded at the precipitate platelet surfaces to in particular the Al atoms in the mixed nitride at the platelet surfaces.

### **5.3.2 Phase transformation of mixed $\text{Cr}_{1-x}\text{Al}_x\text{N}$ nitride precipitates in ferrite**

Upon nitriding the ferritic iron-based alloy Fe–1.5wt.%Cr–1.5wt.%Al, mixed, metastable cubic, rock-salt structure type  $\text{Cr}_{1-x}\text{Al}_x\text{N}$  nitrides develop in the nitrided zone, which contains considerably more nitrogen than necessary to precipitate all Cr and all Al (i.e. excess nitrogen; see above). Subsequent annealing at higher temperature than the nitriding temperature leads to the development of the equilibrium precipitates CrN and AlN.

Cubic, rock-salt structure type and hexagonal, wurtzite structure type particles occur after annealing in the nitrided zone, which exhibit a Bain-type orientation relationship and a Pitsch–Schrader orientation relationship, respectively, with the ferrite matrix, and which correspond with CrN and AlN, respectively. Part of the cubic, rock-salt structure type particles is (still) mixed  $\text{Cr}_{1-x}\text{Al}_x\text{N}$  nitride, however containing less Al than initially present. Transformation of the initial mixed  $\text{Cr}_{1-x}\text{Al}_x\text{N}$  nitrides proceeds by their Al depletion. The subsequent precipitation of AlN occurs in the interior and at grain boundaries of the matrix. A coarser microstructure results. The precipitates no longer exhibit strong coherency with the ferrite matrix, as reflected by the strong

decrease of the broadening of the XRD ferrite-matrix reflections and the distinct decrease of hardness.

Annealing leads to the presence of nitrogen in the originally unnitrided core by diffusion of mobile excess nitrogen from the nitrated zones. This nitrogen immediately precipitates as relatively coarse CrN at grain boundaries and as smaller cubic, rock-salt structure type CrN and hexagonal, wurtzite structure type AlN in the interior of the grains. Mixed  $\text{Cr}_{1-x}\text{Al}_x\text{N}$  nitride does not develop.

### **5.3.3 The microstructure of the diffusion zone of a gaseously nitrated Fe–1.5wt.%Cr–1.5wt.%Al alloy**

The following picture emerges for the development of the microstructure of ferritic, ternary Fe–1.5wt.%Cr–1.5wt.%Al alloy upon nitriding. Upon nitriding cubic, rock-salt structure type  $\text{Cr}_{1-x}\text{Al}_x\text{N}$  precipitates develop in the nitrated zone, with a higher density and smaller size in the surface adjacent region due to the higher supersaturation near the surface in the nitrated zone. Elastic accommodation of the misfit between the  $\text{Cr}_{1-x}\text{Al}_x\text{N}$  precipitates and the ferrite matrix leads to uptake of a large amount of excess nitrogen, in particular in the surface adjacent region of the nitrated zone (see above). The ferrite matrix of the nitrated zone is highly strained (most pronouncedly in the surface adjacent region; see above) and exhibits a hydrostatic tensile component of stress, in agreement with the state of stress corresponding with the elastic accommodation of the misfit between the  $\text{Cr}_{1-x}\text{Al}_x\text{N}$  precipitates and the ferrite matrix. The presence of Al segregated at grain boundaries, already before nitriding, leads to the precipitation of AlN at grain boundaries in the nitrated zone. Cr does not segregate. Plastic deformation (e.g. by creep) occurs in the nitrated zone, first in the oldest part (i.e. surface adjacent region) of the nitrated zone. Upon continued nitriding, this leads to planar tensile stress components of pronounced value in the surface adjacent region followed by planar compressive stress components in a deeper (and thus less aged) region of the nitrated zone. The precipitation of initially dissolved excess nitrogen at grain boundaries in the surface adjacent region (i.e. the oldest part) of the nitrated zone, and the presence of AlN precipitates at the grain boundaries (see above), and the occurrence of tensile planar stress in the surface adjacent region (see above), promote

---

the initialisation and growth of cracks starting at the surface and propagating more or less perpendicular to the surface along grain boundaries.





## Chapter 6

# Zusammenfassung in deutscher Sprache

### 6.1 Einleitung

Gasnitrieren ist ein wichtiges thermochemisches Verfahren zur Wärmebehandlung ferritischer Eisenbasislegierungen. Es verbessert im Allgemeinen das Ermüdungsverhalten, die Verschleißfestigkeit und die Korrosionsbeständigkeit. Gasnitrieren wird üblicherweise in einer Gasmischung aus Ammoniak und Wasserstoff bei Temperaturen zwischen 500 °C und 600 °C (773 K und 873 K) durchgeführt. Während des Nitrierprozesses zerfällt Ammoniak an der ferritischen Werkstückoberfläche und atomarer Stickstoff diffundiert in die oberflächennahe Eisenmatrix ein. In Abhängigkeit der Nitrierbedingungen (Temperatur, Druck und chemisches Potential des Stickstoffs in der Gasatmosphäre) können verschiedene Phasen an der Werkstückoberfläche entstehen. In Übereinstimmung mit dem Fe–N Phasendiagramm entstehen folgende Phasen in der angegebenen Reihenfolge mit zunehmendem Stickstoffgehalt:  $\alpha$ -Fe (Ferrit mit gelöstem Stickstoff),  $\gamma'$ -Fe<sub>4</sub>N<sub>1-x</sub> und  $\epsilon$ -Fe<sub>3</sub>N<sub>1+y</sub>. Die Bildung der Eisennitride ( $\epsilon$ -Fe<sub>3</sub>N<sub>1+y</sub> und/oder  $\gamma'$ -Fe<sub>4</sub>N<sub>1-x</sub>) im an die Werkstückoberfläche angrenzenden Bereich (äußeres Nitrieren) führt zur Entstehung einer Verbindungsschicht (auch „weiße Schicht“ genannt), die die Verschleißfestigkeit und Korrosionsbeständigkeit verbessert. Unterhalb der etwaigen Verbindungsschicht scheiden so genannte innere Nitride in der Nitrierzone aus (inneres Nitrieren), bestehend aus chemischen Verbindungen zwischen Legierungselementen und Stickstoff. Dieser Bereich der Nitrierschicht wird Diffusionszone genannt. Die inneren Nitride in der Diffusionszone bewirken eine Verbesserung des Ermüdungsverhaltens. Während des Gasnitrierens kann die chemische Aktivität des an der Werkstückoberfläche gelösten Stickstoffs sehr genau durch die so genannte Nitrierkennzahl  $r_N = \frac{p_{\text{NH}_3}}{p_{\text{H}_2}^{3/2}}$  eingestellt werden. In Abhängigkeit der Nitrierkennzahl und Nitriertemperatur können Werkstücke mit oder ohne Verbindungsschicht

(Eisennitride) an der Oberfläche hergestellt werden. Da Nitrieren ein weit verbreitetes industrielles Verfahren ist und die praktische Anwendung immer noch stark auf Phänomenologie basiert, insbesondere was das Nitrieren von technischen Mehrkomponentenlegierungen betrifft, besteht ein großes Interesse an fundamentalem Wissen auf diesem Gebiet.

Ein gewisses Grundlagenverständnis über das Nitrierverhalten von einfachen, binären Eisenbasislegierungen konnte in der Vergangenheit geschaffen werden. Technische Legierungen in der praktischen Anwendung haben jedoch in der Regel mehr als ein Legierungselement. Typische Legierungselemente in technischen Nitrierstählen, die eine starke Affinität zu Stickstoff haben, sind unter anderem Cr und Al. Das Nitrierverhalten von *binären* Fe–Cr- und Fe–Al-Legierungen wurde bereits ausführlich untersucht. Über das Nitrierverhalten von Eisenbasislegierungen, die beide Elemente Cr und Al enthalten, gibt es dagegen nur wenig und zudem uneinheitliche Informationen. Grundlegende Forschungsarbeiten über das Nitrierverhalten des *ternären* Systems Fe–Cr–Al existieren bisher überhaupt nicht.

Ziel dieser Dissertation ist es, einen tieferen Einblick in das Nitrierverhalten der ternären Eisenbasislegierung mit der chemischen Zusammensetzung Fe–1,5Gew.%Cr–1,5Gew.%Al (Fe–1,6At.%Cr–3,1At.%Al) zu geben, insbesondere in die Mikrostruktur und Eigenschaften der Diffusionszone.

## 6.2 Experimentelles

### 6.2.1 Probenpräparation

Die Fe–1,5Gew.%Cr–1,5Gew.%Al-Legierung wurde durch Schmelzen der reinen Elemente in einem Induktionsofen unter Schutzgasatmosphäre hergestellt. Nach dem Abgießen und Erstarren wurde die Zusammensetzung und der Anteil an Verunreinigungen in der Legierung durch chemische Analyseverfahren bestimmt (Atom-Emissions-Spektroskopie mit Hilfe von induktiv gekoppeltem Plasma, Trägergas-Heißextraktion und Verbrennungsverfahren). Die Elementverteilung im Abguss (Homogenität) wurde durch Elektronenstrahlmikroanalyse (ESMA) bestätigt. Nitrierproben mit einer mehr oder weniger gleichachsigen Einphasenmikrostruktur wurden durch Kaltwalzen und anschließendes Rekristallisieren hergestellt.

### **6.2.2 Nitrieren**

Der Nitrierprozess wurde in einem Mehrzonenofen bei einer Temperatur von  $(853 \pm 1)$  K unter einem Gasstrom aus Ammoniak und Wasserstoff nach dem Durchflussprinzip durchgeführt. Die Gasflüsse wurden mit Hilfe von Massenfluss-Reglern eingestellt und entsprachen einer Nitrierkennzahl von  $r_N = 0,104 \text{ atm}^{-1/2}$ . Der Nitriervorgang wurde durch Abschrecken der Probe in Wasser abgebrochen. Die Nitrierkennzahl wurde so gewählt, dass sich keine Eisennitride an der Probenoberfläche bilden konnten, d. h. die Nitrierschicht bestand aus einer an die Probenoberfläche angrenzenden Diffusionszone, in der sich nur die inneren Nitride der Legierungselemente ausgeschieden hatten (ohne Entstehung von Eisennitriden).

### **6.2.3 Charakterisierung der Proben**

Phasenanalyse wurde mit Hilfe von Röntgendiffraktometrie (XRD) an Probenoberflächen durchgeführt, vor dem Nitrieren, nach dem Nitrieren sowie nach anschließender Wärmebehandlung und nach Freilegung tieferer Schichten der Nitrierzone durch Materialabtrag. Nachweisbare Phasen wurden durch die  $2\theta$ -Lagen ihrer Reflexe im Röntgendiffraktogramm identifiziert.

Für die Anfertigung von Gefügebildern wurden Probenstücke eingebettet, geschliffen, poliert und mit Nital ( $\text{HNO}_3$  gelöst in Ethanol) geätzt.

Mikrohärtemessungen an Proben wurden mit einem Vickers Mikrohärtemessgerät durchgeführt.

Tiefenprofile von Elementkonzentrationen wurden mit Hilfe von ESMA an Querschliffen senkrecht zur Probenoberfläche aufgenommen, beginnend an der Oberfläche über die Nitrierzone bis in den nicht nitrierten Kern der Proben.

Struktur, Morphologie und chemische Zusammensetzung der inneren Nitridausscheidungen wurden in nitrierten Proben und in nitrierten und anschließend wärmebehandelten Proben mit Hilfe verschiedener Techniken der Transmissionselektronenmikroskopie (TEM) untersucht. Dazu wurden TEM Proben aus verschiedenen Tiefen der Nitrierzone durch elektrolytisches Dünnen oder durch Ionendünnen hergestellt. Hellfeldabbildungen, Dunkelfeldabbildungen und Feinbereichsbeugungsbilder lieferten Einblicke in die (Kristall)Struktur und Morphologie der inneren Nitridausscheidungen. Zur Aufdeckung der (atomaren)

Struktur an der Grenzfläche zwischen Nitridausscheidung und Eisenmatrix wurde hochauflösende Transmissionselektronenmikroskopie eingesetzt (HRTEM). Rastertransmissionselektronenmikroskopie (STEM) in Verbindung mit energiedispersiver Röntgenspektroskopie (EDS) wurde angewandt, um Informationen über die chemische Zusammensetzung individueller innerer Nitridausscheidungen zu bekommen und um die Elementverteilung an und in der Nähe von Korngrenzen zu untersuchen.

Zur quantitativen Bestimmung der Überschussstickstoffaufnahme (z. B. zusätzlich gelöster Stickstoff in Spannungsfeldern um die Ausscheidungen und an den Grenzflächen zwischen Ausscheidungen und Matrix) wurde eine Stickstoffabsorptionsisotherme aufgenommen. Dazu wurde eine Legierungsfolie vornitriert, anschließend bei konstanter Temperatur und variabler Nitrierkennzahl nitriert und schließlich jeweils wieder denitriert. Die Aufnahme an Überschussstickstoff wurde durch Wiegen der Folie nach Nitrieren und Denitrieren und Bestimmen der Massendifferenz ermittelt.

Auger-Elektronenspektroskopie (AES) wurde durchgeführt, um die Bruchfläche einer durchnitrierten Probe zu untersuchen. Mittels abwechselnden Materialabtrags durch Kathodenzerstäubung („Sputtern“) und Messen wurden quantitative Tiefenprofile an unterschiedlichen, charakteristischen Stellen der Bruchfläche aufgenommen.

Mit Hilfe der XRD  $\sin^2\psi$  Methode wurden Eigenspannungen bei konstanter Eindringtiefe von  $0,5\ \mu\text{m}$  (d. h. die Eindringtiefe der Röntgenstrahlung blieb für unterschiedliche Kippwinkel  $\psi$  konstant) gemessen. Ein Eigenspannungstiefenprofil wurde erstellt durch abwechselndes Messen der Eigenspannungen nach der  $\sin^2\psi$ -Methode und kontrollierte, schichtweise, mechanische Materialabtragung von der ursprünglichen Probenoberfläche. Die  $2\theta$ -Lage des  $\alpha\text{-Fe } 211$ -Reflexes im Röntgendiffraktogramm wurde in Abhängigkeit des Kippwinkels  $\psi$  bestimmt. Die Netzebenenabstände  $d_{\alpha\text{-Fe } 211}$  wurden mit Hilfe der Reflexpositionen und der Bragg-Gleichung berechnet. Die resultierenden Netzebenenabstände wurden über  $\sin^2\psi$  aufgetragen und ergaben Geraden innerhalb der experimentellen Genauigkeit. Die Eigenspannungswerte wurden aus den Steigungen der Geraden bestimmt unter der Annahme einer makroskopisch elastisch isotropen Probe und eines ebenen,

rotationssymmetrischen, zweiachsigen Spannungszustands in den untersuchten Oberflächen.

## 6.3 Ergebnisse

### 6.3.1 Kristallstruktur und Morphologie gemischter $\text{Cr}_{1-x}\text{Al}_x\text{N}$ Nitridausscheidungen

Beim Nitrieren der ternären Eisenbasislegierung mit der chemischen Zusammensetzung Fe-1,5Gew.%Cr-1,5Gew.%Al (Fe-1,6At.%Cr-3,1At.%Al) bilden sich gemischte  $\text{Cr}_{1-x}\text{Al}_x\text{N}$ -Ausscheidungen mit einer kubischen Steinsalz-Kristallstruktur in der Ferritmatrix. Diese inneren Nitride befinden sich nicht im thermodynamischen Gleichgewicht, das mit der Ausscheidung von kubischem CrN in der Steinsalz-Kristallstruktur und hexagonalem AlN in der Wurtzit-Kristallstruktur einhergehen würde. Die gemischten  $\text{Cr}_{1-x}\text{Al}_x\text{N}$ -Ausscheidungen in der kubischen Steinsalz-Kristallstruktur entstehen, weil die Diffusion von Cr und Al in Ferrit, im Vergleich zur Diffusion von N in Ferrit, sehr langsam vonstatten geht und das Ausscheiden von AlN in der hexagonalen Wurtzit-Kristallstruktur ein Vorgang mit erschwerter Keimbildung ist. Die Ausscheidung von gemischtem  $\text{Cr}_{1-x}\text{Al}_x\text{N}$  in der kubischen Steinsalz-Kristallstruktur setzt einen erheblichen (wenn auch nicht maximalen) Energieanteil frei. Die  $\text{Cr}_{1-x}\text{Al}_x\text{N}$ -Ausscheidungen treten in Form von Plättchen, mit einer anfangs kohärenten Grenzfläche zur Ferritmatrix entsprechend der Bain-Orientierungsbeziehung, auf. In diesem Anfangsstadium kommt es zu kohärenter Röntgenbeugung der Nitridplättchen mit der Ferritmatrix, weshalb keine separaten Nitridreflexe im Röntgendiffraktogramm auftreten. Nahe der Oberfläche der Nitrierprobe entstehen mehr und feinere Nitridausscheidungen als in tiefer liegenden Bereichen der Diffusionszone, da die Triebkraft für die Ausscheidung innerer Nitride nahe der Oberfläche am größten ist. Für gröbere Nitridplättchen (d. h. tiefer in der Diffusionszone) ist die Bain-Orientierungsbeziehung nicht länger exakt erfüllt. Die Nitridausscheidungen „beenden“ ihre Orientierungsbeziehung mit der Eisenmatrix (erkennbar anhand von Kontrastvariationen entlang der Plättchen auf transmissionselektronenmikroskopischen Dunkelfeldabbildungen und durch Aufspaltung der Elektronenbeugungspunkte in Feinbereichsbeugungsbildern).

Durch die Ausscheidung von  $\text{Cr}_{1-x}\text{Al}_x\text{N}$ -Plättchen nehmen die Nitrierproben große Mengen an Überschussstickstoff auf. Das ist eine Folge des elastischen Ausgleichs der Fehlpassungen zwischen dem  $\text{Cr}_{1-x}\text{Al}_x\text{N}$ -Gitter und des Ferritmatrixgitters. Die Überschussstickstoffaufnahme ist nahe der Probenoberfläche am größten, weil hier die feinsten Ausscheidungsplättchen auftreten (vgl. Text weiter oben) und die Fehlpassung zwischen Ausscheidungen und Matrix (beinahe) vollständig elastisch ausgeglichen wird. Ein Überschussstickstoffanteil, der auch nach dem Denitrieren in der Probe verbleibt, wird auf Stickstoffatome zurückgeführt, die vor allem stark an die Al Atome an der Oberfläche der Mischnitridplättchen gebunden sind.

### **6.3.2 Phasenumwandlung von inneren $\text{Cr}_{1-x}\text{Al}_x\text{N}$ Mischnitridausscheidungen in Ferrit**

Während des Nitrierens einer ferritischen Eisenbasislegierung mit der chemischen Zusammensetzung  $\text{Fe}-1,5\text{Gew.}\% \text{Cr}-1,5\text{Gew.}\% \text{Al}$  entstehen in der Nitrierschicht metastabile  $\text{Cr}_{1-x}\text{Al}_x\text{N}$ -Mischnitridausscheidungen mit einer kubischen Steinsalz-Kristallstruktur. Die Nitrierschicht nimmt deutlich mehr Stickstoff auf als für die Umsetzung allen Cr's und Al's zu  $\text{Cr}_{1-x}\text{Al}_x\text{N}$  notwendig wäre (nämlich Überschussstickstoff; vgl. Text weiter oben). Durch anschließende Wärmebehandlung bei höheren Temperaturen als die Nitriertemperatur entstehen die Gleichgewichtsphasen CrN und AlN.

Nach der Wärmebehandlung sind in der Nitrierzone Teilchen erkennbar mit kubischer Steinsalz-Kristallstruktur und hexagonaler Wurtzit-Kristallstruktur, die eine Bain-Orientierungsbeziehung bzw. eine Pitsch-Schrader Orientierungsbeziehung mit der Ferritmatrix aufweisen und CrN bzw. AlN zugeordnet werden können. Ein Teil der Ausscheidungen mit kubischer Steinsalz-Kristallstruktur sind nach wie vor  $\text{Cr}_{1-x}\text{Al}_x\text{N}$ -Mischnitride, jedoch mit geringerem Al-Anteil als vor der Wärmebehandlung. Die Phasenumwandlung der ursprünglichen  $\text{Cr}_{1-x}\text{Al}_x\text{N}$ -Mischnitride erfolgt durch Verarmung an Al. Die anschließende AlN-Ausscheidung findet im Korninnern und an Korngrenzen der Matrix statt. Das Ergebnis ist eine vergrößerte Mikrostruktur. Die Ausscheidungen besitzen keine ausgeprägte Kohärenz mehr mit der Ferritmatrix, was durch einen starken Rückgang der Reflexverbreiterung von Ferritmatrixreflexen im Röntgendiffraktogramm und durch eine deutliche Abnahme der Härte angezeigt wird.

Die Wärmebehandlung führt dazu, dass mobiler Überschussstickstoff aus der Nitrierzone in den ursprünglich nicht nitrierten Kern der Probe diffundiert. Dieser Stickstoff scheidet sich unmittelbar in Form von relativ groben CrN-Partikeln an Korngrenzen bzw. als kleine CrN-Ausscheidungen mit kubischer Steinsalz-Kristallstruktur und als AlN-Ausscheidungen mit hexagonaler Wurtzit-Kristallstruktur im Korninnern aus. Es entstehen keine  $\text{Cr}_{1-x}\text{Al}_x\text{N}$ -Mischnitridausscheidungen.

### **6.3.3 Die Mikrostruktur in der Diffusionszone einer gasnitrierten Fe–1,5Gew.%Cr–1,5Gew.%Al-Legierung**

Das folgende Bild ergibt sich für die Entstehung der Mikrostruktur in einer ferritischen, ternären Fe–1,5Gew.%Cr–1,5Gew.%Al-Legierung während des Nitrierens. In der Nitrierzone scheidet sich das kubische  $\text{Cr}_{1-x}\text{Al}_x\text{N}$ -Mischnitrid in der Steinsalz-Kristallstruktur aus. Die Dichte der Ausscheidung ist im an die Oberfläche angrenzenden Bereich der Nitrierzone höher, während die Größe der Ausscheidungen dort kleiner ist. Der Grund dafür ist eine höhere Übersättigung der Eisenmatrix mit Stickstoff nahe der Oberfläche. Die elastische Anpassung an die Fehlpassung zwischen  $\text{Cr}_{1-x}\text{Al}_x\text{N}$ -Ausscheidungen und der Ferritmatrix führt zur Aufnahme einer großen Menge an Überschussstickstoff, insbesondere am Oberflächenbereich der Nitrierzone (vgl. Text weiter oben). Die Ferritmatrix in der Nitrierzone ist stark verzerrt (besonders im oberflächennahen Bereich) und weist, in Übereinstimmung mit dem Spannungszustand, eine hydrostatische Zugspannungskomponente auf, die der elastischen Anpassung an die Fehlpassung zwischen  $\text{Cr}_{1-x}\text{Al}_x\text{N}$ -Ausscheidungen und der Ferritmatrix entspricht. Die Tatsache, dass Al bereits vor dem Nitrieren an Korngrenzen segregiert ist, führt zur Ausscheidung von AlN an Korngrenzen in der Nitrierzone. Cr segregiert nicht. In der Nitrierzone kommt es zu plastischer Verformung (z. B. durch Kriechen). Dies geschieht zuerst im ältesten Teil der Nitrierzone (d. h. im an die Oberfläche angrenzenden Bereich). Der andauernde Nitriervorgang induziert im oberflächennahen Bereich einen ebenen Zugspannungszustand von ausgeprägter Größe, gefolgt von ebenen Druckspannungszuständen in tieferen Regionen (und somit jüngeren Regionen) der Nitrierzone. Die Ausscheidung von ursprünglich gelöstem Überschussstickstoff an Korngrenzen in der an die Oberfläche angrenzenden Region (d. h. im ältesten Bereich)

der Nitrierzone und die Anwesenheit von AlN-Ausscheidungen an Korngrenzen (vgl. Text weiter oben) sowie das Auftreten eines ebenen Zugspannungszustands in diesem Bereich begünstigt die Entstehung und das Wachsen von Rissen, die an der Oberfläche beginnen und sich mehr oder weniger senkrecht zur Oberfläche entlang der Korngrenzen fortpflanzen.



## **Danksagung**

Die vorliegende Arbeit wurde am Institut für Metallkunde der Universität Stuttgart und am Max-Planck-Institut für Metallforschung angefertigt.

Hiermit möchte ich mich bei all denen herzlich bedanken, die zum Gelingen dieser Arbeit beigetragen haben.

An erster Stelle möchte ich mich bei Herrn Prof. Dr. Ir. E. J. Mittemeijer für die freundliche Aufnahme in seine Abteilung bedanken, für das in mich gesetzte Vertrauen und für die wissenschaftliche Freiheit. Sein persönliches Engagement und die regelmäßigen, gemeinsamen wissenschaftlichen Diskussionen haben wesentlich zum Erfolg dieser Arbeit beigetragen.

Herrn Prof. Dr. F. Aldinger danke ich für die freundliche Übernahme des Mitberichts sowie Herrn Prof. Dr. E. Roduner für die Zusage, den Prüfungsvorsitz zu übernehmen.

Herrn Dr. R. E. Schacherl und Herrn Dr. E. Bischoff danke ich für die tägliche Betreuung, stete Diskussionsbereitschaft und für die experimentelle Hilfestellung. Beide haben in großem Maße zur erfolgreichen Durchführung dieser Arbeit beigetragen.

Allen Mitarbeiter/innen des Max-Planck-Instituts für Metallforschung, insbesondere den Kollegen/innen der Abteilung Mittemeijer, danke ich für die Unterstützung bei den Problemen des Forschungsalltags und die gute Zusammenarbeit in freundschaftlicher Atmosphäre. Dabei gilt mein besonderer Dank Nicolás Vives Díaz, meinem langjährigen Zimmerkollegen.

Meinen Freunden und Bekannten danke ich für das Verständnis, das sie mir in dieser Zeit entgegen gebracht haben.

Zu guter Letzt gilt ein ganz besonderer Dank meiner Familie, vor allem meinen Eltern und meiner Frau Regine, die mich stets in allen Lebensbereichen großzügig und liebevoll unterstützt haben.



# Curriculum Vitae

## Persönliche Daten

Name Arno Rainer Clauß  
geboren am 9. Dezember 1976 in Lauffen am Neckar  
Staatsangehörigkeit deutsch

## Schulbildung

1983 – 1987 Herzog-Ulrich-Grundschule Lauffen a. N.  
1987 – 1996 Hölderlin-Gymnasium Lauffen a. N.  
Abschluss: Abitur

## Zivildienst

1996 – 1997 Arbeiter-Samariter-Bund Deutschland e. V.  
Rettungssanitäter im Krankentransport

## Berufsausbildung

1997 – 1999 Fa. Schunk GmbH & Co. KG  
Maschinenbaumechaniker

## Studium

1999 – 2005 Universität Stuttgart  
Diplomstudiengang Werkstoffwissenschaft  
Abschluss: Dipl.-Ing. Werkstoffwissenschaft

2005 Diplomarbeit am Institut für Metallkunde  
Thema: „Kinetik des Nitrierens von Fe–Cr–Al-Legierungen“  
Hauptberichter: Prof. Dr. Ir. E. J. Mittemeijer

## Promotion

2005 – 2008 Universität Stuttgart, Institut für Metallkunde und  
Max-Planck-Institut für Metallforschung, Stuttgart  
Thema: „Nitriding of Fe–Cr–Al alloys: nitride precipitation and  
phase transformations“  
Hauptberichter: Prof. Dr. Ir. E. J. Mittemeijer